

Applications of Optics in Biology: Laser Spectroscopy and Image Analysis

Author: Yueyu Lin

Supervisors:

Professor Katarina Svanberg and Professor Sune Svanberg

Major: Optics

Research: Optical Applications in Photobiology

Address: Centre for Optical and Electromagnetic Research,

South China Academy of Advanced Optoelectronics

Abstract

Photobiology is the science of light interaction with living structures and it is a subdiscipline in biology. The focus of photobiology is on the effects of light, especially, the nonionizing radiation on organisms and biological processes. There are 13 different speciality areas in photobiology. In this thesis, we deal with several projects related to the areas in photobiology by using optical techniques. The projects are related as all are dealing with scattering of light, sometimes leading to advantages, sometimes to detrimental effects. Gas in Scattering Media Absorption Spectroscopy (GASMAS) is a spectroscopy technique used in free gas monitoring projects, such as studies of food packages, medical diagnostics, etc. With the development of techniques, optical sensors are not only much used in daily life, but are also an indispensable part of scientific research. The main function of optical sensors is to convert light into electronic signals, which means that it can measure the physical quantity of light and then transform it to a readable signal for an instrument. We used these optical sensors to perform scientific research and explore the possibilities of further studies.

The projects in this thesis using the GASMAS technique are related to medical testing and diagnostics. Sinusitis is now threatening the normal life of millions of people. The clinical treatment of sinusitis mainly relies on drugs (such as antibiotics), which has led to drug abuse. We studied and compared the gas exchange between healthy people and patients after decongestant treatment and investigated the stability of signals. The purpose of the studies is to introduce the GASMAS technique as an auxiliary technology to the diagnostics of sinusitis. We found that the decongestants effectiveness to open the sinus channel of affected individuals and accelerate the free gas exchange could be monitored with the GASMAS technique. We could also see that decongestant ways had no effect on the sinus channel of healthy people. The GASMAS techniques has been successfully used to study lungs of neonatal infants. Respiratory distress syndrome (RDS) is common in prematurely born children. Now we want to further explore the possibility of applying the GASMAS technique to older children and even

adults. Large-scale GASMAS experiments were operated by using a narrow-band pulsed laser in the laboratory. Polystyrene foam blocks and biological tissues (such as chicken, pork, etc.) were used for simulating human tissues in the experiment.

Mosquitoes are the deadliest animals in the world, and can spread about 100 diseases. Thus, monitoring and analysing mosquitoes and their movements are highly needed to effectively control the spread of diseases. We used two types of photoelectric sensors, photodiodes and cameras, to detect and classify mosquitoes. Wing-beat frequency is widely used as a feature information of insects for species and sex identification. In this thesis, we designed two mosquito counting systems based on three different optical methods, including shading and scattering, and also imaging. Four mosquito groups *Aedes albopictus* (male, female) and *Culex pipiens* (male, female) were used for studying detection and classification capability. An insect trap was placed below the systems for mosquito counting and capturing. The species and sexes of mosquitoes can be distinguished based on wing-beat characteristics. after signal extracting and Fourier transform operations. Image analysis is a major research content in moving object detection. We introduced it as a mean for mosquito identification and explored the possibility of mosquito detection in real-time. Although the images were not so clear, we have extracted the contour features of two different insects (mosquitoes and bees) and performed a simple classification. The results showed that even rough imaging can achieve high detection rate and classification accuracy. The study provided a basis for the next step of improved imaging to classify mosquitoes by species and sexes.

Unimpaired vision is a prerequisite for our normal life. However, in normal life our vision will be impaired due to various external factors, such as scattered sunlight, headlight from approaching vehicles, etc. Fortunately, the human brain acting like a supercomputer can process information from the outside world and extract effectively the characteristics of the object of interest from the image and reconstruct object of interest also from imperfect images recorded in a sequence. We have combined two typical digital image processing techniques to mimick this function of the brain. On the

basis of a Gaussian Mixture Model (GMM), we introduced an Interframe Difference method in a new approach. Through testing, our method can effectively eliminate the uninteresting parts (foreground) in the image and reconstruct the interesting parts (background). At the same time, our proposed method has a slight improvement compared to the Gaussian Mixture Model and the Interframe Difference method acting alone. We have also established a connection with Gestalt psychology.

Key words: Photobiology, Light scattering, Gas in Scattering Media Absorption Spectroscopy (GASMAS), medical diagnostics, mosquitoes, optical sensors, images, vision, Gaussian Mixture Model (GMM), Interframe Difference method, Gestalt psychology.

Content

| | |
|---|----|
| Abstract | 1 |
| Chapter 1 Introduction | 1 |
| 1.1 Background | 1 |
| 1.2 Topics of the thesis | 3 |
| 1.2.1 GASMAS applications in the medical field | 3 |
| 1.2.2 Mosquito monitoring and analysis | 4 |
| 1.2.3 Foreground scattering elimination | 7 |
| 1.3 Structure of the thesis | 9 |
| Chapter 2 Principles | 9 |
| 2.1 Light-matter interaction | 9 |
| 2.2 Absorption | 10 |
| 2.3 Scattering | 12 |
| 2.3.1 Elastic scattering | 13 |
| 2.3.2 Inelastic scattering | 14 |
| Chapter 3 GASMAS applications in the medical field | 15 |
| 3.1 Sinus monitoring | 18 |
| 3.2 Lung spectroscopic monitoring | 21 |
| Chapter 4 Mosquito detection and analysis | 24 |
| 4.1 Wing-beat frequency detection | 25 |
| 4.1.1 Shading system | 25 |
| 4.1.2 Scattering system | 27 |
| 4.2 Image detection | 29 |
| 4.3 Measurements and results | 30 |
| 4.3.1 Scattering system and shading system | 30 |
| 4.3.2 Imaging system | 36 |
| Chapter 5 Foreground scattering elimination | 42 |
| 5.1 Gaussian Mixture Model (GMM) | 45 |

| | |
|--|----|
| 5.2 Interframe Difference Method..... | 48 |
| 5.3 Measurements and results | 50 |
| 5.3.1 System set-up and image process..... | 50 |
| 5.3.2 Discussion of results and evaluation..... | 52 |
| Chapter 6 Conclusion and outlook..... | 56 |
| References | 58 |
| Acknowledgements | 66 |
| Publications | 68 |

Chapter 1 Introduction

1.1 Background

Light is one of the most important factors in our daily lives. Plants grow by absorbing energy from sunlight and then provide food for other living creatures. Sunlight is also strongly linked to the behavior and reactions of many organisms on Earth. But at the same time, certain wavelengths of light can cause adverse reactions or even death. Photobiology is a research area of the beneficial and harmful effects of light, ranging from the atomic level to the community level [1]. There are 13 main areas of research in photobiology; the list is shown below:

Photophysics: A specialty area where the focus is on the interactions of light with matter at the atomic and molecular level.

Photochemistry: This area studies the chemical changes that occur in molecules after absorbing light energy directly.

Spectroscopy: The study of the absorption and emission of light by matter.

Photosensitization: During the interaction of light with the system, the light energy is absorbed by one molecule (the sensitizer), and then the energy-rich states of the sensitizer react, resulting in the chemical change of another type of molecules (the substrate molecules) in the system.

UV Radiation Effects on Molecules and Cells: This field is concerned with the photochemistry of deoxyribonucleic acid (DNA), ribonucleic acid (RNA) and proteins under UV radiation.

Environmental Photobiology: The area deals with the effects of light on species composition and productivity.

Photomedicine: This field focuses on the beneficial and detrimental effects of non-ionizing radiation.

Vision: A photoreception that results in the formation of an image.

Non-Visual Photoreception: Different from vision, light is received by a receptor in an organism for monitoring the environment instead of forming an image.

Photomorphogenesis: Studies of the influences of different types of light during the

development of organisms, including the quantity, the quality of light (e.g., wavelength present), spatial asymmetry (e.g., the direction from which the light comes), and the periodicity of light.

Photomovement: Plants and organisms depend on the quality and the direction of the light striking their photoreceptors to provoke movement.

Photosynthesis: The process by which plants capture light energy from the sun and integrate it into molecules for use by organisms is called photosynthesis.

Bioluminescence: Bioluminescence is the highly efficient cold-light emission that has a biological function for the organism concerned.

This thesis primarily discusses three of these main fields: Photophysics, Spectroscopy and Vision. The projects presented are all dealing with the scattering of light, sometimes leading to advantages, sometimes to detrimental effects.

As fast, powerful and non-invasive methods, optical spectroscopic techniques have been used widely for different kinds of applications, such as environmental monitoring, food safety analysis, medical diagnostics, and other applications. The Gas in Scattering Media Absorption Spectroscopy (GASMAS) technique will be introduced and its practical application in medical diagnostics will be presented. Optical sensing techniques are widely used in detection due to its high precision, ultra-fast response time, multiple detection parameter capability, and for other reasons. Common optical sensors mainly include photodiodes (PD), photomultiplier (PMT) sensors, and Complementary Metal Oxide Sensor (CMOS) imaging detectors in cameras. Two different types of methods were proposed in Sect. 4 to detect and classify mosquitoes, based on photodiodes (PD) and camera, respectively.

The images produced by the human eye will become our memories after being processed and stored by our brains. A simple approach related to image improvement, denoted inverse lock-in-like spatial modulation (ILLSPAM), is presented in the thesis. This approach enhances human vision in the time domain by eliminating the foreground. A new imaging process technique based on the combination of the Interframe

Difference, and the Gaussian Mixture models (GMM) was used to separate foreground objects and the background. There is an interesting connection to the Gestalt vision psychology field.

1.2 Topics of the thesis

1.2.1 GASMAS applications in the medical field

Spectroscopy defines a number of techniques that use radiation to obtain information on the structure and properties of matter [1]. The basic principle of spectroscopic techniques is to transmit a beam of electromagnetic radiation onto a sample, and observe how it responds to such a stimulus. Recordings of responses to excitation wavelengths and distributions of emitted wavelengths are called spectra. Spectroscopy techniques are widely used in various fields, such as astronomy, agricultural monitoring, medical diagnostics and in numerous other fields.

The Gas in Scattering Media Absorption Spectroscopy (GASMAS) technique was introduced by S. Svanberg and his colleagues at the Lund University in 2001 [2, 3]. Since then, researchers applied GASMAS in many different fields, including food safety monitoring (e.g., regarding eggs, and various types of food packages, including milk [4-6]) and medical testing and diagnostics (e.g., regarding the middle ear, sinuses, hip bones, and also for monitoring lung in small infants [7-11]).

Rhinosinusitis, or for short sinusitis, is an inflammation or swelling of the tissue related to the human sinuses. Generally, healthy sinuses are filled with air. Common causes of sinusitis are respiratory tract infections, allergies, specific nasal conditions, etc.[12] These causes can make sinus ventilation blocked and the sinuses become filled with fluid; bacteria and virus can grow and cause an infection. Sinusitis can be divided into acute sinusitis and chronic sinusitis [13]. Doctors usually determine the presence of sinusitis based on a simple physical examination. However, such diagnosis always requires the professional knowledge and rich experience of a doctor. More complex and professional diagnostic methods are also applied, including nasal endoscopy, imaging studies, nasal and sinus sampling and allergy testing. The main treatments for sinusitis

include symptom relieving, administration of nasal decongestant or antibiotics, immunotherapy and surgery. The use of antibiotics, which are not effective against virus, may lead to abuse and is clearly associated with drug resistance development [14]. A quick and accurate diagnostics method cannot only help doctors to better find the cause of sinusitis, but also treat it earlier and better. We are further developing a non-invasive monitoring method based on the GASMAS technique to characterize sinusitis and help doctors offer better treatments.

The respiratory distress syndrome (RDS) occurs when a baby's lungs are not fully developed and therefore have difficulties to provide enough oxygen to the organs, especially the brain [15]. The use of the GASMAS technique to detect lung function of newborns has been successfully implemented [16, 17]. In the monitoring of the small infants, fiber-optical internal light administration (such as tracheal intubation) can be used to perform GASMAS. Diode lasers with few mW outpower have been used in first studies, mostly on phantoms. However, older children and adults cannot be studied because of low signal levels. A larger-scale GASMAS implementation must be used to achieve higher probing light fluxes. In adult cases, patients usually suffer from severe respiratory diseases such as pneumonia, chronic obstructive pulmonary disease, pulmonary fibrosis, and of course SARS-CoV-2, which is now influencing the whole world. Direct optical monitoring of lung volume and oxygen distribution can reveal the disease progression and complications in time. Our goal is to be able to use the GASMAS technique to directly determine lung states and control the use of ventilators in older children and adult cases [18]. This requires the development of techniques employing more powerful lasers.

1.2.2 Mosquito monitoring and analysis

According to statistics data from the World Health Organization (WHO) [19], infectious diseases such as malaria, tuberculosis (TB) and HIV are some of the biggest killers in the world. Figure 1.1 from [19] illustrates the incidence rate of these three diseases. Since 2000, the incidences of HIV, TB and malaria have decreased, yet they still are major threats to human beings.

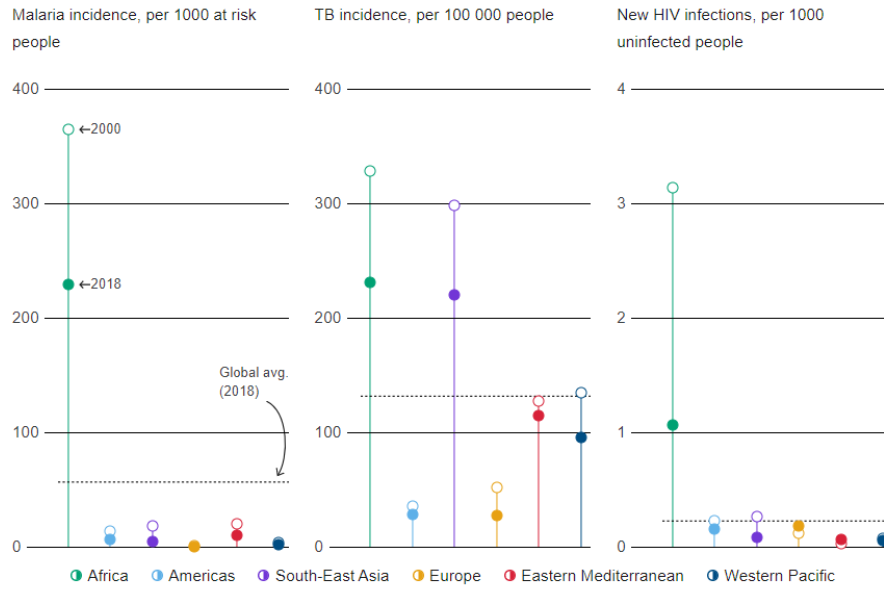


Fig. 1.1 Malaria, tuberculosis, and HIV incidence rates globally [20].

In fact, from Figure 1.1 we can see that the situation in Africa is still far worse than in other regions in the world, although it has improved a lot in the past two decades. Global statistics for 2019, around 409, 000 people died because of malaria. With an estimated 215 million malaria cases and 384, 000 malaria deaths in 2019, the African region accounts for 94% of global cases and deaths [20]. Malaria is a mosquito-borne infectious disease that affects humans and certain animals and is caused by single-celled microorganisms of the *Plasmodium* group. Parasites enter the mosquito first, and are then transferred to the human blood through the bite of the mosquito. After entering the human blood, the parasites move to the liver and start to grow and multiply. Infected people will have symptoms including fever, tiredness, vomiting and headache. In worse cases, yellow skin, seizures, coma, and even death will happen [21].

Not only malaria, but also many other diseases, such as West Nile virus, Zika virus Chikungunya virus, and dengue fever can spread through mosquitoes; so-called mosquito-borne diseases [22]. Monitoring the types of mosquitoes, and statistics and analysis of their mobility, are important in controlling the spread of mosquito-borne diseases and reducing deaths caused by such diseases. In this thesis we propose three different methods to monitor and distinguish the species and sex of mosquitoes.

Our first approach to mosquito monitoring is based on optical sensing techniques.

Applying such techniques for monitoring insects has been an expanding research area. It is believed that the use of two photoelectric cells by I.R. Richard, localized close to each other, was the first attempt in optical insect detection [23]. M. Brydegaard and collaborators at Lund University, Sweden, developed fluorescence lidar techniques to monitor insect. They used backscattered signals to identify insect species remotely [24, 25]. Another type of signals for monitoring insects is their wing-beat frequency signal. In [26], I. Potamitis developed a novel noise-robust optoacoustic sensor, which could be inserted into typical insect traps. Not only sensors but also data processing methods are becoming more intelligent, automated and efficient. E. Fanioudakis et al., from Greece performed a large-scale classification experiments by using deep learning methods [27]. E. Fanioudakis et al., conducted experiments on a data base containing close to 300,000 flight record cases, and obtained a classification accuracy of 96%. However, these methods are generally expensive regarding equipment and require professional knowledge to operate. Our approach uses three counting devices, which have the advantages of low cost and high accuracy, etc.

Another approach is to apply camera imaging to detect and classify mosquitoes based on their characteristic features such as shape, size and color. A solution was presented in [28]. A dataset of *Aedes Aegypti* mosquito species collected by a camera with a 500x optical zoom was used as input to a support vector machine (SVM) algorithm. In [29], a more advanced algorithm based on a Convolutional Neural Network (CNN) was also used to detect and classify insects. A vision-based counting and recognition system was built by using so called You Only Look Once (YOLO) and SVM algorithms [30]. By combining the detection function of YOLO and the classification function of SVM, the system can achieve a detection rate of 93% and a classification rate of 90%. However, these advanced methods require large data bases to train neural networks, which make them both time-consuming and expensive. We put forward a simple approach, using a low-cost mosquito capture device to make an optical darkroom to take pictures of flying mosquitoes by a low-cost camera and then preliminarily classify them.

1.2.3 Foreground scattering elimination

Human conception of the world is largely based on the spatial information obtained by vision. The retina at the back of the eye contains millions of photoreceptor cells, which can perceive the three colors of RGB (red-green-blue). When the light reaches the retina, it is absorbed by these cells and converted into biological signals to be transmitted to the brain, and then processed by the brain to form an image [31, 32].

The quality of human vision formation is also related to the external environment. Apparently, people can get the best visual information when the view is open and clear. For example, human vision is strongly impaired in a dark environment. That is because the color-responsive receptors in the cones are less sensitive and thus inefficient in low-light condition. Vision is then reduced to use a grey scale produced by the rods. Another factor that also has an impact on vision is the scattering of the medium during the transmission process. The spectral range of visible light that forms human vision is around 400-700 nm. The light in this range will not be absorbed by the transmission medium (normally air), but the scattering of particles present will still cause obstacles to human vision. The scattering of a close lying, physically structured semi-transparent layer, can be a further reason of vision impairment, making it difficult to isolate and identify distant objects.

Figure 1.2 shows a common situation of vision impairment when driving. The objects that need attention are far away, but the line of sight passes through a structured window with strong scattering, due to meeting car headlights or the sun. The nearby scattered light completely overwhelms the light from the distant object. Such situations can easily happen while driving, and cause severe vision impairment. The practical approach is of course to keep the windshield of the vehicle perfectly clean, so that the driver can see the distant target more clearly. However, things are not always perfect in real life.



Fig. 1.2 Illustration of vision impairment when driving [II].

There are further vision impairment examples in common life. For example, when you want to see the objects on the opposite side of a busy road, passing vehicles partly block your view. In fact, the human brain can well save some information elements about the object of interest to link them together, and from a temporal sequence of partial images then rebuild the scene and object of interest. In the computer vision field, well-known digital image processing techniques of background subtraction and integral imaging are used to handle this situation [33-39].

In this thesis we focus on a simple and universal method of vision enhancement. This method only focuses on the enhancement processing on the receiving side (such as by eyes, cameras, etc.), because processing on the lighting side, such as tagging by intensity or spatial modulation, is very difficult, and impossible for, e.g., sunlight. The method is inspired by lock-in detection, the principle of which is to extract objects of interest and tagged with specific frequencies, from noisy and overwhelming background signals. We used a lock-in-like detection technique for the two-dimensional space. We consider foreground objects with a specific moving periodic pattern as high-frequency signals with a specific frequency, while stable background objects of interest are considered as low-frequency background signals. During the processing, the unwanted part of the signal is isolated and eliminated, and the overall vision will be enhanced. Since modulation is used in this technique, but for the opposite purpose compared to the normal case of tagging the signal of interest, the new approach can be described as inverse lock-in-like spatial modulation (ILLSPAM).

1.3 Structure of the thesis

The thesis is composed of six chapters, and the content of each chapter can be summarized as follows:

Chapter 1: A brief introduction of optical applications in biology is provided. The research contents of three different but related projects are also briefly presented.

Chapter 2: This chapter shows some basic principles of the interaction between photons and molecules, such as absorption and scattering and so on.

Chapter 3: This chapter describes the medical applications of the Gas in Scattering Media Absorption Spectroscopy (GASMAS) technique, including sinus gas detection and efforts towards adult lung monitoring, and starts with an introduction to the basic principles of GASMAS technique.

Chapter 4: Two different mosquito detection methods are introduced and there are wing-beat frequency analysis and image matching, respectively. By applying wing-beat frequency analysis, *Aedes albopictus* and *Culex pipiens* mosquitoes could be detected and classified with high accuracy.

Chapter 5: This chapter introduces a simple method of inverse lock-in-like spatial modulation (ILLSPAM) to enhance vision. The processing can be performed by human vision reception or be based on a combination of the Interframe Difference (ID) and Gaussian Mixture models (GMM).

Chapter 6: This chapter summarizes the conclusions and gives an outlook related to the work in this thesis.

Chapter 2 Principles

2.1 Light-matter interaction

Light-matter interaction occurs when light encounters matter, including absorption, reflection, transmittance, emission and scattering processes. Figure 2.1 is a Jablonski diagram of the possible transitions when a molecule is photoexcited. Different energy levels of a molecule are shown by horizontal lines, with the energy increasing along the

vertical axis of the figure. Most of the time, molecules stay at the ground state S_0 , which is the level with lowest energy. When a photon is absorbed, the molecule will be excited to a level with higher energy, e.g.; S_2 . S_2 has a higher energy and is unstable in contrast to the ground state. A molecule in a higher energy level may pass to the lowest energy level of the first singlet excited state S_1 by internal conversion (IC). Molecules can come back to some sub-levels of the ground state S_0 in the timescale of several nanoseconds by emitting a photon, a process, which is called fluorescence. Alternately, the molecule can jump from the lowest level of the singlet excited state S_1 to the lowest energy level of a triplet state T_1 through another non-radiative process called intersystem crossing (ISC). After a rapid vibrational relaxation, the process is temporarily stopped at the lowest level of the T_1 state. The emission of photons from T_1 to S_0 constitutes the process of phosphorescence. This process occurs on a much slower time scale than fluorescence.

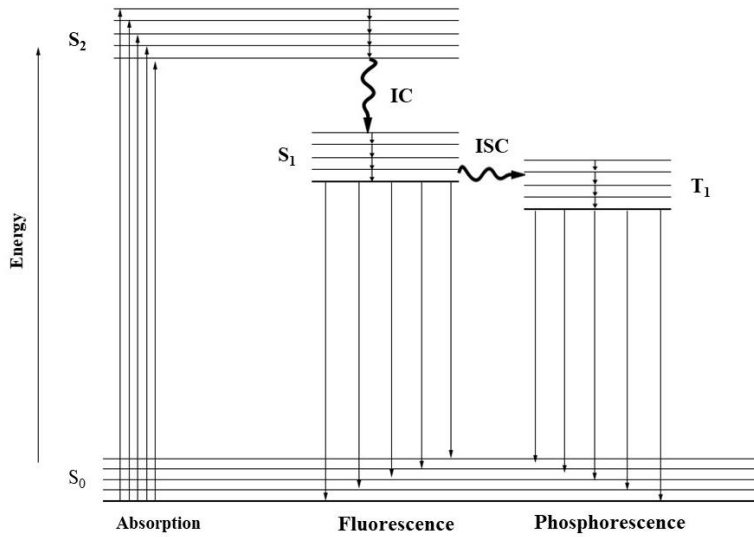


Fig. 2.1 Energy-level diagram, possible processes following light excitation.

2.2 Absorption

As mentioned in Sect 2.1, absorption occurs when a photon interacts with an atom or molecule. In this interaction, the energy carried by the photon is exactly equal to the

energy level difference between the two energy levels, and the atom or molecule at the ground state is transferred to a higher-energy state. Atoms and molecules have characteristic energy level and only photons with an energy matching energy spacings can be absorbed. The energy E carried by a photon is related to the wavelength λ of the light according to $E = \frac{hc}{\lambda}$, where h is the Planck constant, $6.63 \times 10^{-34} \text{ J} \cdot \text{s}$ and c is the velocity of light, $3 \times 10^8 \text{ m/s}$. Figure 2.2 presents the absorption spectrum of human tissue constituents (e.g., hemoglobin, fat, and water). Hemoglobin has strong absorption in the visible region (except red color) and water has major absorption in the infrared range. A small wavelength region between 650 and 1350 nm with low absorption due to water, hemoglobin and fat is identified, and is called the near-infrared (NIR) window or the human tissue optical window.

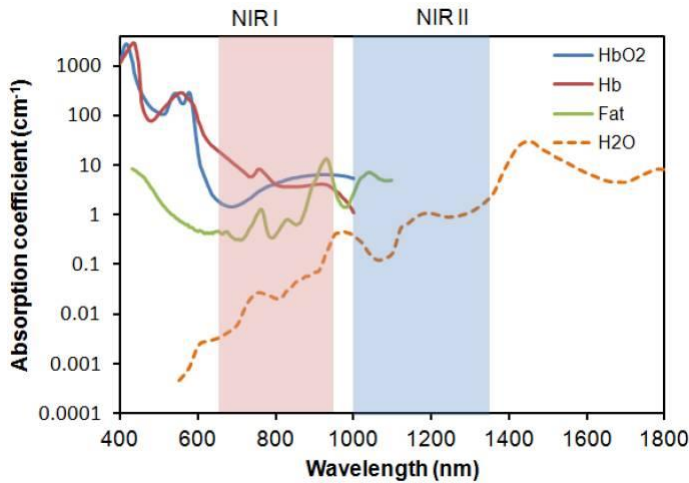


Fig. 2.2 Absorption coefficient (on a log scale) of oxygenated blood, deoxygenated blood, fatty tissue and water as a function of wavelength [40].

Oxygen and water vapor are the two main gases studied with the GASMAS technique in this thesis. Therefore, the characteristic absorption spectra of oxygen (around 760 nm) and water vapor (in a wide wavelength range) are relevant to this thesis. An open access spectral line data base called HITRAN (an acronym for high-resolution transmission molecular absorption database) [41] is a convenient reference data base for absorption lines. Figure 2.3 shows the absorption spectra of oxygen around 760 nm and water vapor around 937 nm, with numerous sharp (linewidth $\sim 0.001 \text{ nm}$) rotational-vibrational line components.

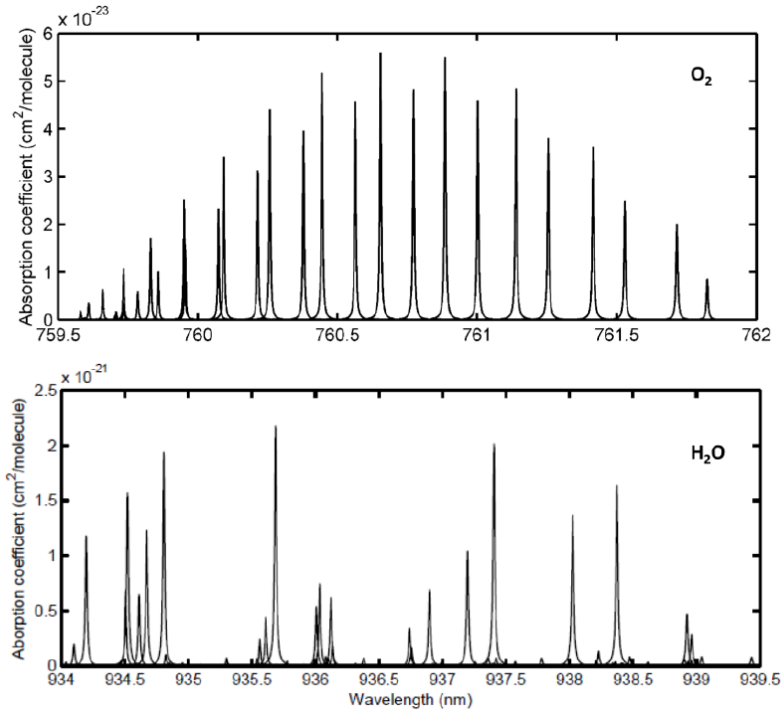


Fig. 2.3 Oxygen and water vapor absorption lines around 760 nm and 937 nm [41, 42].

2.3 Scattering

Scattering occurs during the propagation of light in an inhomogeneous medium. Generally, light travels in a straight line in a homogeneous medium. Part of the light in the inhomogeneous medium will deviate from the original direction, so light can also be observed from the side. Biological tissue is an inhomogeneous medium, so light entering a biological system will be scattered. There are two types of scattering, according to the change of energy: elastic scattering and inelastic scattering. Elastic scattering means that the energy lost during the scattering process is zero, such as in Rayleigh scattering and Mie scattering. In elastic scattering, only the propagation direction of light will change, but the scattering light wavelength will remain the same as the original incident wavelength. In contrast, inelastic scattering means that the energy of the photon in the process of scattering is changed; a wavelength shift occurs. Inelastic scattering includes Raman scattering, Brillouin scattering, and Compton scattering [43].

2.3.1 Elastic scattering

As discussed above, both Rayleigh scattering and Mie scattering belong to elastic scattering, and the energy of light will not change in the process. The classification difference between Rayleigh scattering and Mie scattering relates to the size of the particles in the inhomogeneous medium. When the size of the particle is about one-tenth or less of the wavelength of the incident light, Rayleigh scattering occurs. Mie scattering refers to the phenomenon, when the size of the particles is close to, or larger than the wavelength of the incident light.

According to the Rayleigh scattering law, the intensity of such scattered light is proportional to $\frac{1}{\lambda^4}$, where λ is the wavelength of the incident light. It means that scattered light with longer wavelength has weaker intensity. A very common example in life is that the color of the sky is different at different times of the day. Blue light has a short wavelength and the blue light is strongly scattered against atmospheric molecules. The sky is beautifully blue. At sunset or sunrise, when the sunlight travels a relatively long way through the atmosphere, the blue light is strongly laterally scattered, leaving mostly red light to reach the eye.

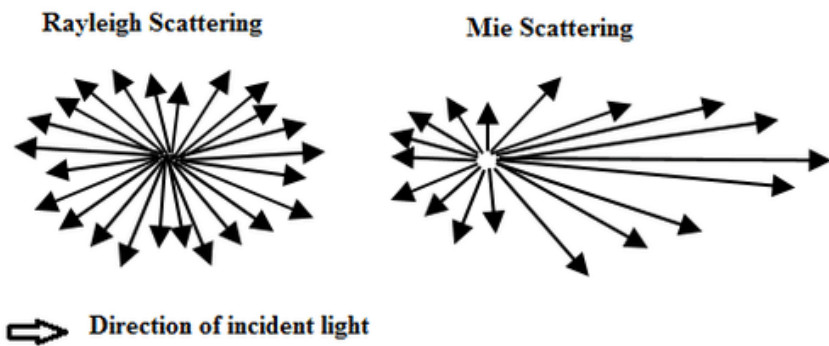


Fig. 2.4 The scattering distributions of Rayleigh scattering and Mie scattering [44].

Scattering against particulates and water droplets in the atmosphere follow the laws of Mie scattering with low wavelength dependence. The resulting light becomes grey like on a cloudy and strongly polluted day. Figure 2.4 describes the scattering distribution of Rayleigh scattering and Mie scattering. Unlike for Rayleigh scattering, Mie scattering is enhanced in the forward direction.

2.3.2 Inelastic scattering

In the interaction with a molecule, part of energy can be emitted or absorbed by the molecule, corresponding to a change in the frequency of the scattered light, and this phenomenon is called inelastic scattering. Raman scattering is a common process of this type. Raman scattering has a great similarity to Rayleigh scattering; the difference lies in the changes of energy and the power is much weaker.

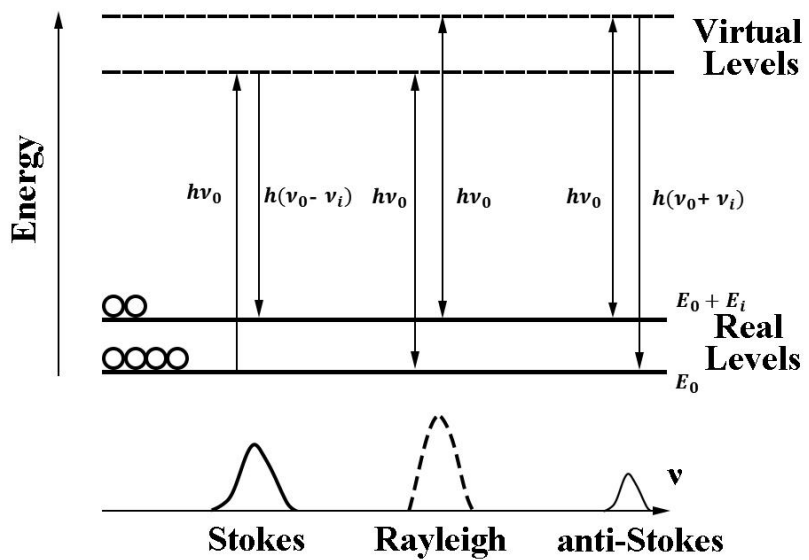


Fig. 2.5 Raman scattering and Rayleigh scattering (adapted from [45]).

As shown in Figure 2.5, a photon with energy $h\nu_0$ interacts with a molecule in the ground state and the molecule transfers to a higher, virtual, energy level. A molecule at a virtual energy level may immediately return to the ground state in three different ways, in so-called Stokes Raman scattering, Rayleigh scattering (discussed in Sect 2.3.1) and anti-Stokes Raman scattering. In the Rayleigh scattering situation, the molecule returns to its original state, and the energy of the emitted photon is the same as that of the energy of the incident photon, $h\nu_0$. In the Stokes Raman scattering process, the molecule decays to a higher real vibrational energy level located $h\nu_i$ above the lowest state, and emits photons with lower energy, $h(\nu_0 - \nu_i)$. Anti-Stokes Raman scattering means that the molecule starts in a higher, less populated vibrational state, and decays to a lower real vibrational energy level, and then emits a photon with higher energy, $h(\nu_0 + \nu_i)$.

Chapter 3 GASMAS applications in the medical field

In Chapter 3, we introduce the Gas in Scattering Media Absorption Spectroscopy (GASMAS) technique and the applications in the medical field. The relevant principles and techniques will first be presented.

As discussed in Sect. 2.2, absorption is one the main processes when light interacts with matters. The Beer-Lambert law relates the attenuation of light to the properties of the medium through which the light passes. The law was discovered by P. Bouguer before 1729 [46] while it is frequently credited to J. H. Lambert, who quoted it in his *Photometria* in 1760 [47]. Lambert's law explains the relationship, that the loss of light intensity when light propagates in the medium is proportional to the optical path length. In 1852, A. Beer discovered another relation, stating that the absorption remains constant if the product of the medium concentration and the optical path length remains the same [48]. The Beer-Lambert law combines the above two laws and became the basic law of light absorption, which is applicable to all electromagnetic radiation and all light-absorbing substances, including gases, solids, and liquids.

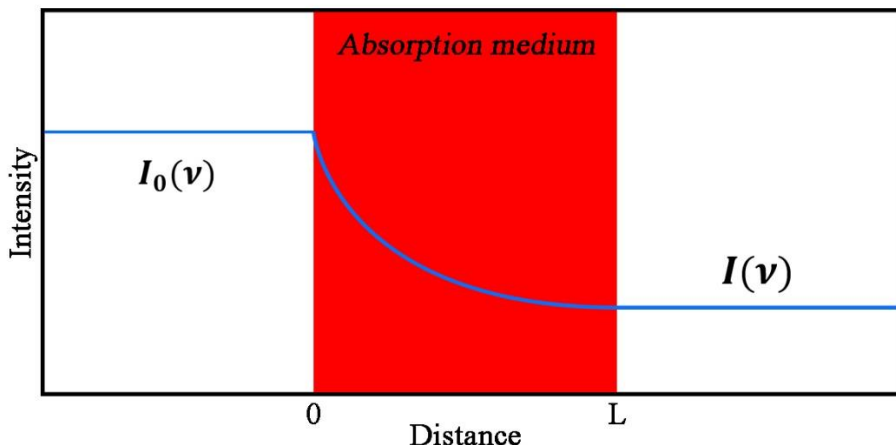


Fig 3.1 Schematic diagram of the attenuation of light when transmitted through an absorbing medium.

Figure 3.1 shows a schematic diagram of the attenuation when light is transmitted through an absorbing medium. When the light of intensity $I_0(\nu)$ passes through a uniform medium with thickness L, the transmitted light will be attenuated due to the

absorption. According to the Beer-Lambert law, the transmitted light intensity $I(\nu)$ is given by:

$$I(\nu) = I_0(\nu) \exp(-\alpha(\nu)CL) \quad 3.1$$

Here, ν is the frequency of light; $\alpha(\nu)$ is the absorption coefficient at frequency ν of the gas; C is the concentration of the gas; L is the gas absorption path-length. The absorbance $A(\nu)$ of the gas at frequency ν can be expressed as:

$$A(\nu) = -\log_{10} \frac{I(\nu)}{I_0(\nu)} = 0.434 * \ln \frac{I_0(\nu)}{I(\nu)} = 0.434 * \alpha(\nu)CL \quad 3.2$$

Therefore, the concentration of the homogeneous medium C and the absorption length of light L can be obtained from the intensity of incident light $I_0(\nu)$ and the intensity of transmitted light $I(\nu)$, if the specific absorption strength factor $\alpha(\nu)$ is known.

Tunable diode laser absorption spectroscopy (TDLAS) is a technique suitable for free gas monitoring. The basic TDLAS set-up consists of a tunable diode laser as light source, transmission optics (e.g., for beam shaping), absorbing medium, receiving optics and a detector. A distributed feedback (DFB) tunable diode laser is frequently a core part of the TDLAS technique. Such lasers have a line width of less than 10 MHz. These lasers can be tuned by either adjusting the temperature or by changing the drive current. As described in Sect. 2.2, gases have specific discrete absorption lines, and the appropriate absorption lines must be selected for the monitoring. Figure 3.2 shows the procedure of using the TDLAS technique to measure the concentration of gases.

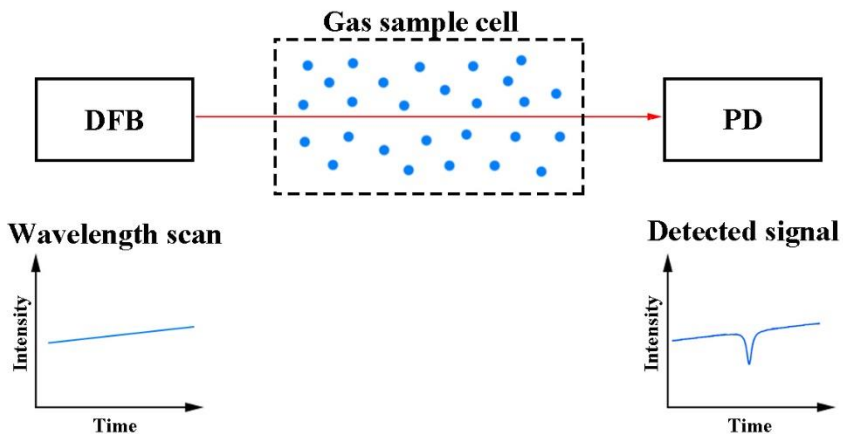


Fig. 3.2 The basic principle of TDLAS, adapted from [49].

Most biological substances, such as food stuffs and human tissues, are strongly scattering media. Clearly, the scattering processes inside must be considered when studying absorption, which is not the case for TDLAS. The gas in scattering media absorption spectroscopy (GASMAS) technique was proposed on the base of the combination of the tunable diode laser absorption spectroscopy (TDLAS) and light scattering processes, and deals with the absorption in the propagation of light in a scattering medium. This technique was proposed to mainly detect oxygen and water vapor contents in a variety of scattering media. Figure 3.3 shows the basic principle of the GASMAS technique. Unlike TDLAS, when the light enters a scattering medium, scattering and absorption processes will be intertwined, when not only the intensity of the light but also the direction will change. By comparing the laser intensity at the transmitter and the signal intensity at the detector, it can be found that when the light on its way to the detector has passed through gas-filled locations, a weak gas absorption signal appears. Figure 3.3 shows two different scattering situations. The figure to the left shows a situation where the scattering medium is containing many small pores, such as alveoli in a human lung, pores in ceramic materials, etc. The figure to the right shows another situation, with a large single cavity filled with gas and surrounded by a scattering medium, such as for the cases of sinuses and the middle ear cavities in the human body.

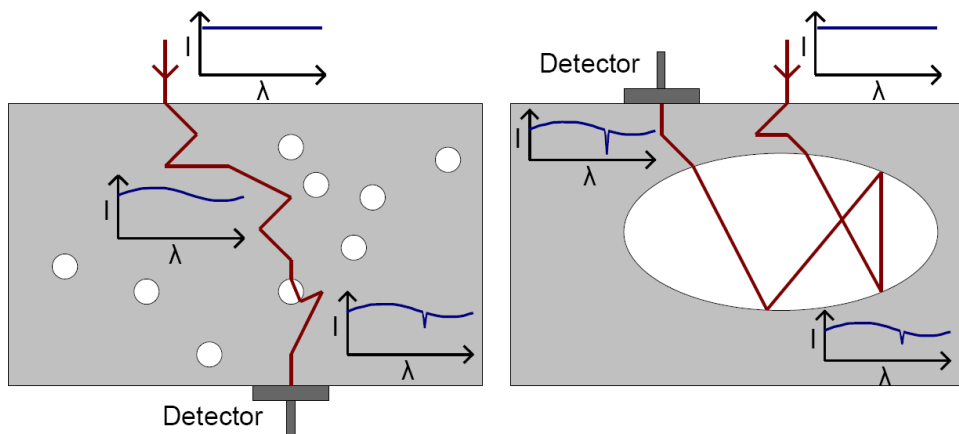


Fig. 3.3 Two types of situations applying to the GASMAS technique performance, adapted from [50].

3.1 Sinus monitoring

The sinuses are hollow spaces in the skull and the face bones around the nose. There are four pairs of sinuses named after the bones where they are located, including the maxillary sinuses (in the cheek bones), frontal sinuses (in the forehead), ethmoid sinuses (near the eyes) and sphenoid sinuses (behind the eyes). Figure 3.4 shows these four pairs of sinuses in the human facial skeleton. In fact, the sinuses are part of the nose and the respiratory system, and connect to the nasal cavity in a complex network of air flow and drainage passages. The healthy sinuses are normally filled with air. Any infection of the upper respiratory tract can easily spread to the sinuses as the mucosa of the nose continues uninterrupted to the lining of the sinuses, thus connecting the sinuses with the infectious agent entering the nose. The resulting infection is called rhinosinusitis, or simply sinusitis. Sinuses can be infected by bacteria and viruses [12]. Sinusitis has become a major health problem. According to the statistics from the American College of Allergy, Asthma & Immunology (ACAAI), 31 million people in the United States are yearly affected by sinusitis and more than 1 billion dollars are spent in the sinusitis treatment cases [51].

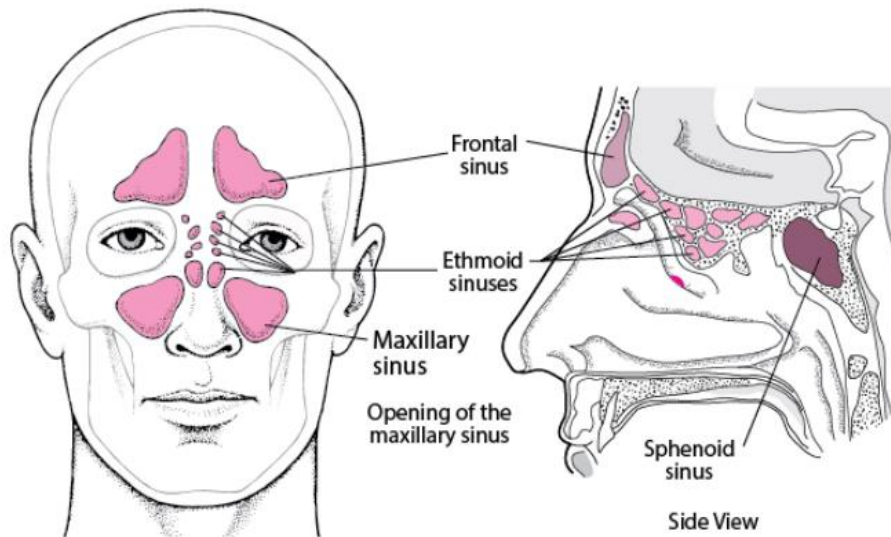


Fig. 3.4 Schematic diagram of the position of the four sinuses pairs in the human facial bones (adapted from [52]).

The instruments (GasSpectTM) we used in the sinus project were developed by the company Gasporox AB (Lund, Sweden). The instruments are constructed for

monitoring gas in food packages, while we adapted them to our sinus monitoring tasks. Figure 3.5 shows the set-up when performing the measurements. The purpose was to study the stability of the GASMAS signal in healthy volunteers and to study gas exchange following decongestant treatment. The latter study was made on a healthy volunteer and a volunteer with clinical allergic rhinitis. The receiver units and diode laser units are separate parts of the instruments, GasSpect™. A personal computer was used to collect data. The laser light was fiber-optically guided to the top of the orbita, and is injected vertically upwards. The detector is placed about 10 mm above the incidence point. The optical signal was converted into an electrical signal and transmits to the receiver unit. A tube connected to a cylinder with pure nitrogen was gently inserted into one nostril the nose to flush out the natural oxygen containing air in the nose cavity, while the volunteer was breathing normally through the mouth.

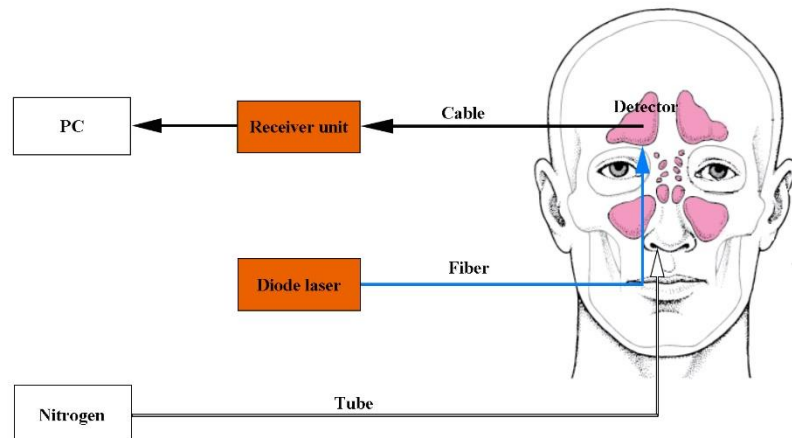


Fig. 3.5 The experimental set-up in sinus monitoring.

The experimental steps on the volunteers (healthy and with rhinitis) are the same, and are described as follows:

- Step 1: Record the sinus signal 60 times (each with 2 s interaction) in two minutes, to obtain a background signal level.
- Step 2: Start flushing pure nitrogen for 3 minutes and record data 90 times.
- Step 3: Stop flushing pure nitrogen and record data 150 times.
- Step 4: After resting for 15 minutes, spray decongestant into the nostril.

- Step 5: Continue the measurement after waiting for 5 minutes, and record the signal 60 times (2 minutes).
- Step 6: Flush the nose with pure nitrogen for 3 minutes and record the data 90 times.
- Step 7: Continue to record data 150 times (5 minutes) after stopping the flushing of nitrogen.

The recorded data are plotted in Figure 3.6. Figure 3.6 (a) presents the signal recorded from the healthy volunteer, while Figure 3.6 (b) presents the signal recorded from the affected one. The signal recorded by the computer exposes a unit of $(\% * m)$. It is the concentration C of the gas in the cavity times the effective scattering path length L in cavity gas.

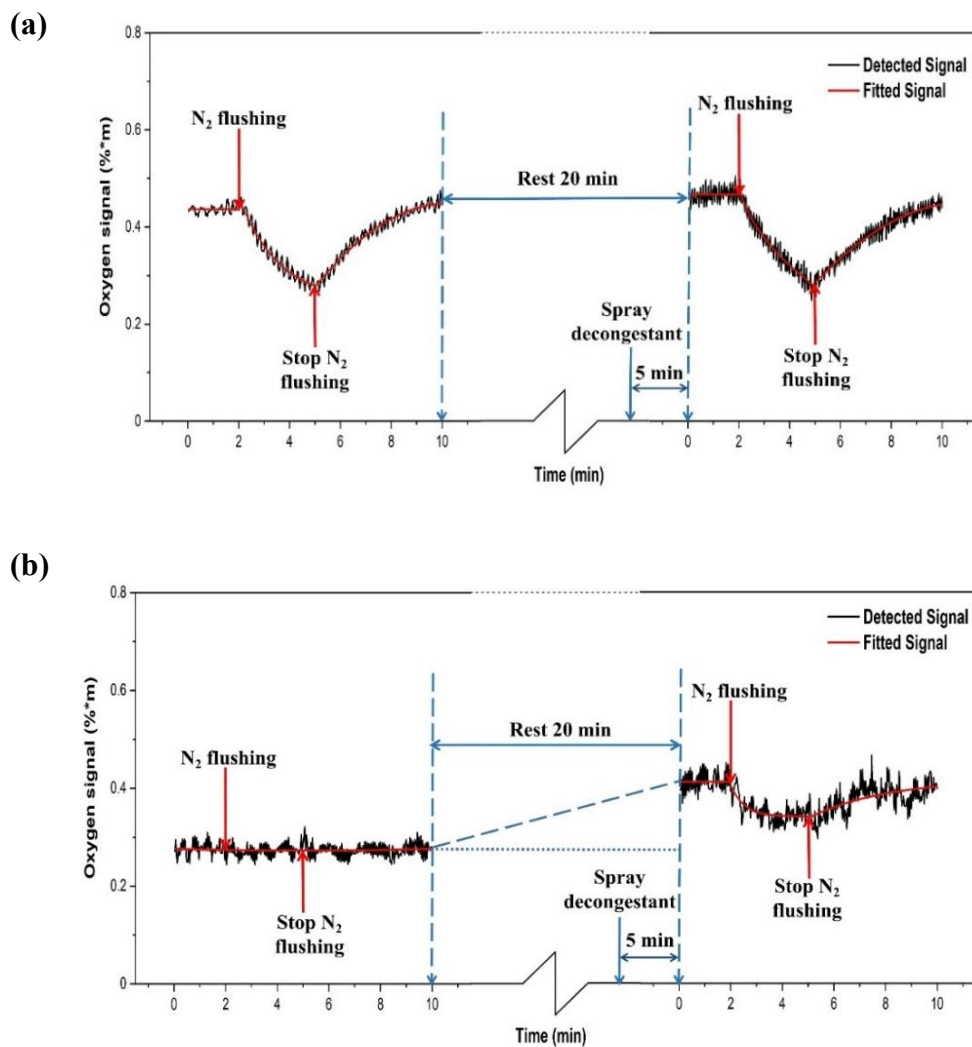


Fig. 3.6 Recorded signals in the decongestant spraying study. (a) The healthy volunteer. (b) The volunteer with rhinitis [IV].

By comparing Figure 3.6 (a) with Figure 3.6 (b), we note that the background signal level of healthy volunteer is higher than that of the affected volunteer. After flushing with nitrogen, the signal of the healthy volunteer dropped significantly, while the signal of the sick volunteer remained constant. This means that only the sinus channel of the healthy volunteer is open, while the sinus channel of the volunteer with rhinitis is blocked. The signal recovery of the healthy volunteer after stopping the flushing of nitrogen confirms this observation. After spraying the decongestant, the signal level of the patient volunteer increased significantly. In the process of a new round of nitrogen flushing, we note that the signal level of the sick volunteer began to decrease like for the healthy volunteer.

For the healthy volunteer, the signal change after spraying the decongestant is basically the same as the original signal change. This indicates that gas can be freely exchanged in and out of the sinuses of the healthy volunteer. For the affected volunteer, the background signal level increased after spraying decongestant. At the beginning, fresh air could not be exchanged freely because of the blocked sinus channel. After spraying the decongestant, the nasal sinus channel was opened, and the gas could be exchanged. When flushing nitrogen, there also are drop and rise changes. This shows that the decongestant has the effect of opening the sinus channel and more importantly that it could be monitored by the GASMAS technique.

3.2 Lung spectroscopic monitoring

We performed a feasibility study in an effort to extend earlier studies on neonatal infants to adult lung spectroscopic monitoring with a large-scale GASMAS system. Figure 3.7 (a) shows the system diagram and Figure 3.7 (b) shows a photograph of the whole system in the experiment. Tunable pulsed laser radiation around 760 nm is generated by a narrow-band dye laser (Sirah, PRSC-D-18, operated with the dye LDS765), which is pumped by the second-harmonic output of a pulsed Nd:YAG laser (Spectra Physics, PRO 290-10, 10 Hz). The pulse length of the system is 6 – 8 ns. When the laser beam enters the sample, it will be scattered, and part of the light will be detected by the

photomultiplier tube (PMT). At the same time, a small part of the light will be transmitted to the photodiode (PD) before entering the sample. The signal obtained by the photodiode can be used as a trigger or as a reference for the shape and length of the laser pulses.

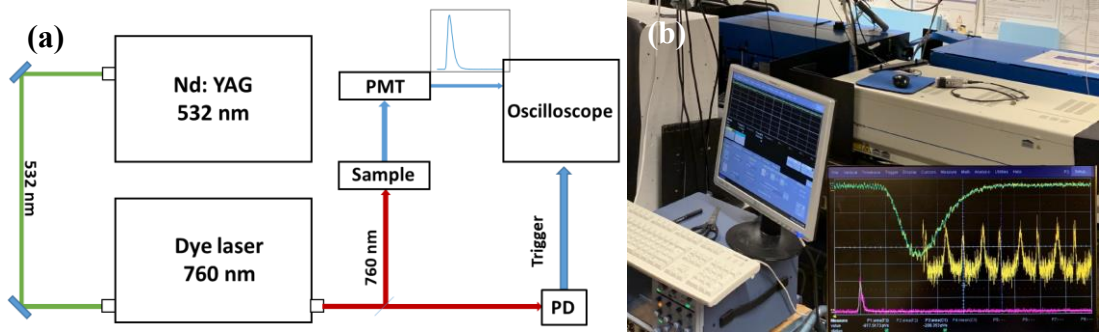


Fig. 3.7 (a) Schematic diagram of the large-scale GASMAS system. (b) Photograph of the large-scale system set-up [III].

The samples we tested consisted of polystyrene foam blocks of different sizes, as well as materials that simulate human tissues (such as chicken and pork meat). In order to reduce the influence of the indoor scattering light, we used a black plastic bag to shield the foam blocks (see Figure 3.8 (a)). Figure 3.8 presents samples we used in the measurements.

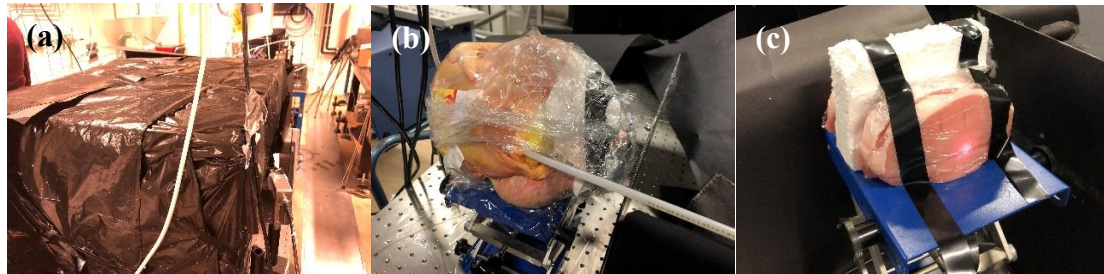


Fig. 3.8 Photographs of the samples. (a) Polystyrene foam blocks. (b) Chicken with sponge inside. (c) Thin piece of polystyrene foam surrounded by thick pork slabs.

We first measured the polystyrene foam blocks as illustrated in Figure 3.8 (a). We studied 5 foam block thicknesses: 10 cm, 20 cm, 30 cm, 40 cm and 60 cm. The time-resolved signal recorded by the photomultiplier tube (PMT) and the laser signal recorded by the photodiode (PD) are shown in Figure 3.9 (a). We note that the average path length of photons in the sample strongly increases with the thickness. The scattering path of some photons is even over 100 meters. For 40 cm thickness, we used

a solid block, as well as a stack of 10 cm blocks. By comparing the two 40 cm curves (purple and green) in Figure 3.8 (a), we can hardly see any difference, indicating that the sample surfaces have a good optical contact. In order to record the degree of scattering and absorption of photons in the sample, we studied the on-line wavelength situation and the off-line situation for each sample. The on-line situation is when the wavelength of the emitted laser is on an absorption peak of oxygen, while in the off-line situation it is close to, but off the absorption peak of oxygen. The divided large-scale GASMAS curve for on and off-resonance recordings on all block thicknesses are shown in Figure 3.9 (b). We can see that the curves basically overlap in the detectable areas. The slope of the divided curve basically follows an exponential, which is expected for a constant concentration of gas through the sample, and is a reflection of the Beer-Lambert law.

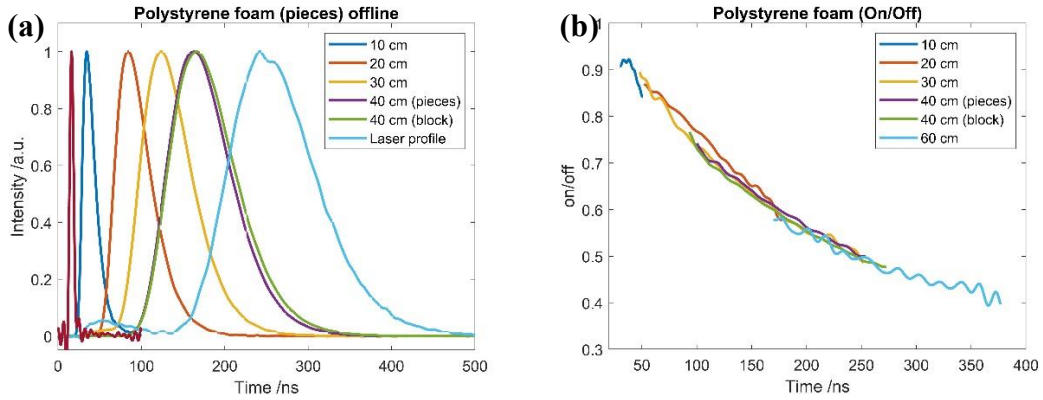


Fig. 3.9 (a) The time-resolved recording for polystyrene foam of different thicknesses, 10-60 cm. (b) Ratio curves for polystyrene foam of different thicknesses, 10-60 cm [III].

In order to further explore the possibility of large-scale GASMAS monitoring in biological tissues, we exchanged the polystyrene blocks for animal tissue samples, which are shown in Figure 3.8 (b) and Figure 3.8 (c). In Figure 3.8 (b), household sponges with a thickness of about 6 cm are inserted in the chicken. In Figure 3.8 (c), a 3 cm thick piece of polystyrene foam with two pieces of pork slabs (2 cm) on each side is shown. The time-resolved recordings of different samples are shown in Figure 3.10. We notice that there is no significant time difference in Figure 3.10 (a), while the peak delay time between the two curves in Figure 3.10 (b) is around 1.5 ns. The reason for this situation is due to the different filling materials. Compared with sponge material,

polystyrene foam has stronger scattering ability and longer average effective path of photons. A small different absorption from oxygen is also noticed for the pork sample.

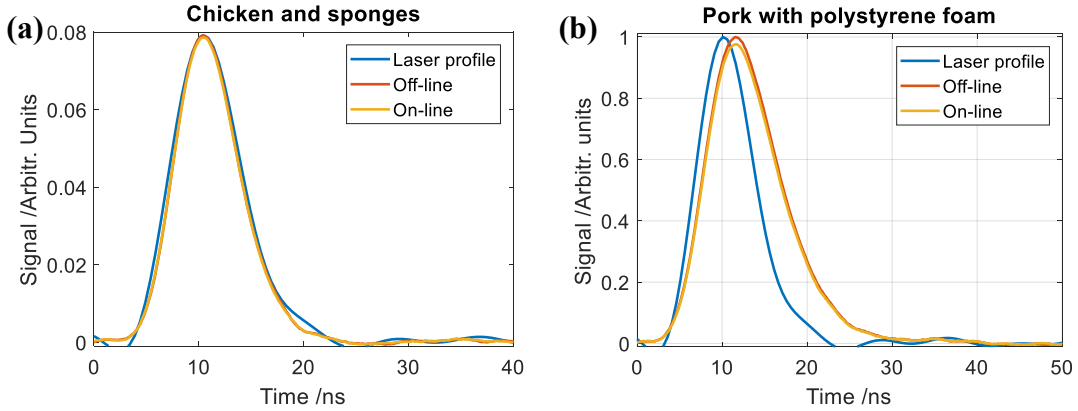


Fig. 3.10 Time-resolved recordings of different samples. (a) Chicken and sponges. (b) Pork slabs with polystyrene foam [III].

Chapter 4 Mosquito detection and analysis

In this chapter, we will present two mosquito detection approaches based on optical sensing techniques, which are optical sensors and a camera, respectively. According to the principles of the different detection approaches, we designed two detection systems, which each was placed on top of an insect trapping system. One system uses the wing-beat frequency for mosquito identification, while the other one uses image processing for feature identification. There is an electric fan at the bottom of the insect trapping system, used to achieve a high capture rate.

The *Aedes albopictus* [53], also known as the (Asian) tiger mosquito, or forest mosquito, was first discovered at a port of Houston in North America in 1895, having been introduced through the commercial trade. This mosquito species has become a significant pest in many communities because it closely associates with humans and typical flies and feeds in the daytime, in addition to dusk and dawn periods. The *Aedes albopictus* is an epidemiologically important vector for the transfer of many diseases, including yellow fever virus, dengue fever, Chikungunya fever, and others [54]. The mosquito species *Culex pipiens* is normally referred to as the common house mosquito. It usually feeds on the blood of vertebrates, but prefers the blood of birds of species that

are closely related to human interaction, such as pigeons [55]. Figure 4.1 shows two pictures of these two species of mosquito. These two species of mosquito are the two main mosquitoes analysed by our optical systems.



Fig. 4.1 The *Aedes albopictus* (left) and the *Culex pipiens* mosquito (right). Pictures downloaded from Wikipedia [56, 57].

4.1 Wing-beat frequency detection

On the basis of optical sensing principles, we designed two counting system for mosquito monitoring, including a light shading system and a light scattering system. Light emitting diodes (LED) and photodiodes (PD) are used as active light sources and detectors, respectively. Different signal amplifiers are chosen according to the specific need in the systems.

4.1.1 Shading system

The detection part of the shading system is mainly composed of four light emitting diodes (LEDs) and four photodiodes, forming an array. Due to the large divergence angle of the light emitted by the LEDs, the detection efficiency must be improved. We placed a Fresnel lens in front of each light emitting diode and each detector be able to operate with a collimate the beam in between. We placed the LEDs and photodiodes at the focus of the Fresnel lenses with focal length 25 mm. Figure 4.2 shows the improvement.

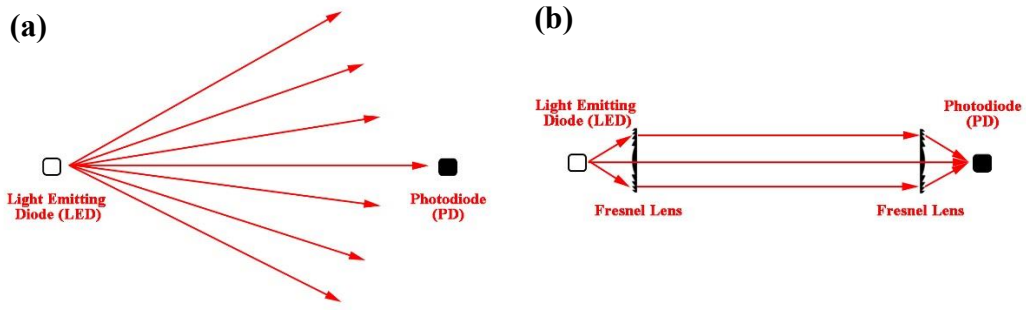


Fig. 4.2 The light path simulation.

As shown in Figure 4.2 (a), only a small part of the light emitted from the LED can without focusing reach the photodiodes because of the divergence angle. It can be seen from Figure 4.2 (b) that the divergent light beam emitted by the LED forms a parallel light beam after passing through the first Fresnel lens, and then enters the second Fresnel lens, which focuses the light on the photosensitive surface of the PD.

The lay-out of the shading system is shown in Figure 4.3. Figure 4.3 (a) gives a system overview with a cylindrical passage through in the center of the shadow counting system, where mosquitoes can enter the detection area and then be captured by the system. Figure 4.3 (b) represents the specific detection area of the system. This area contains the detectors, the LED array and the Fresnel lens groups. The LED array is composed of 4 LEDs (940 nm), and the photodiode array is also composed of 4 photodiodes.

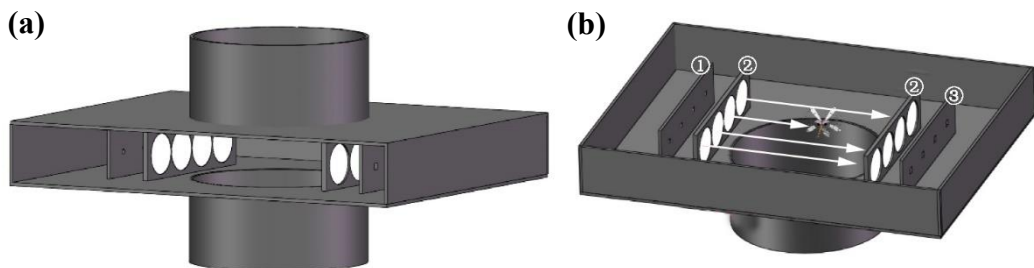


Fig. 4.3 (a) Overview of the shading system. (b) Lay-out of the detection area inside the shading system. ① Infrared LED array. ② Fresnel lens group. ③ Photodiode array [I].

If there is no moving object in the detection area, the photodiode will generate a constant photocurrent. A constant light signal cannot be amplified by the AC-coupled amplifier. When an object appears in the detection area, the photocurrent of the

photodiode will change due to the changes in light and shadow. If the object is a mosquito, the periodic vibration of the mosquito wings will cause periodic changes in the photocurrent, which will be amplified by the AC amplifier circuit. The characteristic information of the mosquito is thus detected and recorded by the system.

4.1.2 Scattering system

According to the above discussion, the mosquito signal of the shadow system is obtained by the change in light and shadow. In this case, we will get strong background light after focusing through the Fresnel lens. Clearly, there is a competition between the detection area (which must be reasonably large), and the contrast in the shadowing. After the optical signal is amplified, some of the original information (e.g., the slow body signal) will be lost. Each insect species has its own fixed range of wing vibration frequencies, and the ranges for different insects will overlap. If we only use wing-beat frequency signals to analyze mosquitoes, the accuracy we can get is limited. Backscattering of light from insects has been utilized by earlier [58-60]. The backscattered signals of insects contain body information and wing-beat frequency information at the same time and better aspects can be useful.

Our scattering system, which is shown in Figure 4.4 operates on this principle. The scattering system is placed above the shading system in a composite insect detection scheme, making possible for the two systems to observe the same insects (see Figure 4.5). The same diameter cylindrical flying channel is used in the scattering and the shading systems. The tandem arrangement increases the recognition accuracy. In order to reduce the background caused by LED stray light, we wrap a black light-absorbing cloth on the inner wall of the system. When a mosquito passes the detection area, the backscattered signal from the mosquito body and wings is recorded by the detector. The illuminating light from LEDs is impinging at right angles to the detection direction. We installed a photodiode for detecting the light scattered from the insect against the dark background of the lower section, which contains the fan. A 940nm bandpass filter is mounted in the front of the photodiode to suppress sunlight, as shown in Figure 4.4 (b).

Since the background is lower in the scattering system we can here use a DC-coupled amplifier.

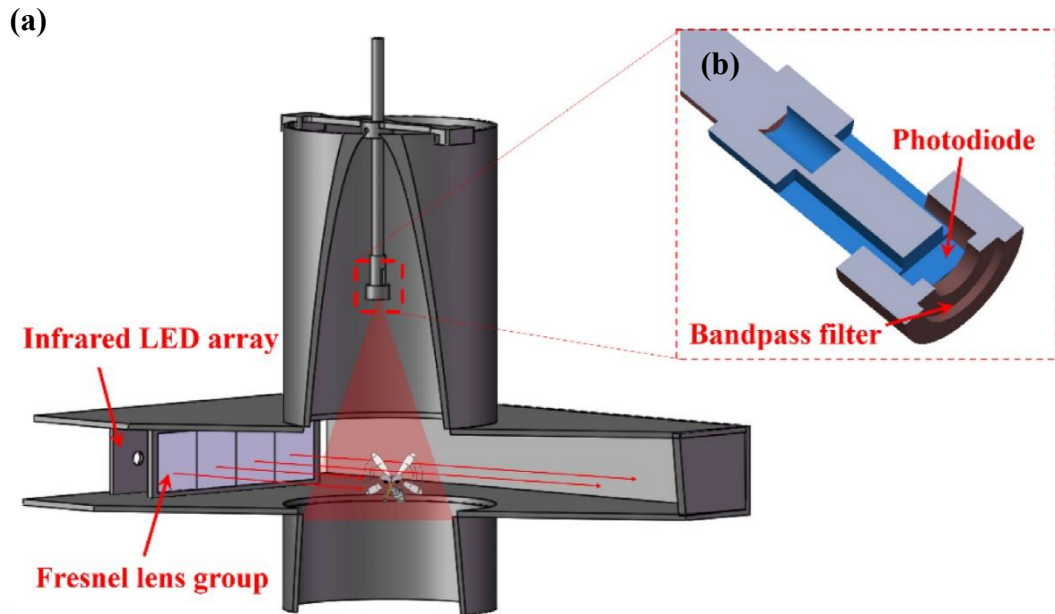


Fig. 4.4 Scattering system. (a) Schematic diagram of the system. (b) Photodiode and band pass filter installation [I].

The whole mosquito counting system is presented in Figure 4.5, including a design diagram and a photo. In Figure 4.5 (a), we show from top to bottom, the scattering system (①), the shading system (②) and the mosquito trapping system (③).

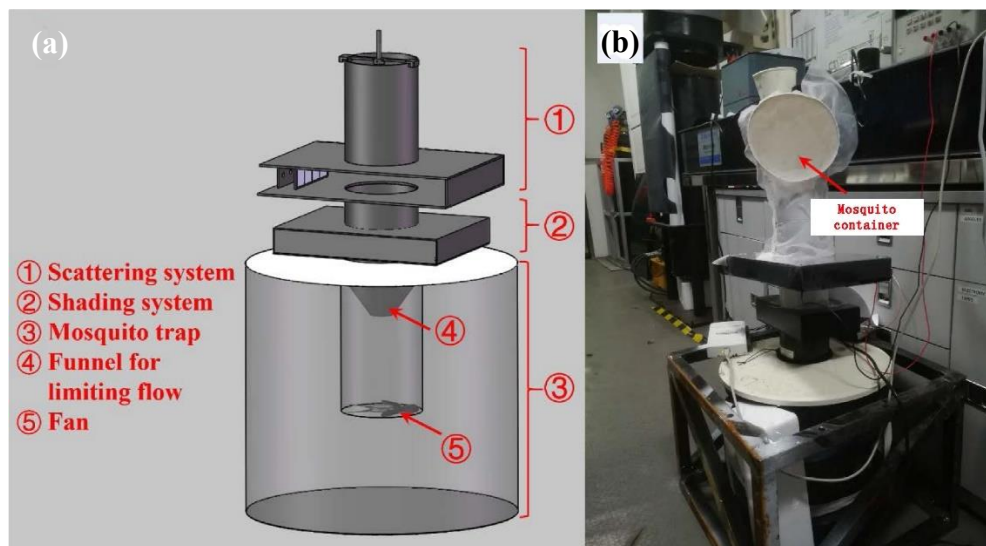


Fig. 4.5 (a) Schematic diagram of the whole mosquito monitoring system. (b) Photograph of the system [I].

4.2 Image detection

Automatic object detection is a technique related to computer vision and image processing that deals with detecting objects of a certain class in digital images and videos [61]. Methods for object detection are generally divided into two main types, which are the neural network-based or the non-neural approaches. For the non-neural approaches, features that are used in further classification would be defined firstly. There are certain methods that can carry out the tasks. For example, the Scale-invariant feature transform (SIFT), which was proposed by D.G. Lowe in 1999 [62], is a feature algorithm in computer vision to detect and describe local features in images. Histogram of oriented gradients (HOG) features [63]) constitutes another feature descriptor to count occurrences of gradient orientation in localized portions of an image. After extracting features, these features are transferred into classic classification algorithms, such as naive bayes, decision trees (DT), support vector machine (SVM) and so on, to get the classification results. For the neural network-based approaches, features are not needed to extract in the first place because it is an end-to-end approach. The word end-to-end means that once we input some samples, we will get the classification results at the end automatically without any interruptions. Generally, it is more convenient to use the neural network-based approaches.

We tried to use a camera recording method to perform preliminary classification for mosquitoes. The instrument we designed is shown in Figure 4.6, including a detection upper part (①) and a trapping lower system (②). A lamp (④) is placed on the top of the detection part, also serving as a light attractor for mosquitoes. At the same time, the lamp provides illumination for the photos captured by the camera (③). The camera is facing a black cloth (⑥), which increases the contrast between the insect and the surrounding environment during photographing, which is the same motivation as for the scattering system described above. There is a black mosquito net (⑦) in the mosquito catching system, and the fan (⑧) under the net can generate an airflow to

suck mosquitoes into the net. This combination also prevents mosquitoes from flying again in front of the camera and protect mosquitoes from being damaged by the fan.

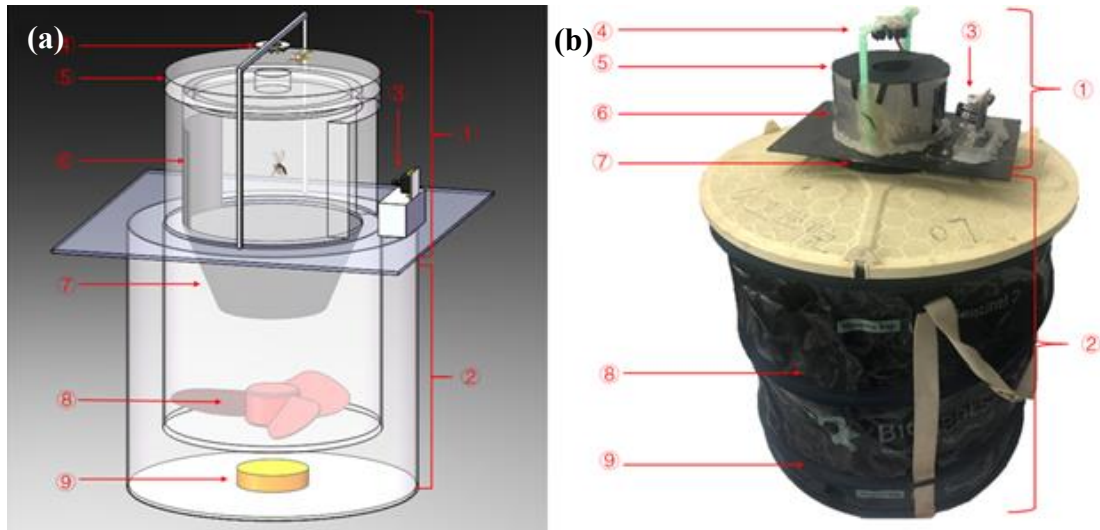


Fig. 4.6 Overview of the instrument, consisting of an image detection part (①) placed above a commercial mosquito trapping system (②). ③ is a fixed camera. [V]

An attractant (⑨) that simulates human odor is placed on the bottom of the mosquito trapping system. In operation, the lamp and the odor attractant bring mosquitoes to the instrument. Mosquitoes can enter the system through a small opening (⑤), and then be caught by the air flow produced by the fan. Before mosquitoes are stopped in the bag, the camera will record photographs of them. These photographs are transferred to a personal computer where insects can be counted and classified. Our image processing method can effectively distinguish mosquitoes from other insects, ensuring a good accuracy of the data.

4.3 Measurements and results

The experiments and data analysis for two different approaches we have chosen are presented in the following two parts.

4.3.1 Scattering system and shading system

The combination of a scattering system and a shading system not only improves the accuracy of mosquito recognition, but also can ascertain, whether mosquitoes are

captured by the system or not, through time correlation.

Some diseases can be transmitted by female mosquitoes only, such as malaria and dengue fever. Therefore, not only the species of mosquito but also the sex of the mosquito are main research aspects when monitoring mosquitoes. In the measurements, we studied the sex of the two species of mosquitoes, which we introduced in Figure 4.1; *Aedes albopictus* and *Culex pipiens*. In the upper container shown in Figure 4.5 (b), four mosquito groups *Aedes albopictus* (male, female) and *Culex pipiens* (male, female), with 65, 40, 90 and 70 individuals, respectively, sequentially were placed. The outlet of the container holding the insects is directly connected to the inlet of the counting system, and the mosquitoes inside the container transit the monitoring system.

An example of a signal recorded by the scattering system is shown in Figure 4.7 (a). Ideally, when there is no object passing by, the signal obtained by the system should be zero. However, in actual measurement, there are a lot of stray light in the system, causing a substantial background signal. Thus is the case, in spite of the fact, that we have covered the inner wall of the system with black diffusion cloth to reduce the influence of reflected light. Figure 4.7 (b) is an expanded view of the mosquito signal in Figure 4.7 (a). The red curve represents the backscattered signal from the body of the mosquito and the blue superimposed signal is due to the backscattered signal of the swinging wings. A Fourier transform operation is performed on the blue curve to get Figure 4.7 (c), which includes the fundamental frequency and harmonics of the wing-beat.

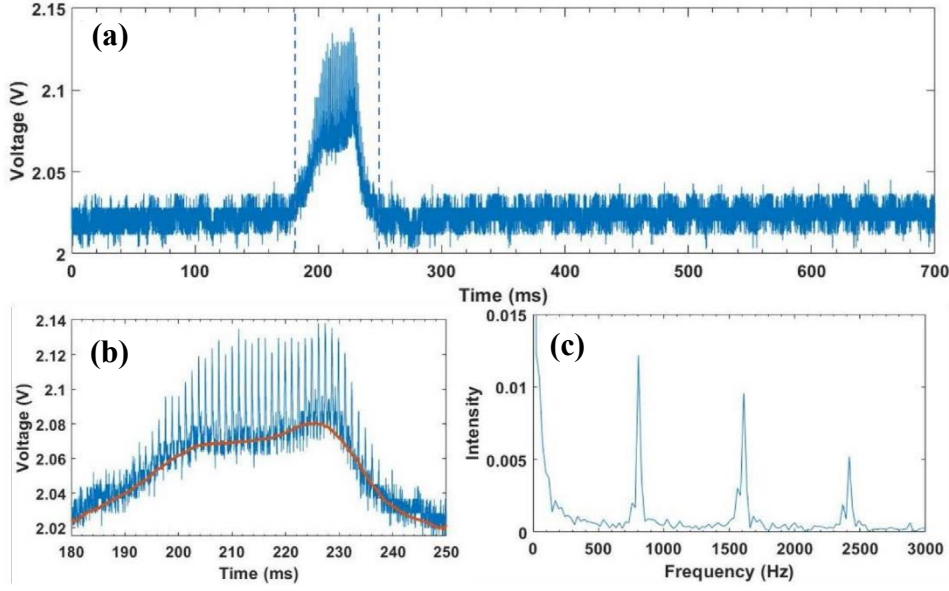


Fig. 4.7 Data from the scattering system. (a) A signal sample from the scattering system. (b) The mosquito signal within 180 ms – 250 ms. The red curve is the signal of the mosquito body and the blue one is composed of the signals from body and the beating wings. (c) Fourier transform of the mosquito wing-beat signal [I].

A signal example recorded by the shading system is shown in Figure 4.8. Two out of four photodiodes detected signals of a flying mosquito. The time sections corresponding to the mosquito signals are taken out and a Fourier transform operation is performed, and the results are shown in Figure 4.8 (b) and Figure 4.8 (c). From the results, we can see that these two signals have the same frequency information. It seems that the same mosquito was detected by two different detectors after entering, and the time difference is 50 ns.

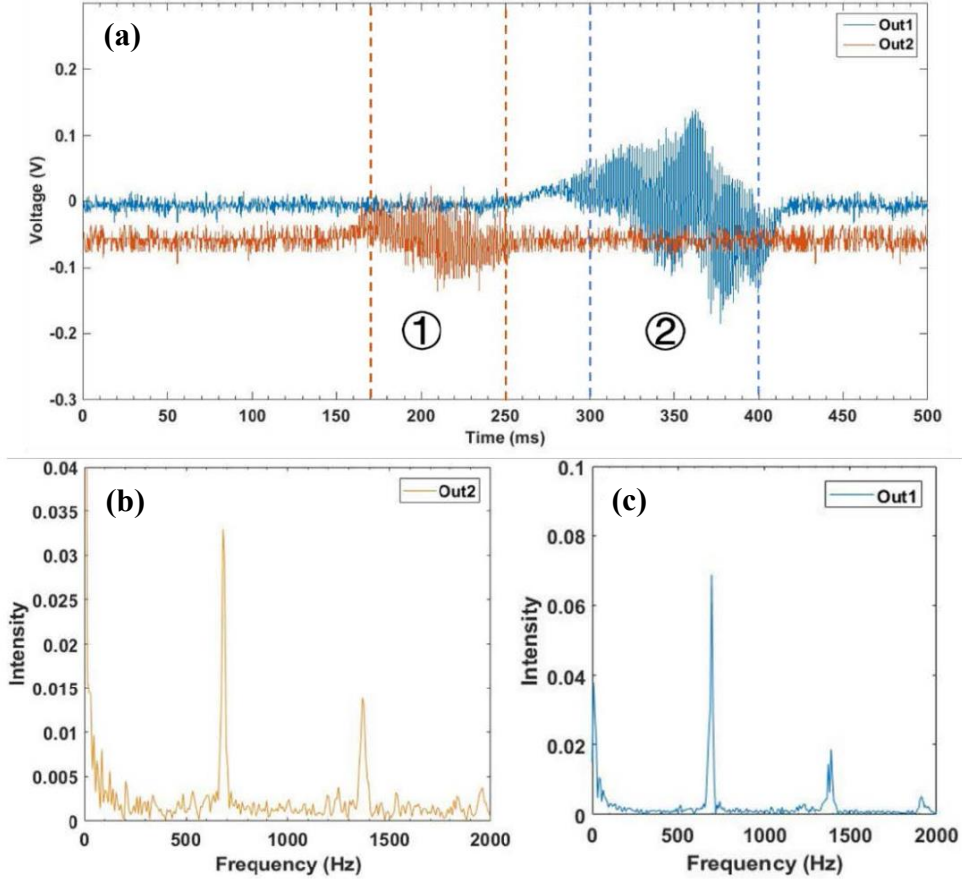


Fig. 4.8 Data from the shading system. (a) Signal samples from the shading system. (b) The Fourier transform result of ①. (c) The Fourier transform result of ② [I].

We also studied the time difference between events recorded by the two counting systems in the combined system, and detected the wing-beat frequency of the same sample. In order to evaluate the capture and counting capabilities of our system, we collected and analyzed all the data. Fig. 4.9 shows the signals of the four groups of mosquitoes recorded by the scatter counting system. Likewise, Fig. 4.10 shows the signals of the four groups of mosquitoes recorded by the shading counting system. A normal distribution fitting process is used to further analyze the sample, and the results are included in Figure 4.9 and Figure 4.10. It can be seen from the figures that the wing-beat frequencies of mosquitoes of different genders have a certain range with some small overlap. Male mosquitoes have significantly higher wing-beat frequency than that of females. Therefore, the wing-beat frequency within the *Aedes albopictus* and *Culex pipiens* species can be used as an important basis for male and female discrimination. The wing-beat frequency of *Culex pipiens* is lower than that of *Aedes albopictus*. This

may be due to the fact that *Culex pipiens* is slightly larger than *Aedes albopictus*. After comparing Figure 4.9 and Figure 4.10, we found that even for the same sample, there are small differences in the results. We believe, that these differences are caused by the specific air flow produced by the fan.

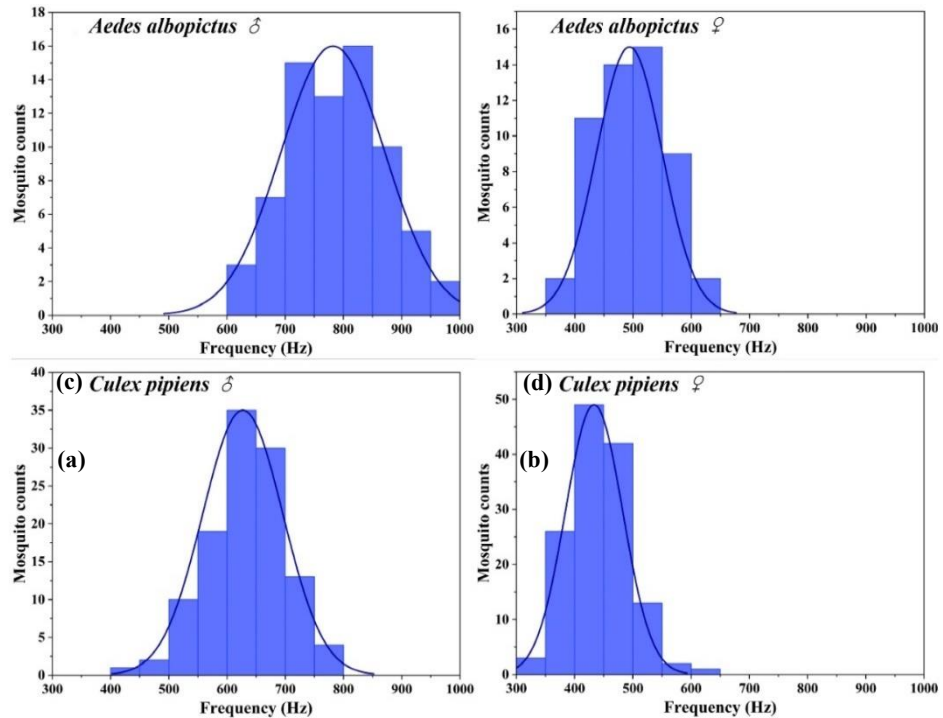


Fig. 4.9 Frequency distributions of the scattering system.

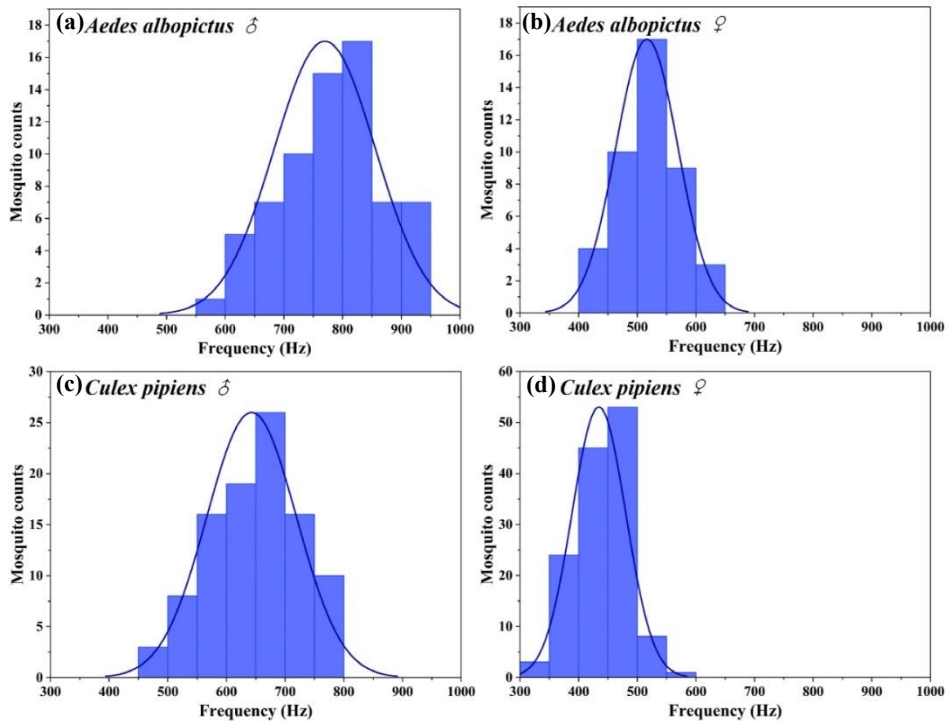


Fig. 4.10 Frequency distributions of the shading system [I].

Since mosquitoes will be caught by the internal mosquito net after passing through the detection area, the system also has the function of manual capturing and counting. As shown in Figure 4.8 (a), mosquitoes may be detected by different photodiodes more than once in the detection area, causing measurement errors. We proposed a counting method named "Method". The counting rule of "Method" is that only those signals detected by the shading system as well as the scattering system within a short time period are considered as representing a mosquito. This proposed "Method" can prevent mosquitoes from being repeatedly detected by one of these two systems. All the results are shown in Figure 4.11. Compared with the number caught by the mosquito net, the number of mosquitoes detected by the detector is higher. Compared with the two kinds of mosquitoes, *Culex pipiens* is over-represented. This may be because *Culex pipiens* is slightly larger, which makes them more resistant to the air flow with possibility to fly back and forth in the detection area. The number of mosquitoes counted by "Method" is less than the number of mosquitoes actually caught, with one exception. This may be because the density of mosquitoes in the container is relatively large and another mosquito has been recorded by the scattering system before the mosquito is recorded by the shading system.

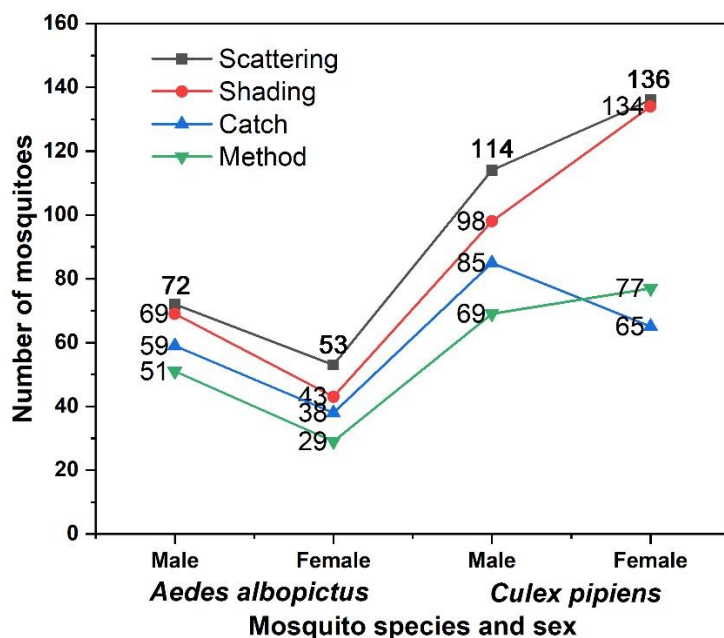


Fig. 4.11 Statistical chart of the number of mosquitoes [I].

4.3.2 Imaging system

In this section we will present a new simple and effective method with low cost and high accuracy. The main idea of our method is template matching [64], which involves a definition of a measure or a “cost” to find the “similarity” between the (known) reference patterns and the (unknown) test patterns by performing a matching operation. Many improved algorithms such as Fast Template Matching [65] and Very Fast Template Matching [66] were presented with high speed and better performance. However, the biggest limitation of these methods is that only one single object can be detected at a time. In real life, the probability of one single target detection event is much smaller than the probability of multi-target events. So, we improved the single template matching algorithm to make it adapt to the task of multi-target detection.

We here present the process steps to detect and classify mosquitoes from other insects captured by the camera. Bees were chosen as an example of a specie, to be discriminated against. The specific calculation process is as follows:

- Step 1: Convert the image sample (pixels: 1280*960) from RGB (red, green and blue) into grayscale.
- Step 2: Cut out the template (pixels: 200*144) from one sample image, as shown in Figure 4.12 (a). Perform padding operation to another sample image. The padding operation means to increase length and width of the sample image with the length and width of the template to make the new image (pixels: 1480 * 1104), as shown in Fig. 4.12 (b). Through the padding operation, the target at the edge of the image will be detected by the algorithm.

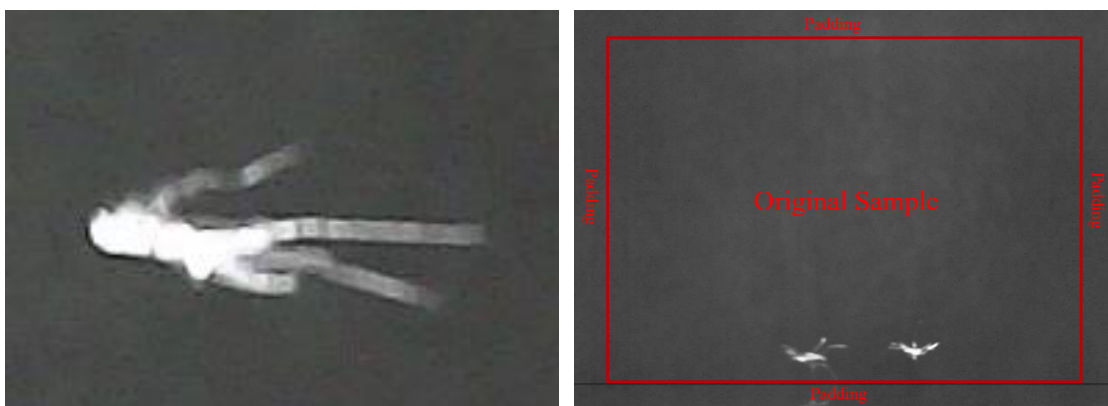


Fig 4.12 (a) Template image. (b) Image sample after padding [V].

- Step 3: Align the template with the upper left corner of the image sample. Calculate the similarity between the template and the area covered by the template (the Region of Interest, ROI). The correlation coefficient r_{ccoeff} is calculated as follows:

$$r_{ccoeff}(x, y) = \sum_{x', y'} I'_T(x', y') * I'_{ROI}(x + x', y + y') \quad 4.1$$

Here, x and y are the pixel location information in the image sample, $0 \leq x < 1280$ and $0 \leq y < 960$. x' and y' are the pixel location information in the template, $0 \leq x' < 200$ and $0 \leq y' < 144$. We further calculate I'_T :

$$I'_T(x', y') = \frac{I_T(x', y') - \frac{\sum_{x'', y''} I_T(x'', y'')}{W * H}}{\sqrt{\sum_{x'', y''} I_T^2(x'', y'')}} \quad 4.2$$

$I_T(x', y')$ is the intensity of the pixel, which locates in (x', y') of the template image. x'' and y'' are also the pixel location information in the template, $0 \leq x'' < 200$ and $0 \leq y'' < 144$. W and H are the width and height of the template, which are 200 and 144, respectively. Equation 4.2 is actually a normalization process. By subtracting the mean and dividing by the variance, it is guaranteed that the particular light intensity will not affect the calculation results.

Further, I'_{ROI} is calculated as:

$$I'_{ROI}(x', y') = \frac{I_{ROI}(x', y') - \frac{\sum_{x'', y''} I_{ROI}(x'', y'')}{W * H}}{\sqrt{\sum_{x'', y''} I_{ROI}^2(x'', y'')}} \quad 4.3$$

$I_{ROI}(x', y')$ is the intensity of the pixel, which locates in (x', y') of the ROI region. x'' and y'' are also the pixel location information in the template, $0 \leq x'' < 200$ and $0 \leq y'' < 144$. Again, W and H are the width and height of the template, which are 200 and 144, respectively.

- Step 4: Move the template one pixel to the right and repeat the calculation in Step 2 until the template arrives to the far right.
- Step 5: When the template arrives the far right, move it one pixel down and repeat the calculation in Step 3 and Step 4 from the far left.
- Step 6: After the loop calculation of step 4 and step 5, a new matrix R_{ccoeff} of

dimension (pixels: $(1480-200+1) * (1104-144+1)$) is produced, composing of the calculated correlation coefficient r_{ccoeff} values. With the calculations in Equation 4.3 and Equation 4.4, the value of r_{ccoeff} is limited between 1 and -1. The higher r_{ccoeff} , the greater matching degree is. Then the maximum value, the minimum value and maximum position information in the matrix R_{ccoeff} are chosen. A threshold value of 0.4 is defined. When the calculated correlation coefficient is bigger than the defined threshold, we consider that a target is detected.

- Step 7: Centering on the coordinates of the maximum, an area, which has the same size (pixels: $200 * 144$) as the template in the original image (pixels: $1280 * 960$) is placed. Normalization, binarization and morphological processing are carried out for the region within the original area to obtain the contour of the object. Then we calculate the area and perimeter of this contour and divide the perimeter by the area to get the ratio.
- Step 8: Covering procedure is performed in the matrix R_{ccoeff} . The covering operation means replacing the area in step 7 with the minimum value from step 6. Then repeat the process in Step 7 and Step 8 until the maximum value is smaller than the threshold.

One hundred and twenty two insect images arranged to include 71 mosquito images, and 51 bee images were recorded by the instrument to evaluate the performance of these three types of detection algorithms and the degree of improvement. Single template matching is the primary aspect of our proposed method. However, signal template matching cannot deal with multi-objects tasks, which is more common in daily life. The idea of improvement is that once an object is detected by the algorithm, the pixel values around the object belong to the same object. In multi-object detection tasks, an object should not be detected more than once, which means that the pixel value around the object should be eliminated by the algorithm. Thus, multi-target template matching can be performed after covering operation. As a defect of template matching, objects falling on the edge of the image are difficult to be detected by the algorithm. In order to further improve the detection efficiency, a padding operation was introduced

to Multi-target template matching, which is the third algorithm we proposed.

Some examples of the results from these three different algorithms are shown in Figure 4.13 and Figure 4.14. By comparing two photos in Figure 4.14, we can see that more than one target can be detected after covering. After the padding operation, there are more pixels near the target that can be used when calculating (see Figure 4.15 (b)).

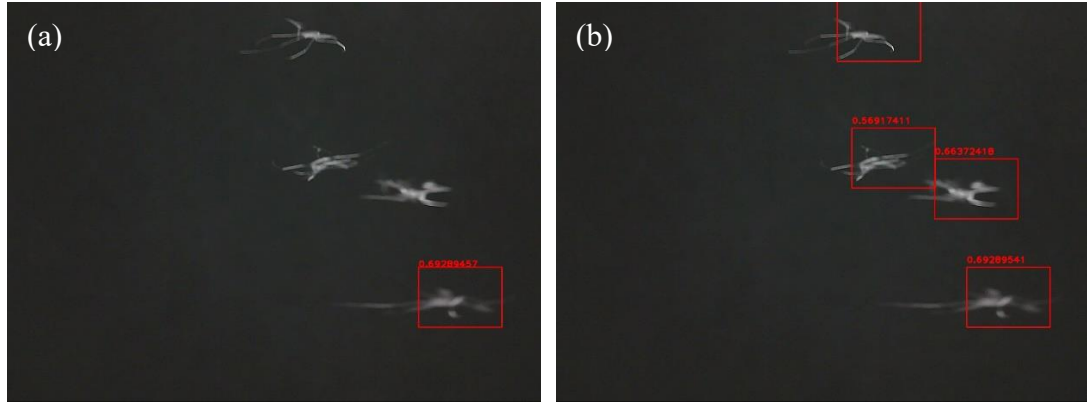


Fig. 4.13 (a) Single template matching. (b) Multi-target template matching. [V]

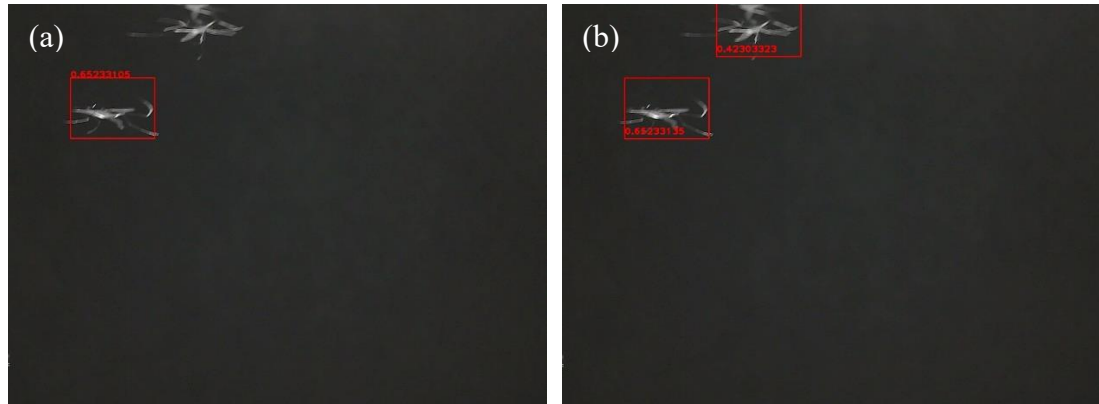


Fig. 4.14 (a) Before padding. (b) After padding [V].

Table 4.1 shows the different detection rates for these three algorithms, which includes Single template matching, Multi-target template matching and our proposed detection algorithm. After our improvements, the detection rate reaches 92% from initially 64%.

Table 4.1 Performance of different algorithms [V].

| Algorithm type | Template matching | Covering | Padding | Detection rate |
|---|-------------------|----------|---------|----------------|
| Single template matching algorithm | √ | ✗ | ✗ | 64% |
| Multi-target template matching algorithm | √ | √ | ✗ | 84% |
| Our proposed algorithm | √ | √ | √ | 92% |

In step 7, a set of processes were performed with the ROI to classify mosquitoes and bees. The process details are displayed in Figures 4.15 and 4.16. From Figures 4.15 (d) and 4.16 (d), the body area of a bee is much larger than that of a mosquito. Seeing from the contour shape of the mosquito, the mosquito has a longer perimeter and a smaller area. Perimeter means the number of pixels contained in the edge of the range, while area means the number of all the pixels contained within the contour. A bee recorded by the camera may have similar perimeter as a mosquito but a larger area. At the end of the process, only those targets classified as mosquitoes by the algorithm will be colored (see Figures 4.15 (e) and 4.16 (e)). After determining the area and the perimeter of the target in the ROI, we decided two ways to present and the results, as plotted in Figure 4.17. From Figure 4.17 (a), the Perimeter/Area ratio curves of mosquitoes and bees are basically separate from each other. However, in Figure 4.17 (b), Perimeter²/Area ratio curves slightly intersect with each other. The calculation to Figure 4.17(b) is dimensionless [67]. The ratio calculation between the perimeter and the area also relies on the size, while the calculation between the square of perimeter and the area relies on shape only. By comparing these two results, taking also the size into account gives better performance.

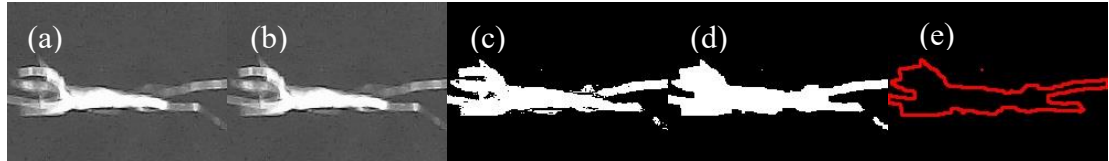


Fig. 4.15 Processed sample of mosquito. (a) Original ROI; (b) Normalization; (c) Binarization; (d) Morphological processing; (e) Classification results [V].

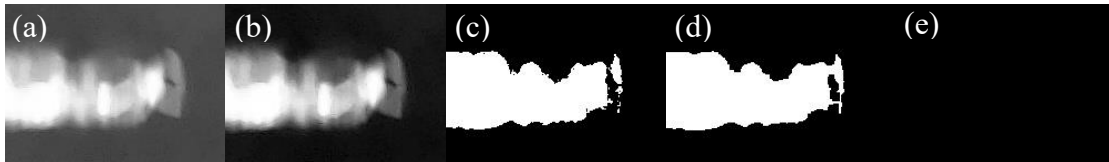


Fig. 4.16 Processed sample of bee. (a) Original ROI; (b) Normalization; (c) Binarization; (d) Morphological processing; (e) Classification results [V].

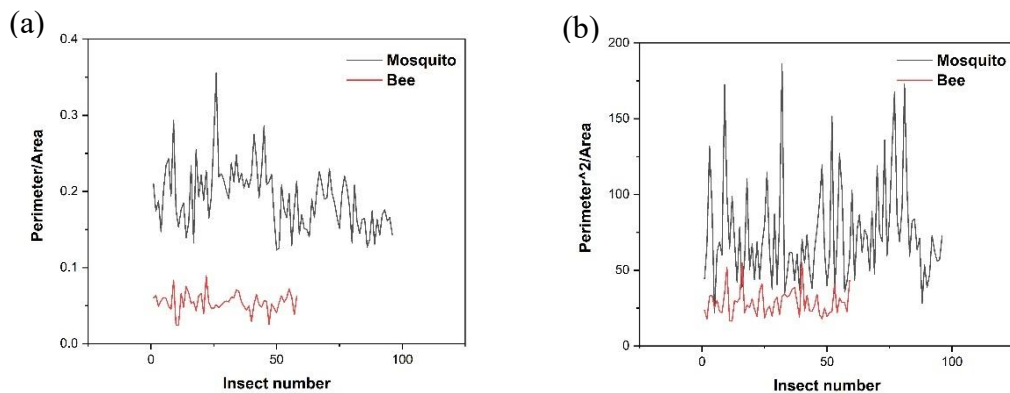


Fig. 4.17 (a) The Perimeter/Area ratio curves of mosquitoes and bees. (b) The Perimeter²/Area ratio curves of mosquitoes and bees [V].

In order to further evaluate the classification power more accurately, several evaluation indices are introduced as shown in Eqs (4.4 - 4.6). TP, FN, FP are defined as follows:

TP: True positive, which means that objects were detected as mosquitoes and they are mosquitoes.

FN: False negative, which means that objects are mosquitoes but they are not detected as mosquitoes.

FP: True negative, which means that objects were detected as mosquitoes but are not mosquitoes (which could be absence of insects, or a bee).

Then Recall, Precision and F-measure values can be calculated as follows:

$$Recall = \frac{TP}{TP + FN} \quad 4.4$$

$$Precision = \frac{TP}{TP + FP} \quad 4.5$$

$$F - measure = 2 * \frac{Precision * Recall}{Precision + Recall} \quad 4.6$$

There can be contradictions between Recall and Precision. F-measure is defined as a harmonic mean of Recall and Precision [68]. The higher the F-measure is, the better performance will be. The calculation results are presented in Table 4.2. No Classification means that we only used the detection method, while Classification means that we used the detection method and the classification method at the same time. All the values of the indices are increased by adding the classification method.

Table 4.2 Performance of different methods.

| Methods | TP | FN | FP | Recall | Precision | F-measure |
|-------------------|----|----|----|--------|-----------|-----------|
| No Classification | 86 | 14 | 13 | 86.0% | 86.8% | 86.4% |
| Classification | 93 | 6 | 7 | 93.9% | 93.0% | 93.5% |

Chapter 5 Foreground scattering elimination

We put forward a concept of inverse lock-in-like spatial modulation (ILLSPAM), aiming at vision enhancement. Like for all the other projects introduced in this thesis, we are dealing with light scattering. The present project relates to a common experience in life. When human beings focus on a static object, the brain can lock to the target of interest and automatically ignore the external environment. The information processing function of the brain can conditionally segment the image information, sequentially received by the eye, and store the target "fragments" of interest. Then, in the time dimension, these fragments are linked together to form a complete target, which forms the object captured in our brains. In the psychology branch of Gestalt thinking, experienced phenomena consist of part–whole structures, configurations, or Gestalten [69]. A Gestalt is an integrated, coherent structure or form; a whole that is different from the sum of the parts [69, 70].

There are usually some obstructions between the eye and the target, such as cars on the road and trees swaying in the wind. Sometimes the cause of vision impairment is the scattering of the transmission medium, such as structured windows with scattering,

enhanced by direct forward sunlight (see forward Mie scattering in Figure 2.4). At this time, we suggest to periodically adjust the position of the and head to reduce vision impairment and obtain more information about the target, by separating it from the background. Figure 5.1 illustrates a situation when driving. The vision of the driver is severely impaired due to the impact of strong sunlight, or due to the head-lights of a vehicle approaching at night time. Interesting objects, such as animals and humans, are in a distance, as shown in Figure 5.1 (a). Figure 5.1 (b) shows the close foreground scene with scattering dirt on the windscreen. Figure 5.1 (c) is made up of the background objects in Figure 5.1 (a) and foreground scene in Figure 5.1 (b). In order to better rebuild the objects in the background, we need to separate the two scenes. The method is to periodically move the foreground up and down a few centimeters, and focus on observing the non-moving part of the picture, which is the background.

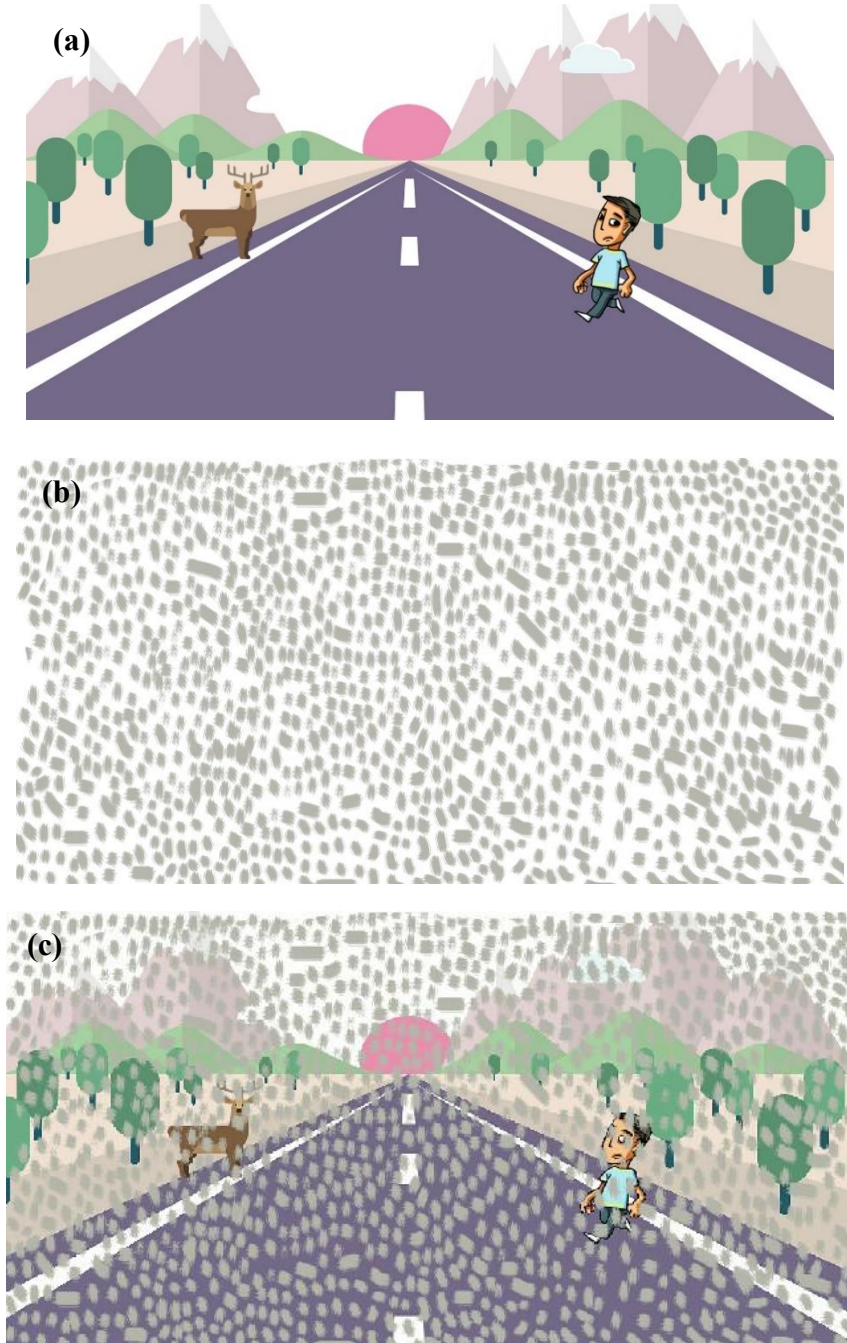


Fig. 5.1 Illustration how vision impairment sometimes occurring during car driving can be improved by a simple spatial modulation approach. (a) The scene of the background we want to observe. (b) Foreground scene with scattering dirt. (c) The impaired vision image obtained from the superposition of (a) and (b) [II].

Many image processing methods have been developed to remove the foreground and reconstruct the background; see, e.g., [70-76, 39]. The new physiological method we proposed will be presented through an illustrative example, which was recorded with a standard smartphone. The digital processing method we used in our

demonstration is based on two already known methods, the Gaussian Mixture Model (GMM) and the Interframe Difference Method.

5.1 Gaussian Mixture Model (GMM)

The Gaussian distribution, which is sometimes called the normal distribution, is a common form of distribution that frequently exists in nature. A single Gaussian model (GSM) is a data model with a Gaussian distribution. The probability density function formula of a single Gaussian distribution (GSM) is as follows:

$$p(x) = \frac{1}{(2\pi\sigma^2)^{\frac{1}{2}}} e^{-\frac{(x-\mu)^2}{2\sigma^2}} \quad 5.1$$

Here, the parameter μ ($-\infty < \mu < +\infty$) represents the mean value, and the parameter σ ($0 \leq \sigma$) represents the standard deviation. The formula can also be described as $x \sim \mathcal{N}(\mu, \sigma^2)$. The mean value corresponds to the middle position of the normal distribution. 95% of the data are distributed within 2σ around the mean in the intensity domain.

The Gaussian Mixture Model (GMM) is an extension of a single Gaussian probability density function, which uses multiple Gaussian probability density functions (normal distribution curves) to accurately distribute the variables, and it decomposes the variable distribution into several Gaussian functions. The probability density function formula of a Gaussian mixture distribution (GMM) is as follows:

$$p(x) = \sum_{i=1}^K \omega_i \cdot \frac{1}{(2\pi\sigma_i^2)^{\frac{1}{2}}} e^{-\frac{(x-\mu_i)^2}{2\sigma_i^2}} \quad 5.2$$

Here, K is the number of single Gaussian models (GSM) in the Gaussian mixture model. μ_i and σ_i are the mean value and standard deviation of the i -th ($0 < i \leq K$) single Gaussian, respectively. ω_i is a weight parameter, which is positive and corresponding to the importance of the i -th single Gaussian model. The sum of all weights in the Gaussian mixture model must be equal to 1. The formula can also be described as $x \sim \mathcal{N}(\mu, \sigma^2, K)$.

Figure 5.2 is a visualization of the relationship between the Gaussian mixture

model and the individual Gaussian models with different weights that compose it. The solid line represents the Gaussian mixture model and the dotted lines represent the single Gaussian models.

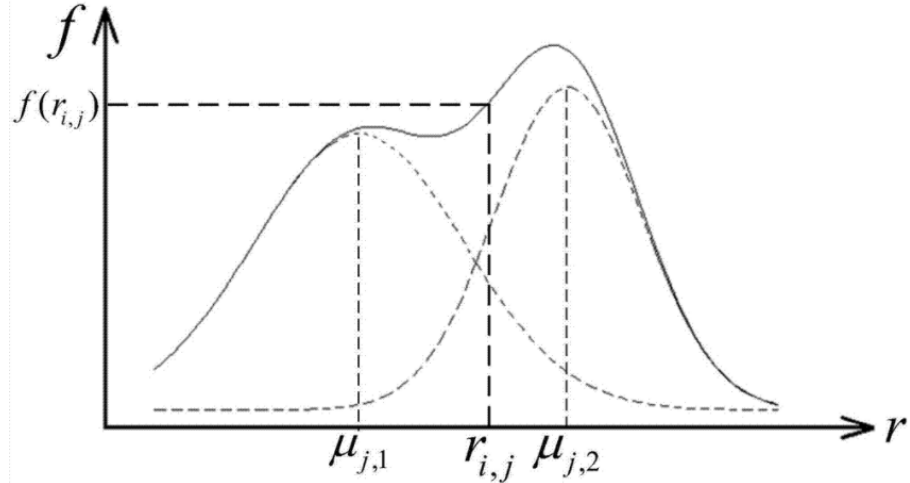


Fig. 5.2 Visualization of the Gaussian mixture model (solid) and the single Gaussian models (dashed) that compose it.

Usually, the Gaussian mixture model (GMM) is used for clustering problems of one-dimensional data. Through iterative processing, the best parameters are found for data clustering. However, in two-dimensional data (image processing), the Gaussian mixture model is more adequate. The Gaussian mixture model is usually used in image segmentation tasks or background reconstruction tasks. Figure 5.3 is a visualization of a Gaussian mixture model applied in background reconstruction tasks.

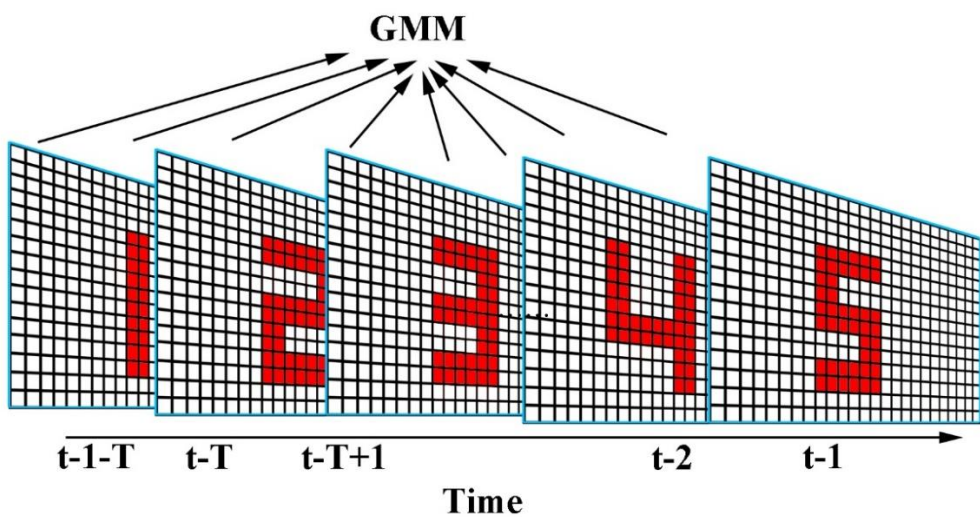


Fig. 5.3 Visualization of a Gaussian mixture model applied in background reconstruction tasks.

An image is composed of tens of thousands of pixels. In Figure 5.3, different timestamps correspond to different images. Rather than explicitly modeling the values of all the pixels in an image as one particular type of distribution, the GMM models the values of a particular pixel as a mixture of Gaussians [77]. The calculation steps of the Gaussian mixture model are as follows:

- Step 1: Take the pixel at position (0,0) as an example, a data set of intensity χ_{T-1} will be generated after a time period of T, which means $\chi_{T-1} = \{x_{t-1}, \dots, x_{t-1-T}\}$. (Here x_{t-1} is the current pixel value at time t-1). A Gaussian mixture modeling operation was performed on this data set χ_{T-1} to achieve clustering operations, and find the optimal solution after iteration. The probability of observing the current pixel value $p(x)$ is:

$$p(x) = \sum_{m=1}^M \omega_m \cdot \eta(x, \mu_m, \sigma_m^2) \quad 5.3$$

Here, M is the number of single Gaussian models (GSM) in the Gaussian mixture model. (Currently, from 3 to 5 are used.). Again, the ω_m values, which are positive and estimate the mixing weights, add up to one. μ_m and σ_m^2 are the mean value and the estimate of the variance of the m-th ($0 < m \leq M$) Gaussian, respectively. η is a Gaussian probability density function:

$$\eta(x, \mu, \sigma^2) = \frac{1}{(2\pi\sigma^2)^{\frac{1}{2}}} e^{-\frac{(x-\mu)^2}{2\sigma^2}} \quad 5.4$$

- Step 2: When a new frame occurs at time t, the relative new intensity value $x^{(t)}$ of the corresponding position (0, 0) will be used to match the M models in the Gaussian mixture model. If the difference between the new intensity value $x^{(t)}$ and the mean value of a certain model is less than $2.5 \sigma_m$ ($|x^{(t)} - \mu_{m,t-1}| \leq 2.5 \sigma_{m,t-1}$), we define that this pixel belongs to a background pixel and go to the step 3.
- Step 3: Define a learning rate α ; at this time all the weights of the single Gaussian model must be updated. The update calculation process is as follows:

$$\omega_{m,t} = (1 - \alpha) * \omega_{m,t-1} + \alpha * N_{m,t} \quad 5.5$$

For the certain model that matched, $N_{k,t} = 1$; while $N_{k,t} = 0$ for the rest single Gaussian models. After updating, a normalization operation will be applied for all the weights.

At the same time, the internal parameters of the matched model will be updated according to the following formula:

$$\rho = \alpha / \omega_{m,t} \quad 5.6$$

$$\mu_{m,t} = (1 - \rho) * \mu_{m,t-1} + \rho * x^{(t)} \quad 5.7$$

$$\sigma_{m,t}^2 = (1 - \rho) * \sigma_{m,t-1}^2 + \rho * (x^{(t)} - \mu_{m,t})^T (x^{(t)} - \mu_{m,t}) \quad 5.8$$

The parameters of the rest of single Gaussian models remain the same.

- Step 4: If no matching model is found in step 2, the certain single Gaussian model with smallest weight will be updated, with a distribution with the current value x_t as its mean value, and initially high variance, and low prior weight.
- Step 5: Sort the models according to the value of $\omega_{m,t} / \sigma_{m,t}$, and choose the first B models as the background model, where:

$$B = \operatorname{argmin}_b \left(\sum_{m=1}^b \omega_{m,t} > P \right) \quad 5.9$$

P is a measure of the minimum portion of the data that should be accounted for by the background.

Step 1 to step 5 are the specific calculation processes of the Gaussian mixture model in the background modeling task. All pixels in the image will be calculated and modeled separately, as expressed in steps one to five. GMM is a robust, adaptive method that is flexible enough to handle variation in lighting, moving scene clutter, and so on.

5.2 Interframe Difference Method

Compared with the complex Gaussian mixture model, the interframe difference method [78] is the simplest and most direct method in the background modeling task. In two adjacent frames, if a certain pixel belongs to the background, then the values between

the two corresponding pixels in these two frames will be similar to each other. This is the main principle of the interframe difference method. Figure 5.4 shows a visualization of a interframe difference method.

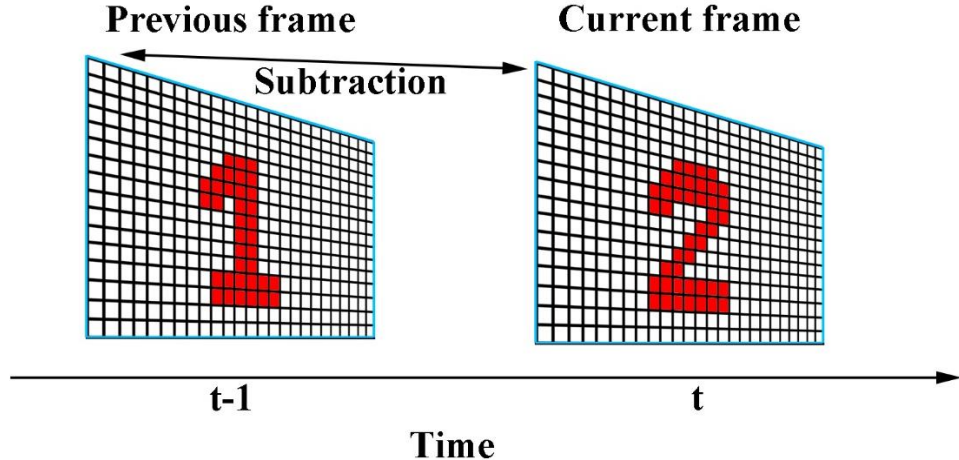


Fig. 5.4 Visualization of the interframe difference method

The background modeling equation of the interframe difference method is presented as follow:

$$x_t = \begin{cases} \text{Background}, & \text{if } |x_t - x_{t-1}| \leq H \\ \text{Foreground}, & \text{if } |x_t - x_{t-1}| > H \end{cases} \quad 5.10$$

Here x_t means the pixel value of the current frame and x_{t-1} means the pixels of the previous frame. H is given at first as a threshold value.

The advantages of the interframe difference method is that it is simple to operate, and the program design complexity is low; it is not sensitive to scene changes such as light, it can adapt to various dynamic environments, and has relatively strong robustness. The disadvantage is that the complete area of the object cannot be extracted. When the moving range of the object is small relative to the outline of the object, there will often be holes inside the object, and only the boundaries of objects can be extracted. In the calculation result, the boundary of the object is usually larger than the actual object.

5.3 Measurements and results

5.3.1 System set-up and image process

A simple laboratory set up is shown in Figure 5.5. A smartphone camera is fixed on a table. A transparent screen cluttered with an irregular pattern of scattering grey spots is moving periodically, 0.5 m from the camera. The object of interest in our case (the participating university badges) is placed 1 meter away from the camera. The function of the camera is to simulate the vision seen by the human eye, and the regularly moving transparent screen represents the scattering medium that causes vision impairment.



Fig. 5.5 The laboratory setup, including the objects, the obscuring foreground screen and the smartphone camera. (left) schematic setup, and (right) a photograph of the setup [II].

Image samples were collected by the smartphone camera. Then a sample vision enhancement process based on a Gaussian mixture model (GMM) and the interframe difference method was operated. We operated an interframe action based on the result obtained from GMM. The process steps are shown as follows:

- Step 1: A time period T was defined in the beginning to increase the adaptability of the training set. To prevent excessive computation time or possible motion, T should not be chosen too long. At time $t-1$, calculate the pixel data set generated in the time period T by following the steps in section 5.1 to obtain a temporary Gaussian mixture background. The pixel intensity of the temporary Gaussian mixture background $TB_{t-1}(x, y)$ is composed of the product of the weight and the

mean value of each single Gaussian model. Thus:

$$x_{TB,t-1} = \sum_{m=1}^M \omega_m * \mu_m \quad 5.11$$

Here, $x_{TB,t-1}$ means the pixel value in the temporary Gaussian mixture background. M means the number of single Gaussian model (GSM) in the Gaussian mixture model. The ω_m values estimate the mixing weights and μ_m are the mean value of the m-th ($0 < m \leq M$) Gaussian model.

- Step 2: At time t, a new frame comes and the following calculation is made for all the pixels. Convert the current frame $f_t(x, y)$ and the temporary Gaussian mixture background $TB_{t-1}(x, y)$ at time t to gray images $f_{t,g}(x, y)$ and $TB_{t-1,g}(x, y)$. A subtraction operation is performed between these two images. If the distance between the pixel in $f_{t,g}(x, y)$ and the corresponding pixel $TB_{t-1,g}(x, y)$ is smaller than an adaptive threshold H, this means that the current pixel can be considered as a background pixel. The gray frame can be divided into gray foreground and gray background according to the following relation:

$$f_{t,g}(x, y) = \begin{cases} B_g(x, y), & \text{if } |f_{t,g}(x, y) - TB_{t-1,g}(x, y)| \leq H \\ F_g(x, y), & \text{if } |f_{t,g}(x, y) - TB_{t-1,g}(x, y)| > H \end{cases} \quad 5.12$$

- Step 3: We reconstruct the current background $B_t(x, y)$ after the subtraction operation based on the background $B_{t-1}(x, y)$ corresponding to the previous frame. The new background $B_t(x, y)$ can be obtained as follows: Based on $B_{t-1}(x, y)$, we update the pixels which locate in the area of $B_g(x, y)$ in function 5.12 by using the pixel values, which are in the same location in the current frame $f_t(x, y)$. The other pixels, which are located in the area of $F_g(x, y)$, remain the same. Th relation is shown as follow:

$$B_t(x, y) = \begin{cases} B_{t-1}(x, y), & \text{if } f_{t,g}(x, y) = B_g(x, y) \\ f_t(x, y), & \text{if } f_{t,g}(x, y) = F_g(x, y) \end{cases} \quad 5.13$$

- Step 4: Update the parameters of the Gaussian mixture model according to Eqs 5.5 – 5.8 and get a new temporary Gaussian mixture background model $TB_t(x, y)$. When a new frame occurs at time t+1, loop steps 1 through 3 to update the

background.

5.3.2 Discussion of results and evaluation

As discussed above, a background image will be generated by the calculation and displayed by the system. Figure 5.6 shows the same image before and after the process, respectively. Figure 5.6 (a) is an individual frame, where parts of the object of interest were blocked, while Figure 5.6 (b) shows a processed image, which is free of obstruction.



Fig. 5.6 (a) Individual frame and (b) a digitally processed image [II].

The inter-frame difference method is a commonly used method in motion detection, but it is not sensitive to slow-moving targets. However, the inter-frame difference method is simple and has good stability to light changes. The Gaussian mixture model collects specific pixel intensity information in a fixed period of time. If the target moves

slowly, it will be incorrectly classified as background information. At the same time, the Gaussian mixture model cannot deal with the problems arising from light changes, because the background quality obtained by GMM often depends on the prehistory. We operate an inter-frame action based on the GMM result. It improves the sensitivity of the GMM to changes in light and improves the quality of the background model as a feedback variable.

In order to evaluate the improvement degree of our approach, a classical data set CDnet2014 [79] was used to test these three approaches, including the Gaussian mixture model (GMM), the interframe difference method and our approach. This data set contains 11 video categories (more than 170, 000 frames totally) with 4 to 6 videos sequences in each category. The CDnet2014 dataset provides realistic, camera-captured, diverse sets of indoor and outdoor videos. Spatial resolutions of the videos in the CDnet2014 vary from 320×240 to 720×486 . This data set also has an official test tool that specifically tests the effectiveness of different methods. However, the test tool only tests the moving parts rather than the background to evaluate the results of background reconstruction. We use the background reconstructed by different methods for the evaluation. Background reconstruction tasks are usually prepared for moving target detection. Now, instead of eliminating the moving parts of the image, as done in Figure 5.6, we focused on the moving objects. The results regarding the identification of the moving parts (the foreground) are shown in Figure 5.7.

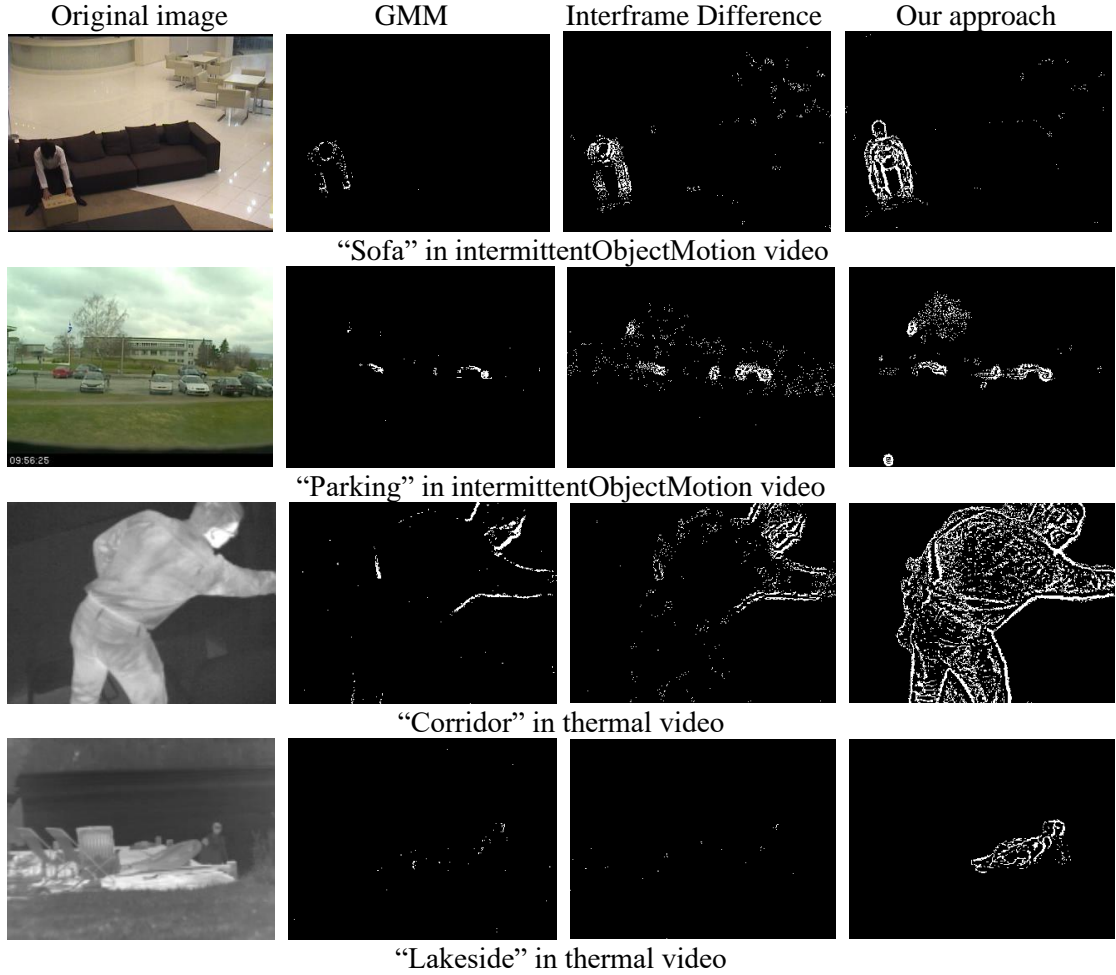


Fig. 5.7 Comparison for benchmark videos between our approach and other approaches. From left to right for each scene we present: the original image, and the results for the foreground (the moving part) obtained with the Gaussian Mixture Model (GMM), the Interframe Difference Model and our new approach [II].

Clearly, a better image comprehension is obtained by applying our method. We used the evaluation tools of the database, and the indices Recall, Precision, PWC, and F-measure were chosen. Recall, Precision, and F-measure can be calculated from Eqs (4.5 - 4.7). The calculation of PWC is shown below:

$$PWC = 100 * \frac{FN + FP}{TP + FN + FP + TN} \quad 5.14$$

Here TP, TN, FP and FN denote the number of true positives, the number of true negatives, the number of false positives and the number of false negatives regarding the pixel identification. The average results are shown in the form of a line chart in Figure 5.8.

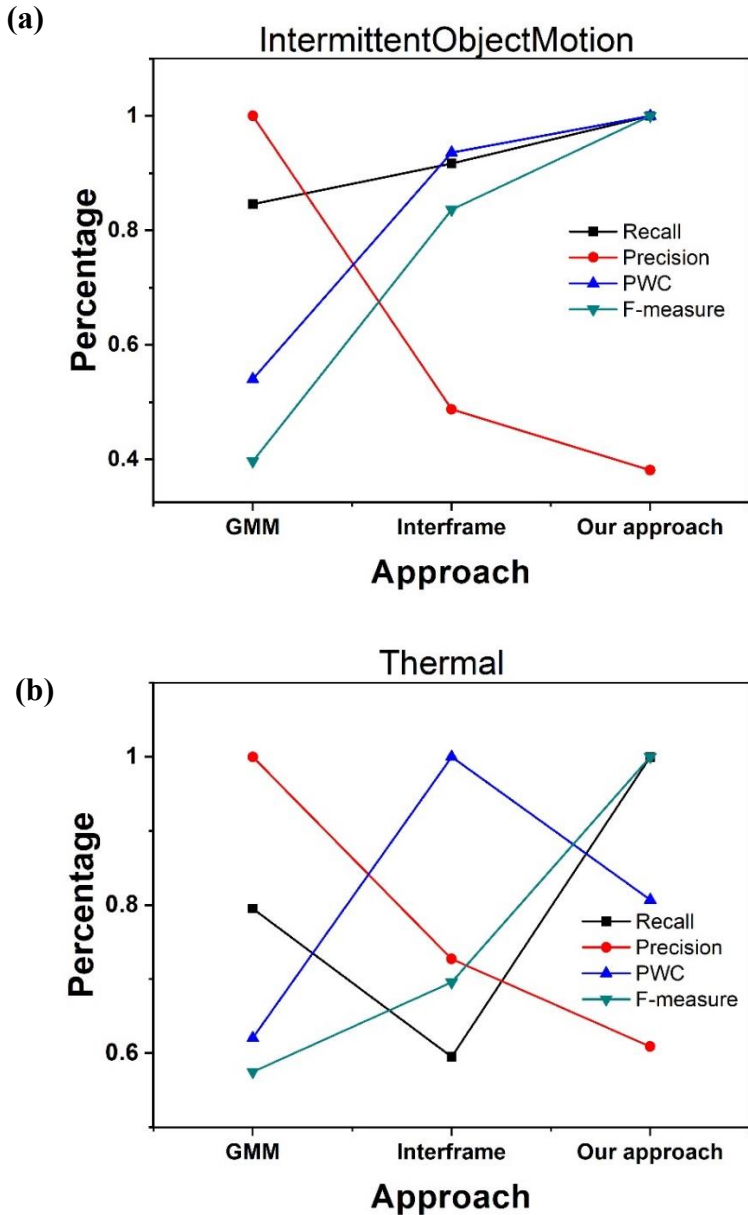


Figure 5.8 Comparison of evaluation indices of various approaches [II].

From Figure 5.8 (a) we can see, that the Recall, PWC and F-measure values for our approach are better than those from the other two approaches when the IntermittentObjectMotion videos categories are used. Although the PWC index of our approach is not the best in the Thermal video categories case, the Recall and F-measure values are still good. The Precision indices of our approach are the worst in both cases, which is caused by the sensitivity to light change. Our approach increases the ability to detect slow-moving objects, but at the same time loses the ability to resist light variation.

Chapter 6 Conclusion and outlook

All the projects of this thesis deal with the research areas in photobiology. The common theme in these projects is optical scattering with a focus on the utilization of the positive effects and reduction of the negative effects.

In the medical field, we show the application scenarios and feasibility of the GASMAS technique in medical diagnostics. We profit from the scattering, making the pathlength through gas longer and thus making the absorption imprint more prominent. We studied the effect of decongestants on the oxygen content of the frontal sinus in volunteers with rhinitis and being fully healthy. By observing the effect of nitrogen flow in conjunction with decongestants, we for the first time objectively demonstrated how valuable the GASMAS technique might be as a diagnostic tool, monitoring the compete system of sinus ventilation. For the volunteer with rhinitis, we found in Figure 3.6 (b) that the oxygen content increases after spraying the decongestant, which means that the gas exchange becomes stronger as the channel is opened. On the contrary, there is not any significant influence after spraying the decongestant in the healthy case. The next planned is to correlate the gas signal with the types of bacteria found in patients with sinusitis in order to investigate the potential of the GASMAS technique in the diagnosis of sinusitis. A major breakthrough would be to discriminate between bacterial and viral infections, thus contributing in the fight against the development of antibiotic resistance but this is still to be proven.

As a start of the project to take small-scale GASMAS to adult lung function monitoring, we used polystyrene foam and some biological tissue to perform large-scale, exploratory GASMAS experiments. The results show that for large samples such as foam, there is a clear pattern of gas absorption. However, when the percentage of the absorbed light is less than 1% of the detectable light, the performance of pulsed system will be low. This relates to laser pulse fluctuations and triggering errors. In the future, we will use solid-state tapered amplifiers to improve the output of the laser and eliminate the negative influence of the measurement due to the output intensity fluctuations of the laser. We believe that such a large-scale GASMAS system in the future could greatly

benefit patients with lung deficiency and/or influenced by SARS-CoV-2.

In the mosquito monitoring projects, two types of systems were introduced based on two different optical sensors. The first system is a combination of two counting systems, including a light shading system and a scattering system. By analyzing the sequence of mosquito signals and combining the outputs of these two systems, the monitoring capabilities of the composite system can be improved. In future work, the system we developed could be part of a network for monitoring mosquitoes, and achieve wireless data transmission and cloud storage. The image recording and processing for mosquitoes is a new attempt. Although our images are not very sharp, the F-measure value of 93% is achieved in the classification between mosquitoes and bees. The future goals are to get image samples with high quality and employ even more efficient classification methods.

Inverse lock-in-like spatial modulation (ILLSPAM) is a new approach described in the thesis to deal with the signal of interest. Several examples of visual impairment that may occur in life are discussed and illustrated. A simple set-up that simulated how the human brains work was demonstrated in the laboratory. A new processing method based on the Gaussian mixture model (GMM) and the interframe difference method was introduced. The proposed method has shown certain advantages, but still has shortcomings regarding the ability to be immune to changes in light. In the future, more professional devices will be adopted to simulate the process of human brain processing. At the same time, further processing methods (such as machine learning, deep learning, etc.) will be applied in image processing.

References

- [1] K. Smith, *The Science of Photobiology*, Springer, New York (1989).
- [2] M. Sjöholm, G. Somesfalean, J. Alnis, S. Andersson-Engels, and S. Svanberg, Analysis of gas dispersed in scattering media, *Optical Letters*, **26**, 16-18 (2001).
- [3] S. Svanberg, Gas in scattering media absorption spectroscopy – from basic studies to biomedical applications, *Laser & Photonics Reviews*, **7**, 779-796 (2013).
- [4] J. Huang, H. Zhang, T.Q. Li, G.Y. Zhao, S. Svanberg and K. Svanberg, Studies of oxygen and oxygen exchange in fruits using gas in scattering media absorption spectroscopy, Progress in Electromagnetics Research Symposium Proceedings, Guangzhou, 1251-1255 (2014).
- [5] H. Zhang, H.Y. Lin, T.Q. Li, Z. Duan, K. Svanberg and S. Svanberg, Non-invasive optical detection of oxygen content in food packages using gas in scattering media absorption spectroscopy, *Acta Optica Sinica*, **36**, 0230005-1 (2015).
- [6] W.S. Li, H.Y. Lin, H. Zhang, K. Svanberg and S. Svanberg, Detection of free oxygen and water vapor in fertilized and unfertilized eggs by diode laser spectroscopy – exploration of diagnostics possibilities, *Journal of Biophotonics*, **11** (2017).
- [7] H. Zhang, J. Huang, T. Li, S. Svanberg, K. Svanberg, Optical detection of middle ear infection using spectroscopic techniques: phantom experiments, *Journal of Biomedical Optics*, **20** (5), 57001 (2015).
- [8] P. Chen, W.S. Li, H.Y. Lin, D.L. Chen, Y. Li, K. Svanberg, and S. Svanberg, Assessment of free gas in the tibial condyle bone of the human knee by diode laser spectroscopy with possible application to arthrosis diagnostics, *IEEE Journal of Selected Topics in Quantum Electronics*, **25**, 1-4 (2018).
- [9] D.L. Chen, W.S. Li, W. He, H. Zhang, Q.W. Zhang, H.Y. Lin, S. Svanberg, K. Svanberg, and P. Chen, Laser-based gas absorption spectroscopy in decaying hip bone: water vapor as a predictor of osteonecrosis, *Journal of Biomedical Optics*, **24** (6), 065001 (2019).
- [10] L. Persson, K. Svanberg and S. Svanberg, On the potential of human sinus cavity

- diagnostics using diode laser gas spectroscopy, *Applied Physics B*, **82**, 313–317 (2006).
- [11] L. Persson, M. Andersson, M. Cassel-Engquist, K. Svanberg and S. Svanberg, Gas monitoring in human sinuses using tunable diode laser spectroscopy, *Journal of Biomedical Optic*, **12** (5):054001 (2007).
- [12] M.D. C. L. Scott, *Mayo Clinic Family Health Book*, Fifth Edition, Mayo Clinic (2018).
- [13] B. Wyler and W.K. Mallon, Sinusitis update, *Emergency Medicine Clinics of North America*, **37**(1):41-54 (2019).
- [14] B.K. English and A.H. Gaur, The use and abuse of antibiotics and the development of antibiotic resistance. *Advances in Experimental Medicine and Biology*, **659**, 73-82 (2010).
- [15] A. Kumar and B.V. Bhat, Epidemiology of respiratory distress of newborns, *Indian Journal of Pediatrics*, **63** (1), 93-8 (1996).
- [16] P. Lundin, E.K. Svanberg, L.Coccola, M. Lewander Xu, G. Somesfalean, S. Andersson-Engels, J. Jahr, V. Fellman, K. Svanberg and S. Svanberg, Non-invasive monitoring of gas in the lungs and intestines of newborn infants using diode lasers: feasibility study, *Journal of Biomedical Optics*, **18** (12), 127005 (2013).
- [17] E.K. Svanberg, P. Lundin, M. Larsson, J. Åkesson, K. Svanberg, S. Svanberg, S. Andersson-Engels and V. Fellman, Non-invasive monitoring of oxygen in the lungs of newborn infants by diode laser spectroscopy, *Biomedical Optics*, 25-28 (2016).
- [18] E.K. Svanberg and S. Svanberg, Equipment and method for internal laser illumination for medical gas analysis, Swedish Patent Application No 1500335-3. (2015).
- [19] <https://www.who.int/data/gho/whs-2020-visual-summary>.
- [20] World malaria report 2020: 20 years of global progress and challenges. Geneva: World Health Organization; 2020. Licence: CC BY-NC-SA 3.0 IGO.
- [21] H. Caraballo and K. King, Emergency department management of mosquito-borne illness: malaria, dengue, and West Nile virus. *Emergency Medicine Practice*, **16**

(5):1-23 (2014).

[22]<https://www.cdc.gov/niosh/topics/outdoor/mosquito-borne/default.html>.

[23]I.R. Richards, Photoelectric cell observations of insects in flight, *Nature*, **175**, 128-129 (1955).

[24]A. Gebru, S. Jansson, R. Ignell, C. Kirkeby, J. C. Prangsma and M. Brydegaard, Multiband modulation spectroscopy for the determination of sex and species of mosquitoes in flight, *Journal of Biophotonics*, **11** (8), 1-13 (2018).

[25]S. Jansson, P. Atkinson, R. Ignell and M. Brydegaard, First polarimetric investigation of malaria mosquitoes as lidar targets, *IEEE Journal of Selected Topics in Quantum Electronics*, **25**(1), 1-8 (2019).

[26]I. Potamitis and I. Rigakis, Novel noise-robust optoacoustic sensors to identify insects through wingbeats, *IEEE Sensors Journal*, **15** (8), 4621-4631 (2015).

[27]E. Fanioudakis, M. Geismar and I. Potamitis, Mosquito wingbeat analysis and classification using deep learning, 2018 26th European Signal Processing Conference (EUSIPCO), Rome, Italy, 2410-2414 (2018).

[28]A. M. M. De Los Reyes, A. C. A. Reyes, J. L. Torres, D. A. Padilla and J. Villaverde, Detection of *Aedes Aegypti* mosquito by digital image processing techniques and support vector machine, 2016 IEEE Region 10 Conference (TENCON), Singapore, 2342-2345 (2016).

[29]M. Minakshi, P. Bharti and S. Chellappan, Leveraging smart-phone cameras and image processing techniques to classify mosquito species. Proceedings of the 15th EAI International Conference on Mobile and Ubiquitous Systems: Computing, Networking and Services (2018).

[30]Y. Zhong, J. Gao, Q. Lei and Y. Zhou, A Vision-based counting and recognition system for flying insects in intelligent agriculture. *Sensors*, **18**, 1489 (2018).

[31]A.B. Watson, *Digital Images and Human Vision*; Bradford Books, MIT Press: Cambridge, MA, USA (1993).

[32]Z.P. Li, *Understanding Vision, Theory, Models and Data*, Oxford University Press: Oxford, UK (2014).

- [33]R. Szeliski, *Computer Vision-Algorithms and Applications*, Springer: Berlin/Heidelberg, Germany, 531 (2010).
- [34]K. Toyama, J. Krumm, B. Brumitt and B.Meyers, Wallflower: Principles and practice of background maintenance, In Proceedings of the Seventh International Conference on Computer Vision (ICCV'99), Kerkyra, Greece, 255–261 (1999).
- [35]S.-H. Hong, J.-S. Jang and B. Javidi, Three-dimensional volumetric object reconstruction using computational integral imaging. *Optical Express*, **12**, 483–491 (2004).
- [36]X. Xiao and B. Javidi, M. Martinez-Corral and A. Stern, Advances in three-dimensional integral imaging: Sensing, display, and applications, *Applied Optics*, **52**, 546–560 (2013).
- [37]A.J. Lipton, H. Fujiyoshi and R.S. Patil, Moving target classification and tracking from real-time video, In Proceedings of the Fourth IEEE Workshop on Applications of Computer Vision, Princeton, NJ, USA, 8–14 (1998).
- [38]C. Stauer and W.E.L.Grimson, Adaptive background mixture models for real-time tracking. In Proceedings of the Computer Vision and Pattern Recognition Conference, Fort Collins, CO, USA, 246–252 (1999).
- [39]N. Goyette, P. Jodoin, F. Porikli, J. Konrad and P. Ishwar, Changelogdetection.net: A new change detection benchmark dataset. In Proceedings of the Computer Vision and Pattern Recognition Conference, Providence, RI, USA, 1–8 (2012).
- [40]H. Quek and K. W. Leong, Near-infrared fluorescent nanoprobes for in vivo optical imaging, *Nanomaterials* **2** (4), 92-112 (2012).
- [41]I.E. Gordon, L.S. Rothman, C. Hill, R.V. Kochanov, Y. Tan, P.F. Bernath, M. Birk, V. Boudon, A. Campargue, K.V. Chance, B.J. Drouin, J.-M. Flaud, R.R. Gamache, J.T. Hodges, D. Jacquemart, V.I. Perevalov, A. Perrin, K.P. Shine, M.-A.H. Smith, J. Tennyson, G.C. Toon, H. Tran, V.G. Tyuterev, A. Barbe, A.G. Császár, V.M. Devi, T. Furtenbacher, J.J. Harrison, J.-M. Hartmann, A. Jolly, T.J. Johnson, T. Karman, I. Kleiner, A.A. Kyuberis, J. Loos, O.M. Lyulin, S.T. Massie, S.N. Mikhailenko, N. Moazzen-Ahmadi, H.S.P. Müller, O.V. Naumenko, A.V. Nikitin, O.L. Polyansky,

- M. Rey, M. Rotger, S.W. Sharpe, K. Sung, E. Starikova, S.A. Tashkun, J. Vander Auwera, G. Wagner, J. Wilzewski, P. Weisło, S. Yu and E.J. Zak, The HITRAN2016 molecular spectroscopic database, *Journal of Quantitative Spectroscopy and Radiative Transfer*, **203**, 3-69 (2017).
- [42] R.V. Kochanov, I.E. Gordon, L.S. Rothman, P. Weisło, C. Hill and J.S. Wilzewski, HITRAN Application Programming Interface (HAPI): A comprehensive approach to working with spectroscopic data, *Journal of Quantitative Spectroscopy and Radiative Transfer*, **177**, 15-30 (2016)
- [43] https://en.wikipedia.org/wiki/Scattering#cite_note-14.
- [44] <http://hyperphysics.phy-astr.gsu.edu/hbase/atmos/blusky.html>.
- [45] D.J. Gardiner, *Practical Raman spectroscopy*, Springer-Verlag, ISBN 978-0-387-50254-0 (1989).
- [46] P. Bouguer, Essai d'optique sur la gradation de la lumière. *Nature*, **111**, 320 (1923).
- [47] J.H. Lambert, Photometria sive de mensura et gradibus luminis, colorum et umbrae, Augustae Vindelicorum, E. Klett (C.P. Detleffsen) (1760).
- [48] A. Beer, Determination of the absorption of red light in colored liquids, *Annalen der Physik und Chemie*, **162** (5), 78–88 (1852) (in German).
- [49] <https://nanoplus.com/en/technology/tdlas/>.
- [50] S. Svanberg, Gas in scattering media absorption spectroscopy – from basic studies to biomedical applications, *Laser and Photonics Reviews*, **7**, 779-796(2013).
- [51] <https://acaai.org/allergies/types/sinus-infection>.
- [52] <https://www.merckmanuals.com/home/ear,-nose,-and-throat-disorders/nose-and-sinus-disorders/sinusitis>.
- [53] https://en.wikipedia.org/wiki/Aedes_albopictus.
- [54] P. Hochedez, S. Jaureguierry, M. Debruyne, P. Bossi, P. Hausfater, G. Brucker, F. Bricaire and E. Caumes, Chikungunya infection in travelers. *Emerging Infectious Diseases*, **12**, 1565-1567 (2006).
- [55] A. Farajollahi, D.M. Fonseca, L.D. Kramer and K. A. Marm, "Bird biting" mosquitoes and human disease: a review of the role of *Culex pipiens* complex

mosquitoes in epidemiology, *Infection Genetics Evolution, Journal of Molecular Epidemiology and Evolutionary Genetics of Infectious Diseases*, **11**, 1577-1585 (2011).

[56]https://en.wikipedia.org/wiki/Aedes_albopictus#cite_note-Hochedez-2.

[57]https://en.wikipedia.org/wiki/Culex_pipiens#cite_note-2-3.

[58]A. Gebru, S. Jansson, R. Ignell, C. Kirkeby, J.C. Prangsma and M. Brydegaard, Multiband modulation spectroscopy for the determination of sex and species of mosquitoes in flight. *Journal of Biophotonics*, **11**, 2018000 (2018).

[59]S.M. Zhu, E. Malmqvist, W.S. Li, S. Jansson, Y.Y. Li, Z. Duan, K. Svanberg, H.Q. Feng, Z.W. Song, G.Y. Zhao, M. Brydegaard, and S. Svanberg, Insect abundance over Chinese rice fields in relation to environmental parameters, studied with a polarization-sensitive CW near-IR Lidar system, *Applied Physics B*, **123**, 211 (2017).

[60]Z.W. Song, B.X. Zhang, H.Q. Feng, S.M. Zhu, L.N. Hu, M. Brydegaard, Y.Y. Li, S. Jansson, E. Malmqvist, K. Svanberg, G.Y. Zhao, J. Bood, S. Svanberg, and D.S. Li, Application of Lidar remote sensing of insects in agricultural entomology on the Chinese scene, *Journal of Applied Entomology*, **144**, 161 (2020).

[61]S. Dasiopoulou, V. Mezaris, I. Kompatsiaris, V. Papastathis and M.G. Strintzis, Knowledge-assisted semantic video object detection, in IEEE Transactions on Circuits and Systems for Video Technology, **15**, 1210-1224 (2005).

[62]D. G. Lowe, Object recognition from local scale-invariant features, Proceedings of the Seventh IEEE International Conference on Computer Vision, Kerkyra, Greece, **2**, 1150-1157(1999).

[63]N. Dalal and B. Triggs, Histograms of oriented gradients for human detection, IEEE Computer Society Conference on Computer Vision and Pattern Recognition (CVPR), **1**, 886-893 (2005).

[64]T. Sergios and K. Koutroumbas, *Pattern Recognition*, 4th ed, Chapter 8 - Template Matching, 481-519 (2009).

[65]J.P. Lewis, Fast template matching, Canadian Image Processing and Pattern

- Recognition Society, Vis. Interface. **95**, 120-123 (1994).
- [66] H. Schweitzer, J.W. Bell and F. Wu, Very fast template matching. In: A. Heyden, G. Sparr, M. Nielsen, P. Johansen (eds) Computer Vision — European Conference on Computer Vision (ECCV), **2353**, 358-372 (2002).
- [67] Svanberg, S. Laser spectroscopy in medical diagnostics, in *Lasers for Medical Applications* (ed. H. JelinKova), Woodhead Publication, (2013), p.307.
- [68] Y. Sasaki, The truth of the F-measure. Teach Tutor Mater (2007).
- [69] J. Wagemans, J.H. Elder, M. Kubovy, S.E. Palmer, M.A. Peterson, M. Singh and R. von der Heydt, A century of Gestalt psychology in visual perception: I. Perceptual grouping and figure-ground organization, *Psychol. Bull.*, **138**, 1172–1217 (2012).
- [70] J. Wagemans, J. Feldman, S. Gepshtein, R. Kimchi, J.R. Pomerantz, P.A. van der Helm and C. van Leeuwen, A century of Gestalt psychology in visual perception: II. Conceptual and theoretical foundations, *Psychological Bulletin*, **138**, 1218–1252 (2012).
- [71] R. Szeliski, *Computer Vision - Algorithms and Applications*; Springer: Berlin/Heidelberg, Germany, 531 (2010).
- [72] K. Toyama, J. Krumm, B. Brumitt and B.W. Meyers, Principles and practice of background maintenance. In Proceedings of the Seventh International Conference on Computer Vision (ICCV'99), Kerkyra, Greece, 255–261 (1999).
- [73] S.-H. Hong, J.-S.Jang and B. Javidi, Three-dimensional volumetric object reconstruction using computational integral imaging. *Optical Express*, **12**, 483–491 (2004).
- [74] X. Xiao, B. Javidi, M. Martinez-Corral and A. Stern, Advances in three-dimensional integral imaging: Sensing, display, and applications. *Applied Optics*, **52**, 546–560 (2013).
- [75] A.J. Lipton, H. Fujiyoshi and R.S. Patil, Moving target classification and tracking from real-time video. In Proceedings of the Fourth IEEE Workshop on Applications of Computer Vision, Princeton, NJ, USA, 8–14 (1998).

- [76]C. Stauffer and W.E.L. Grimson, Adaptive background mixture models for real-time tracking. In Proceedings of the Computer Vision and Pattern Recognition Conference, Fort Collins, CO, USA, 246–252 (1999).
- [77]C. Stauffer and W.E.L. Grimson, Adaptive background mixture models for real-time tracking. In Proceedings of the Computer Vision and Pattern Recognition Conference, Fort Collins, CO, USA, 246–252 (1999).
- [78]A.J. Lipton, H. Fujiyoshi and R.S. Patil, Moving target classification and tracking from real-time video, In Proceedings of the Fourth IEEE Workshop on Applications of Computer Vision, Princeton, NJ, USA, **19**, 8–14 (October).
- [79]Y. Wang, P.-M. Jodoin, F. Porikli, J. Konrad, Y. Beniezeth, and P. Ishwar, CDnet 2014: An Expanded Change Detection Benchmark Dataset, in Proc. IEEE Workshop on Change Detection (CDW-2014) at CVPR-2014, 387-394(2014).

Acknowledgements

It is my third year of the three-year master project and the seventh year as a student of the South China Normal University. I am very grateful for the cultivation and education from SCNU for me during these seven years. I grew from an ignorant high school graduate to a master student, who now reasonably well can be on my own. In the past seven years, I have met many outstanding people, including teachers and colleagues, who gave me plenty of support and help.

There are two people to whom I would like to express my appreciation most and they are my supervisors, Prof. Katarina Svanberg and Prof. Sune Svanberg. I am very honored to be in their group, the SCNU Applied Laser Spectroscopy and Remote Sensing Group. Both of them take scientific research very seriously, cautiously and responsibly. When I first joined the group, they taught me the basic knowledge and experimental principles with huge patience. Their rigorous and serious treatment of science and their perseverance in dealing with difficulties has had a great impact on me. Not only academically; they also gave me a lot of help in life, especially at the time when I studied at the Lund University, Sweden, as an exchange student. The optimistic attitude towards life and the energetic spirit from Prof. Sune Svanberg deeply impress and inspire me in my life. Prof. Katarina Svanberg often treats me from an adult perspective, not just a student. She often teaches me to be responsible for myself and encourage me to overcome the fear in my heart. They will always be happy to help me as long as I need. Under their influence, I now often take the initiative to help people around me who have to go through difficulties. I am honored to have had the opportunity to go to Lund University as an exchange student. The knowledge and experience I learned at Lund University will affect me for life. I miss very much the weekend I spent together with part of the Svanberg family on the island of Klädesholmen. It is the best memory of my entire exchange life.

Then, I would like to thank other members in the group. Thanks to Jinlei Wang, for teaching me basic knowledges and giving me a lot of help in the mosquito project. He helped me get a good start in my master student life. Thanks to Lingna Hu, who

transferred to me the principle of the GASMAS technique and gave me plenty of advices when I needed. Thanks to Zheng Duan, for always helping without any return. As a senior member in the group, he is a guy who always is prepared to help others in need. Thanks to Xun Wang and Ying Li, for bring me a lot of fun in work and life. Thanks to Han Zhang, who is also very willing to help people. She gave me plenty of advice and help when I was in trouble. Thanks to Guangyu Zhao, Ye Yuan, Junchen Lu and Xiaobo Lin, for support in the project cooperation. Thanks to other members in the group, for letting me have a great time with them. I am also very grateful to the collaborators in Lund Sweden: Patrik Lundin, Anna-Lena Sahlberg and Emilie Krite Svanberg.

Finally, I would like to thank my parents and my elder brother for their unfailing support and meticulous care during these years. Nothing would have happened without their love.

This work was supported by the Science and Technology Program of Guangzhou (2019050001), and the Guangdong Provincial Key Laboratory of Optical Information Materials and Technology (2017B030301007).

Publications

- [I] J.L. Wang, S.M. Zhu, **Y.Y. Lin**, S. Svanberg and G.Y. Zhao, Mosquito counting system based on optical sensing. *Applied Physics B*, **126**, 1-10 (2020).
- [II] **Y.Y. Lin** and S. Svanberg, Foreground scattering elimination by inverse lock-in-like spatial modulation. *Vision*, **4**, 37 (2020).
- [III] **Y.Y. Lin**, P. Lundin, E. Krite Svanberg, K. Svanberg, S. Svanberg and A.-L. Sahlberg, Gas in scattering media absorption spectroscopy on small and large Scales - towards the extension of lung spectroscopic monitoring to adults, Submitted (2021).
- [IV] H. Zhang, N. Han, **Y.Y. Lin**, J.W. Huang, S. Svanberg and K. Svanberg, Gas monitoring in human frontal sinuses - stability considerations and gas exchange studies, Submitted (2021).
- [V] Y.T. Sun, **Y.Y. Lin**, G.Y. Zhao and S. Svanberg, Identification of flying insects in the spatial, spectral and time domains with focus on mosquito imaging, Submitted (2021) (Joint first authorship).

Patent application

- [VI] **Y.Y. Lin** and S. Svanberg, A foreground scattering elimination method based on inverse phase-locked spatial modulation, Chinese patent application, 201910546779.X, 2019.



Mosquito counting system based on optical sensing

Jinlei Wang¹ · Shiming Zhu¹ · Yueyu Lin¹ · Sune Svanberg^{1,2} · Guangyu Zhao¹

Received: 11 May 2019 / Accepted: 29 November 2019

© The Author(s) 2020

Abstract

Mosquitos, sometimes carrying deadly diseases such as malaria, zika, and dengue fever, cause much concern. To control mosquitos, it is important to effectively monitor their presence and behavioral trends. We have constructed two optical sensing systems for insects based on light attenuation and light backscattering, respectively. The systems, which were tested with the potentially dangerous *Aedes albopictus* and *Culex pipiens*, were able to extract the wing-beat frequency, when they passed impinging light, derived from light-emitting diodes. We could achieve distinction between the sexes of *A. albopictus* and *C. pipiens* based on the wing-beat frequency. Finally, we propose a statistical method suitable for the system to improve the accuracy of counting.

1 Introduction

Mosquitoes are the most dangerous animals in the world. It is well known that about 200 million people will be infected with malaria every year and kill at least 500,000 people following bites from female *Anopheles* mosquitoes [1–3]. These amazing numbers are increasingly catching worldwide attention. Pesticides are used as counter-measures and anti-malarial drugs are formulated. However, with the mosquitoes developing resistance to pesticides as well as to drugs, the situation becomes aggravated. In addition to malaria, mosquitoes carry about 100 other diseases, such as dengue fever [4, 5], zika, and yellow fever [6]. According to statistics, about 800,000 people are annually killed by mosquito-borne diseases. Therefore, effective monitoring of the type and distribution of mosquitoes is very important to reduce the harm caused by these dangerous disease vectors.

People are often interrupted by mosquito interference, at work and at rest, and can, with sufficient attention accurately,

identify the number and type of mosquitoes through vision and hearing. The eye acquires the structural characteristics of the mosquito, while the ear recognizes the sound of the wing beats. In the same way, insects can be captured by cameras and microphones. Electronic recordings are inspired by human recognition, as employed in the following two approaches:

1.1 Image tracking

Images of insects are recorded at different angles by a camera followed by identification based on the characteristics features [7–9]. This method not only requires a high acquisition speed of the camera to quickly acquire insect images in flight, but also requires sufficient contrast of the background [10, 11]. Using infrared radiation in the recordings, the insects are thought to be less affected by the detection procedure [12, 13]. The image tracking method can achieve high accuracy by observing mosquito flight details. However, this method is not suitable for a wide range of monitoring, and also obtains a large number of useless images which increases the difficulty of analysis.

1.2 Acoustic tracking

When insects flap their wings, sound with a special frequency is produced, and the pitch of the sound is related to the type of insect [14]. Using a microphone to monitor insects provides a simple and less costly method than image tracking [11]. However, it is difficult to use the microphone

✉ Sune Svanberg
sune.svanberg@fysik.lth.se

Guangyu Zhao
guangyu.zhao@coer-scnu.org

¹ Center for Optical and Electromagnetic Research, South China Academy of Advanced Optoelectronics, South China Normal University, University City Campus, Guangzhou 510006, China

² Department of Physics, Lund University, SE 221 00 Lund, Sweden

efficiently due to environmental influences and because of the limited range of sound propagation [15].

Recently, new approaches based on optics have also emerged. Brydegaard et al. developed CW lidar techniques to monitor insects based on light scattering with fast read-out capability to ensure the capturing of wing beats [16–21]. Potamitis et al. used photoacoustic as well as optical sensors to monitor insects [22–26].

In the present paper, we propose a method of combining optical counting with mosquito trap techniques to increase the probability of insect encounters. Two optical counting systems, based of optical shadowing and light backscattering, respectively, were constructed and used to increase the accuracy of mosquito counting. Our method has a low cost (in the order of 50 EURO, excluding the optional commercial amplifier, the commercial trap, and the computer with its data acquisition card) and could be expected to be useful in a wide range of mosquito surveillance.

2 System descriptions

We use two optical methods (shading and scattering) to count and identify mosquitoes.

2.1 Scattering counting system

We fixed four LEDs (CH-HQ-1W, Chenhui Optoelectronic Factory Outlet Store, China), each emitting 1 W at a center wavelength of 940 nm at the focus of a Fresnel lens group (MYlens-d55, focal length 25 mm, Shenzhen Meiyang Technology Co., China), as shown in Fig. 1. A beam having a certain divergence angle is emitted from the LED array, and the Fresnel lenses collimates the light to form a uniform detection area. To avoid the influence of the external light and the stray light from the LEDs, we installed the detecting photodiode (BP104F, OSRAM Opto Semiconductors) centered in the collection channel and looking vertically downwards into the system dark interior, towards a suction fan. A 940 nm band-pass filter

($\phi 8 \times 0.7$ mm, Shenzhen Infrared Laser Technology Co., China) is mounted in front of the photodiode to suppress daylight. When an insect passes the light beam, an oscillatory scattering light signal is received by the photodiode. The photocurrent generated is then boosted by an amplifier. We made some changes to a commercial amplifier (C7319, Hamamatsu Optoelectronics, Japan), to increase the multiplication factor of the original amplifier by five times, reaching 5×10^7 .

2.2 Shading counting system

In the other geometry adapted, the shadow caused by the insect when passing the emitted light is instead utilized, and the signal from the detector is then transiently reduced. Our set-up is shown in Fig. 2. We placed four LEDs (L-34F3C, Kingbright Electronic Co, Ltd., China) and four photodiodes (BP 104F, OSRAM Opto Semiconductors) at the foci of the Fresnel lens groups, as shown in Fig. 2b). The LEDs emit a beam of light through the first Fresnel lenses (focal length 25 mm); the light passes with parallel beams through the detection area, and is then focused on the photodiodes by the second set of Fresnel lenses (focal length 25 mm). When compared with the previous system, the peak wavelength of the LEDs is still 940 nm, but the shading counting system uses a much lower LED power of 80 mW. When the mosquito passes through the collimated detection area, the photocurrent of the photodiode changes accordingly due to the shading of the light. The varying photocurrent is amplified by the circuit shown in Fig. 3. The photodiode receives the maximum photocurrent signal when no object passes through the detection area. Since the light intensity then remains the same, the photocurrent passing through the AC-coupled amplifier is zero. When a flying object passes through the detection volume, the intensity of the light received by the photodiode is modulated, resulting in an oscillating photocurrent, which is amplified.

Fig. 1 Counting system based on light scattering. **a** Photograph of the experimental arrangement of the scattering counting system. The inside of the system is covered with black, diffusing material to reduce stray light. **b** A cross-sectional view of the scattering counting system. The installed photodiode and band-pass filter are shown separately

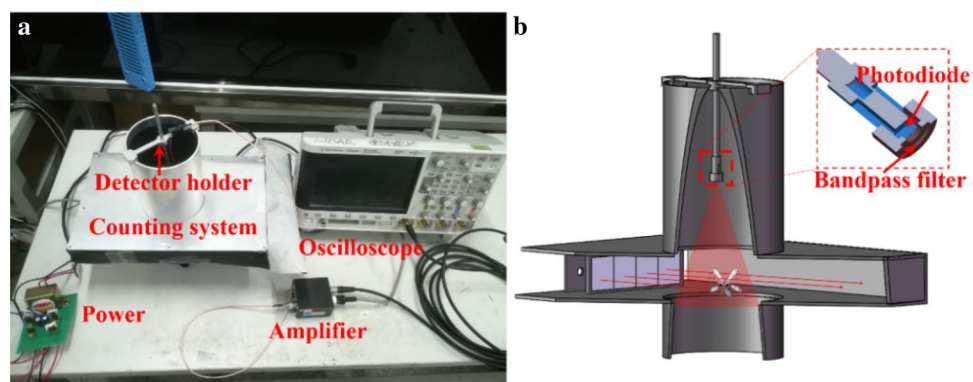


Fig. 2 **a** Photo of the experimental arrangement of the shadowing counting system. **b** Detailed display of the four infrared LEDs ①, the four photodiodes ③, and the two Fresnel lens groups ②

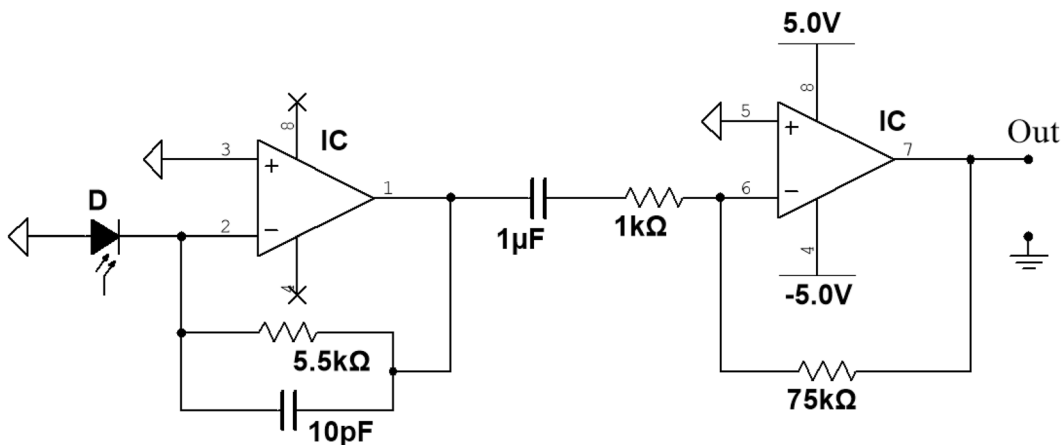
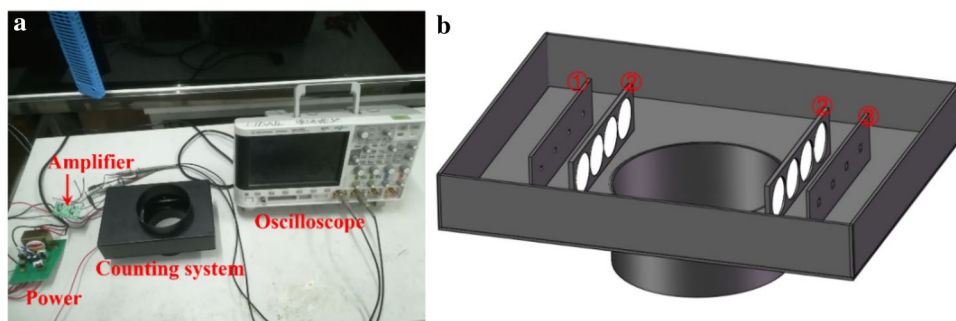


Fig. 3 AC amplifier circuit for the shadowing counting system

3 Measurements and results

3.1 System testing

We used *Aedes albopictus* and *Culex pipiens* insects to test the two counting systems, first separately, then in a tandem arrangement. The first type of mosquito can, when infected, carry dengue and zika virus, while the second one can cause Japanese encephalitis. A signal of a passing mosquito, as recorded by the scattering counting system is shown in Fig. 4. Because of a substantial level of background light, as scattered from the system interior also in the absence of a passing mosquito, a steady-state signal level of about 2 V is generated, actually with a weak 50 Hz signal superimposed due to insufficient shielding of the power supply. A passing mosquito gives rise to a signal increase of about 0.1 V. Figure 4b shows an expanded part of the signal of interest caused by an *A. albopictus*. The oscillating signal from the beating wings is seen superimposed on the much slower increase in scattering caused by the passing insect body. The transformation from the time domain to the frequency domain of the wing-beat signal is shown in Fig. 4c featuring a fundamental wing-beat

frequency of about 800 Hz and also several harmonics, reflecting the fact that the signal is far from a pure sinus wave.

In a test of the shadowing counting system, we restricted the recording to the two middle photodiodes. The outputs of the photodiodes were directly connected to two channels of an oscilloscope after boosting with amplifiers, as shown in Fig. 3. The signals are shown in Fig. 5. Both photodiodes monitored the wing-beat signal of the *Aedes albopictus*, with a time separation between the two signals. We performed a transformation to the frequency domain of the two signals, as shown in Fig. 5b, c. The signals have the same wing-beat frequency. It seems that the insect has chosen a trajectory which sequentially passes through the detection volumes of both photodiodes.

3.2 Species and sex distinction

To further improve the performance of the technique, also for allowing possible distinction between species and sexes, the two counting systems and a commercial mosquito trap (Biogents, Regensburg, Germany) are connected in series, as shown in Fig. 6. Such a combined system has advantages in the operation, since it does not only improve the accuracy

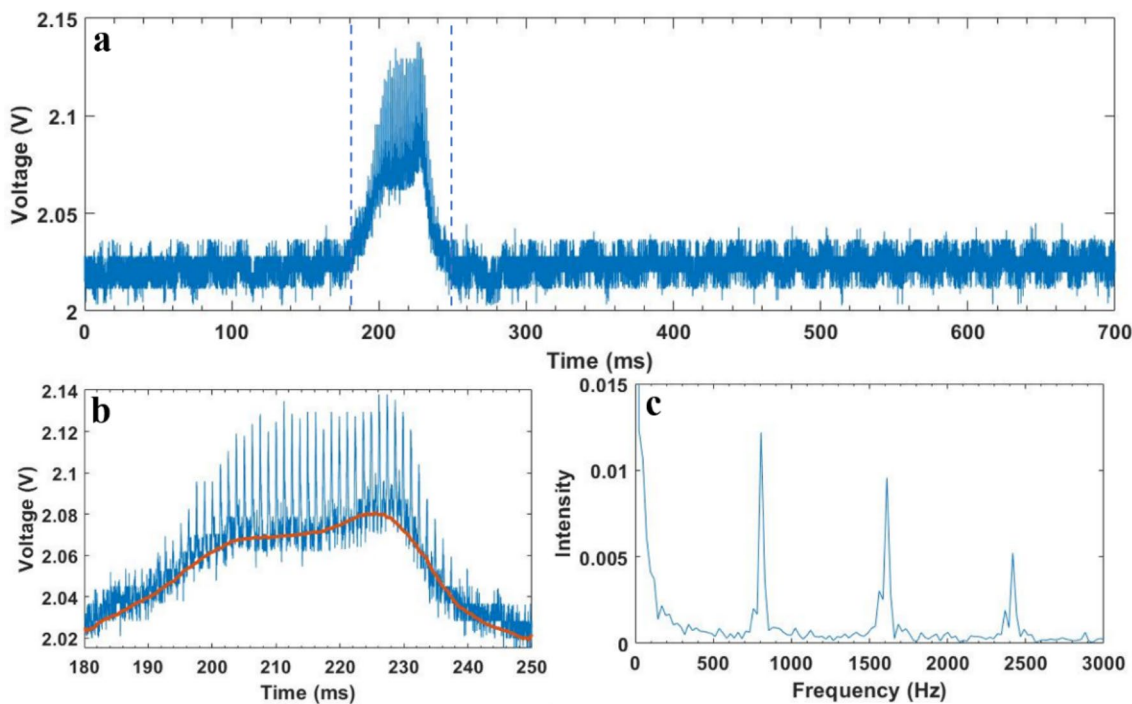


Fig. 4 Data recorded by the scatter counting system. **a** Mosquito signal recorded with an oscilloscope. **b** The mosquito signal within 180–250 ms; the red curve is the signal of the mosquito body. **c** Amplitude spectrum of the frequency contents of the mosquito wing-beat signal

in mosquito identification and counting, but it can also determine whether the mosquito is actually captured by the trap using time correlation. After a mosquito is recorded by the scattering system, if it continues to fly downwards, it will be recorded by the shadowing counting system, finally to arrive trapped at the lowest part, where a suction fan is installed. Being installed below the scattering counting system, the shading system has a time delay relative to the first system. However, there is a problem with the commercial trap in our application. High-speed fans can easily attract mosquitoes into the trap, but mosquitoes then pass the detection area quickly. If the wing-beat signal is obtained by lowering the wind speed, the frequency determination becomes more accurate, but the mosquito will easily escape from the trap and reduce the accuracy of counting. We installed a funnel-like device above the fan to reduce the wind speed in the detection area, as shown in Fig. 6a. This method not only results in good wing-beat signal from the mosquito but also prevents the mosquitoes from escaping once they enter the trap. However, this method still has a drawback, since mosquitoes entering the trap are fewer and mosquitoes may pass through the counting system more than once. Thus, a compromise must be found. The five amplified output signals of the two counting systems (the scattering system has one signal output, and the shading system has four signal outputs) are collected by a data acquisition card (N6211, National Instruments, USA).

In the upper container, shown in Fig. 6b, four mosquito samples of *Aedes albopictus* (male, female) and *Culex pipiens* (male, female), each with about 65, 40, 90, and 70 individuals were placed. Photographs of the four types of mosquitoes are given in Fig. 7. The outlet of the container is directly connected to the inlet of the counting system, and the mosquitoes inside the container go directly into the counting system. We studied possible differences between the two counting systems in the combined system to detect the wing-beat frequency of the same sample.

First, we recorded all mosquito signals for a specific species and sex by the shading and scatter counting system and performed fast Fourier transformation to obtain the wing-beat frequency of the sub-sample. Then, the individuals with wing-beat frequencies in adjacent 50 Hz frequency intervals were counted to make histograms, as shown in Figs. 8 and 9. We fit the wing-beat frequencies to a normal distribution to further analyze the data, as shown in the curves included in Figs. 8 and 9.

From Figs. 8 and 9, we can see that *Aedes albopictus* and *Culex pipiens* of different sex have a range of wing-beat frequency, but have only little overlap in the distributions. There is a quite good correlation between the fitted normal distribution curve and the distribution histogram. Therefore, the wing-beat frequency of *A. albopictus* and *C. pipiens* can be used as an important basis for male and female discrimination. The wing-beat frequency of males of *A. albopictus*

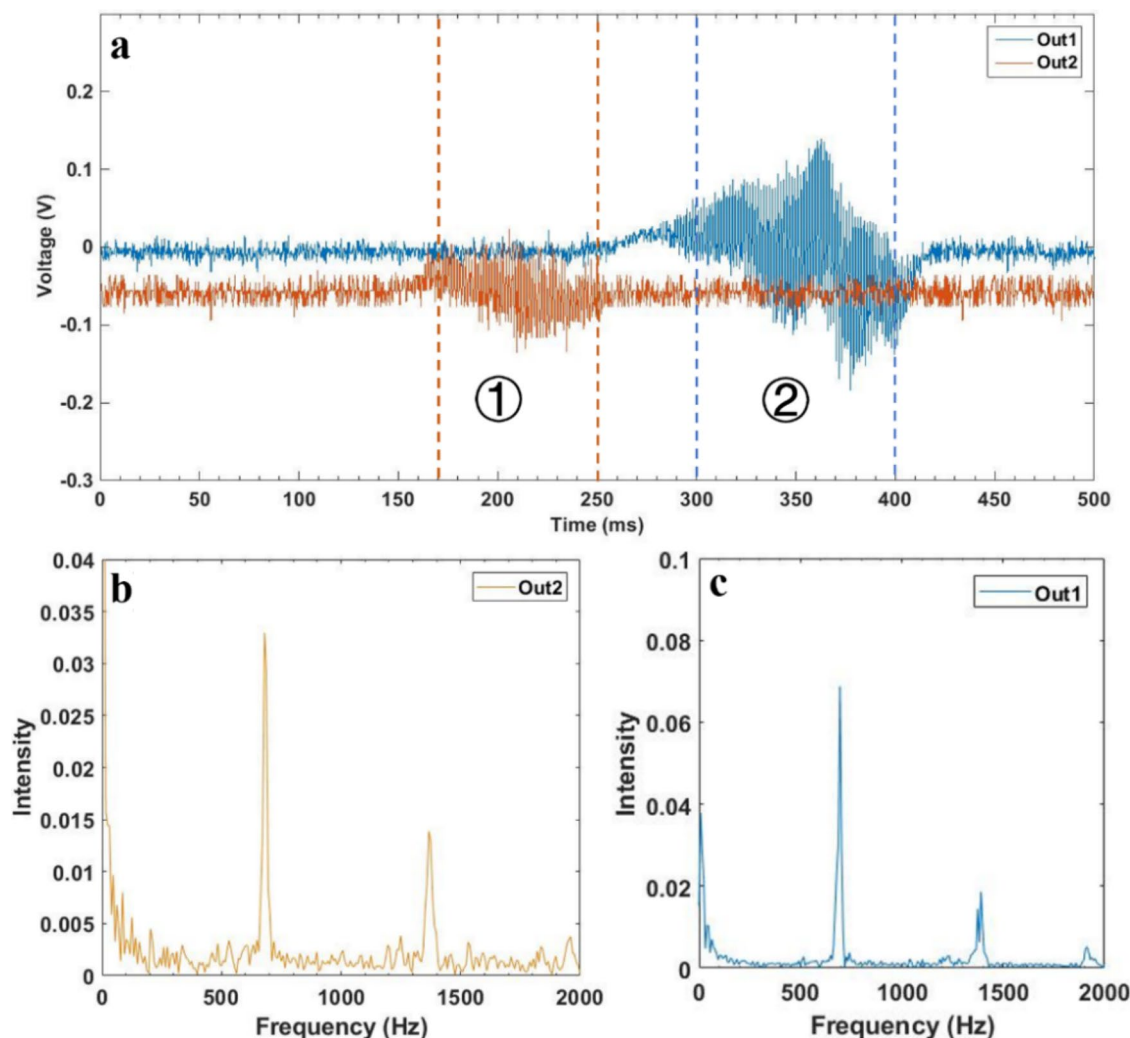
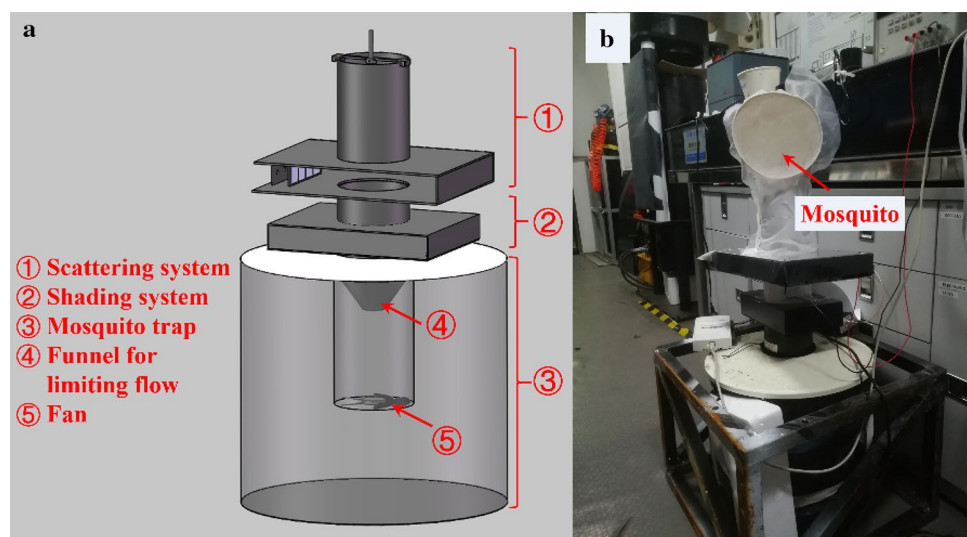


Fig. 5 Data recorded by the shadowing counting system. **a** The oscilloscope records the signals of the two-channel mosquito wing-beat. **b** Amplitude spectrum of the frequency contents of the Channel ①

signal is shown in (b), and the corresponding data for the Channel ② signal are given in (c)

Fig. 6 **a** Combined counting system structure diagram. **b** Photo of the composite mosquito counting system



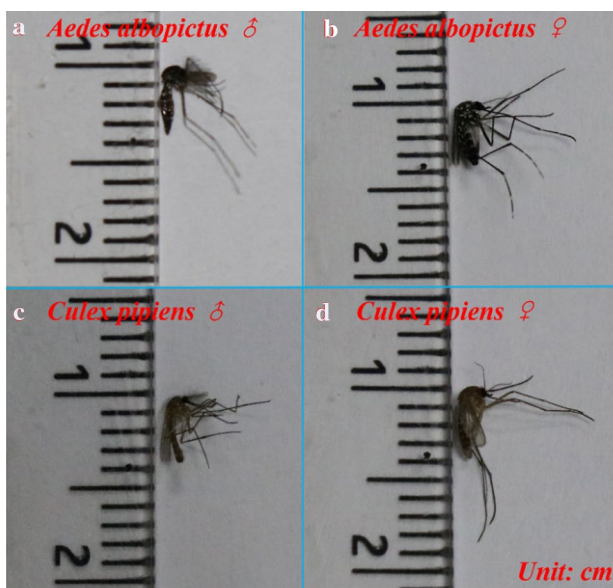


Fig. 7 Photographs of the four types of mosquitoes studied in the experiment

and *C. pipiens* is significantly higher than that of females. The frequency of wing-beat of *C. pipiens* is lower than that of *Aedes albopictus*. This may be due to the fact that the

body of *C. pipiens* is slightly larger than *A. albopictus*, as shown in Fig. 7. We also found that there is still considerable overlap in the range of wing-beat frequencies of *A. albopictus* and *C. pipiens* of the same sex, which makes it difficult to use the data as a basis for differentiation.

Figure 10 shows the normal distributions of the wing-beat frequencies of the same species of mosquitoes recorded by the two systems. We suspect that the small differences caused are due to the distance of the two counting systems away from the fan. Although we have made some restrictions on wind speed, it may still have some impact on the flight of mosquitoes. This may also contribute to a broadening of the wing-beat frequency distributions. Furthermore, we note that the fit to the *Aedes albopictus* female data in Fig. 9a is worse than for the other cases, which might contribute to the resulting small shift in center frequency.

3.3 Counting analysis

We compared the number of mosquito signals detected by the two systems with the number of actually captured mosquitoes. The results are shown in Fig. 11. The number of mosquitoes caught is the number of mosquitoes that are captured after they enter the trap, which we can easily obtain and which is very accurate. Due to the low wind speed in the

Fig. 8 Scattering counting system frequency distributions

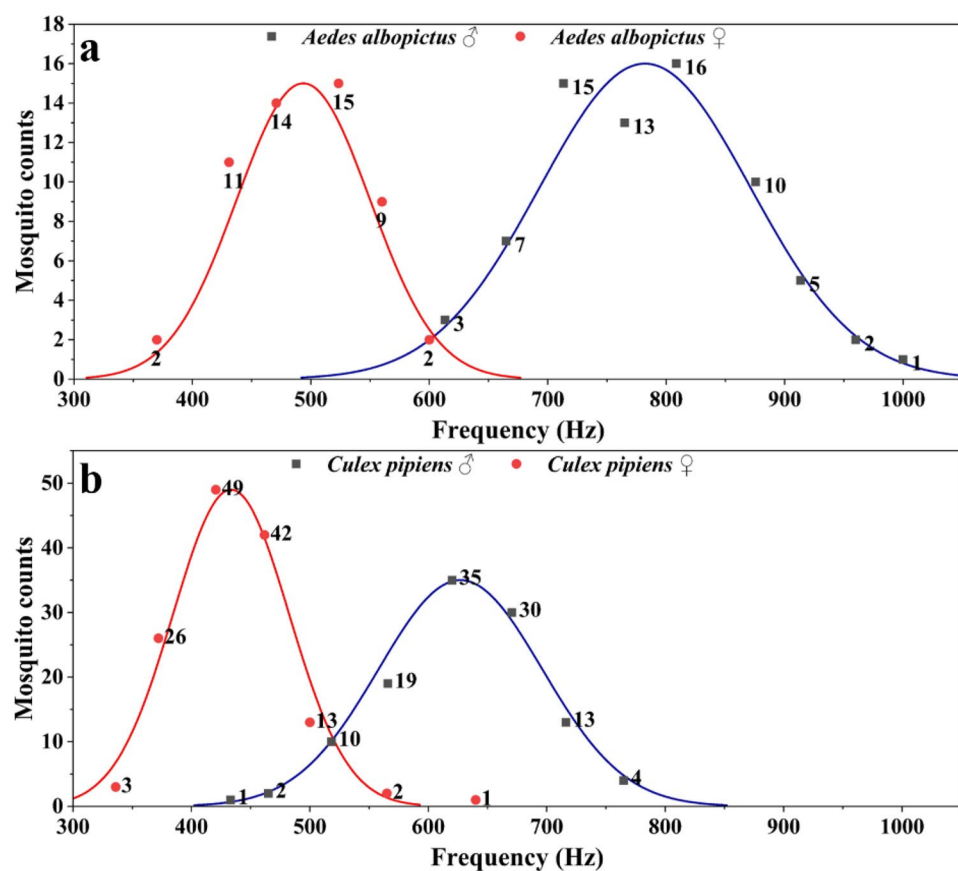
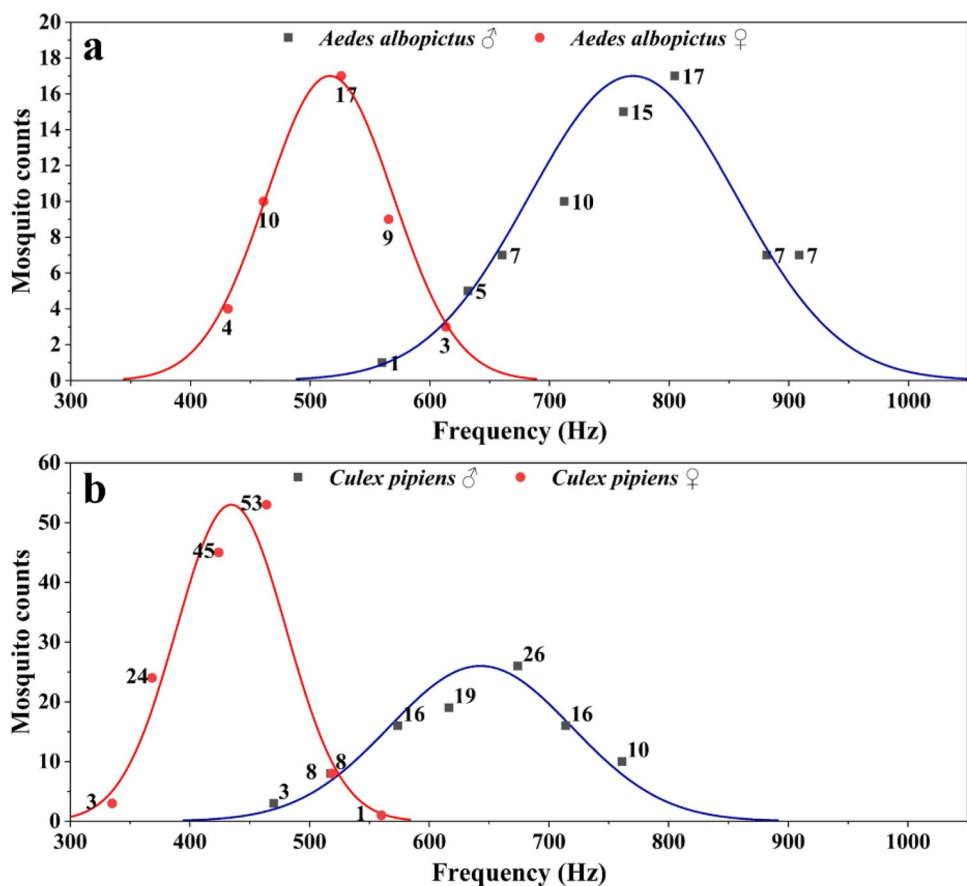


Fig. 9 Shading counting system frequency distributions



detection area, mosquitoes may pass through the detection area more than once, which increases the difficulty of counting. Here, we provide a counting method that combines the two systems, which we denote “METHOD”. If a mosquito is caught, it must be recorded by both counting systems and there will be some delay in time, which is a necessary condition for being caught by the trap. If it is only recorded by the scattering system and not recorded by the shading system, we do not think that it will be captured; even if the conditions for capture are fulfilled—whether we really observe the same individual is based on the detected frequency of the wing-beat. “METHOD” is a method of judging based on the two conditions of delay time and wing-beat frequency. This method can prevent mosquitoes from being repeatedly recorded by one of the counting systems.

As shown in Fig. 12, we found that *Culex pipiens* results in more signals from both systems. This may be because the body of *C. pipiens* is slightly larger than that of *Aedes albopictus*. At the same wind speed, *C. pipiens* can be more active in the system, so the chance of being recorded by a detector more than once is higher. The number of mosquitoes recorded by “METHOD” is less than the number of mosquitoes actually caught, except for female *C. pipiens*. This may be because the density of mosquitoes in the container is relatively large and the next mosquito may have

been recorded by the scattering system before the mosquito is recorded by the shading system.

The error rate for the system trap count which we define as:

$$\text{Error rate} = \frac{\text{METHOD} - \text{Catch}}{\text{Catch}} \times 100\%.$$

Compared to the statistical number of mosquitoes in a single counting system, the method which we provide effectively improves the accuracy of the counting.

4 Conclusions and discussion

We have used an insect trapping system, with one or the other of two optical insect recording systems placed to monitor insects passing the trap inlet. The recording systems are based on light scattering or light shadowing, respectively, and exhibited similar performance in test experiments with *Aedes albopictus*. By placing the systems one after the other in tandem on the trap inlet channel, enhanced monitoring capability is obtained. We used this tandem system and obtained a very good distinction between male and female of *A. albopictus* and *Culex pipiens* according to the frequency

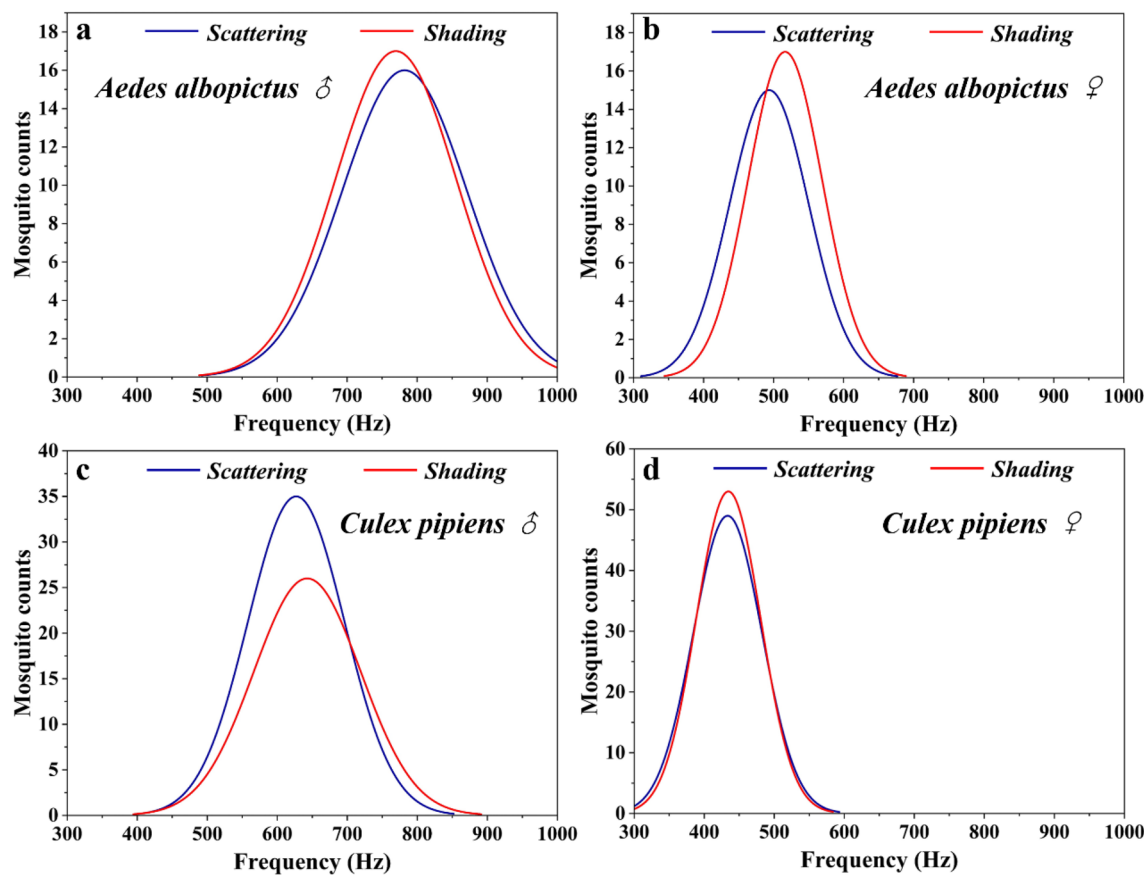
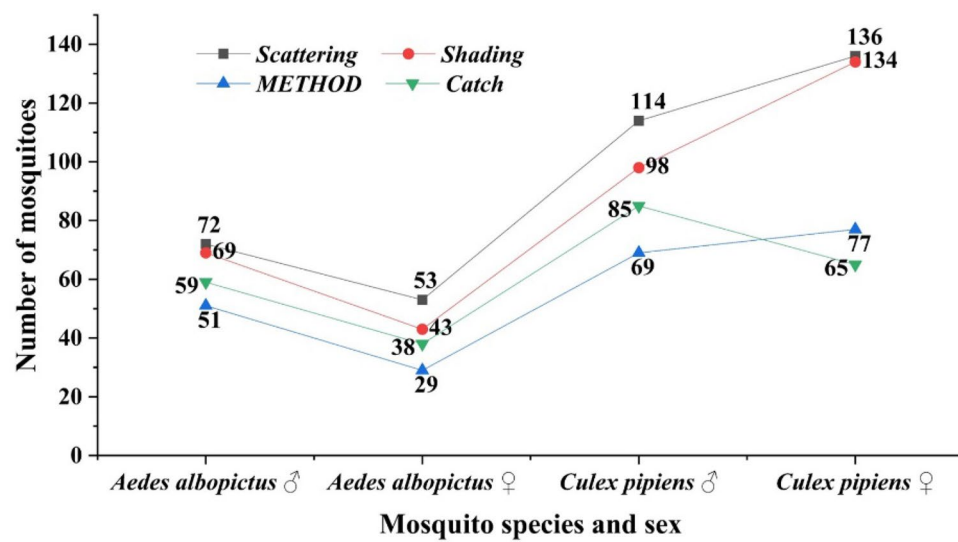


Fig. 10 The wing-beat frequency distributions recorded by the two counting systems

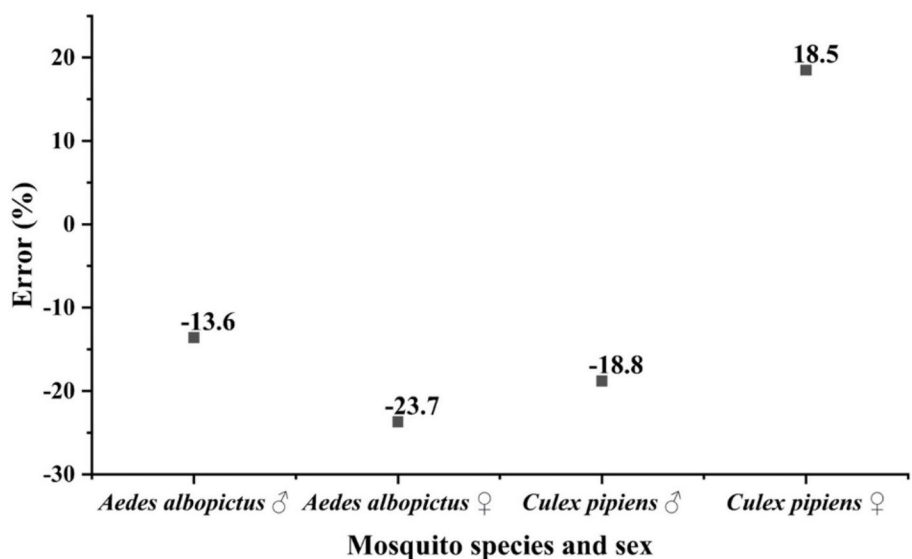
Fig. 11 Statistical diagram of the number of mosquitoes



of the wing-beat. However, the frequency of the wing-beat cannot be used as a basis for distinguishing *A. albopictus* and *C. pipiens*. We have proposed a statistical method, which improves the counting ability of the system.

In future field monitoring work, we can combine our techniques with standard attracting technology to improve the ability to capture mosquitoes. We can use ultraviolet light to achieve phototaxis (attraction to light) and chemicals that simulate the human-body odors to attract

Fig. 12 The distribution of the error rate of “METHOD”



mosquitoes and improve the practical ability of the system. With the development of the Internet of Things technology, we can also achieve wireless transmission of monitoring data to achieve a wide range of monitoring.

We now plan to perform extensive testing of the equipment with a variety of classified insects in preparation for field experiments.

We believe that our insect classification and counting system can be of considerable value in the management of disease-bearing insect vectors.

Acknowledgements Open access funding provided by Lund University. The authors thank Professors Sailing He and Guofu Zhou for support. We are also grateful to Xinghua Su and Professor Xiaodong Chen of Southern Medical University for providing well-classified insects, and to Dr Mikkel Brydegaard for discussions on electronic circuitry. We would also like to thank Zheng Duan, Ying Li, and Lingna Hu for assistance. This work was supported by the Guangdong Province Innovation Research Team Program (2010001D0104799318), the National Science Foundation of China (61705069), and the Chinese Ministry of Science and Technology through the National Key Research and Development Program of China (2018YFC1407503).

Open Access This article is licensed under a Creative Commons Attribution 4.0 International License, which permits use, sharing, adaptation, distribution and reproduction in any medium or format, as long as you give appropriate credit to the original author(s) and the source, provide a link to the Creative Commons licence, and indicate if changes were made. The images or other third party material in this article are included in the article's Creative Commons licence, unless indicated otherwise in a credit line to the material. If material is not included in the article's Creative Commons licence and your intended use is not permitted by statutory regulation or exceeds the permitted use, you will need to obtain permission directly from the copyright holder. To view a copy of this licence, visit <http://creativecommons.org/licenses/by/4.0/>.

References

1. J.G. Beeson, L. Kurtovic, C. Dobaño, D.H. Opi, J.A. Chan, G. Feng, M.F. Good, L. Reiling, M.J. Boyle, Challenges and strategies for developing efficacious and long-lasting malaria vaccines. *Sci. Transl. Med.* **11**(474), 1–17 (2019)
2. J. Friesen, O. Silvie, E.D. Putrianti, J.C.R. Hafalla, K. Matuschewski, S. Borrman, Natural immunization against malaria: causal prophylaxis with antibiotics. *Sci. Transl. Med.* **2**(40), 40–49 (2010)
3. S. Mharakurwa, P.E. Thuma, D.E. Norris, M. Mulenga, V. Chalwe, J. Chipeta, S. Munyati, S. Mutambu, P.R. Mason, Malaria epidemiology and control in Southern Africa. *Acta Trop.* **121**(3), 202–206 (2012)
4. C.P. Simmons, J.J. Farrar, N. van Vinh Chau, B. Wills, Dengue. *N. Engl. J. Med.* **366**(15), 1423–1432 (2012)
5. S. Bhatt, P.W. Gething, O.J. Brady, J.P. Messina, A.W. Farlow, C.L. Moyes, J.M. Drake, J.S. Brownstein, A.G. Hoen, O. Sankoh, The global distribution and burden of dengue. *Nature* **496**(7446), 504–507 (2013)
6. M.A. Johansson, P.F. Vasconcelos, J.E. Staples, The whole iceberg: estimating the incidence of yellow fever virus infection from the number of severe cases. *Trans. R. Soc. Trop. Med. Hyg.* **108**(8), 482–487 (2014)
7. S. G. Huang, M. Q. Zhou, G. H. Geng, X. L. Wang, Ontology-based insect recognition. In: International Conference on Image Analysis & Signal Processing (2009)
8. Y.W. Tian, Recognition method of insect damage and stem/calyx on apple based on hyperspectral imaging. *Trans. Chin. Soc. Agric. Eng.* **31**(4), 325–331 (2015)
9. H.T. Zhang, Y.X. Hu, H.Y. Zhang, Extraction and classifier design for image recognition of insect pests on field crops. *Adv. Mater. Res.* **756–759**, 4063–4067 (2013)
10. G. E. Meyer, Effect of image size and contrast on the recognition of insects in radiograms. In: Proceedings of SPIE - The International Society for Optical Engineering **1379** (1991)
11. J. Spitzen, W. Takken, Keeping track of mosquitoes: a review of tools to track, record and analyse mosquito flight. *Parasites Vectors* **11**(1), 1–11 (2018)
12. G. Gibson, A behavioural test of the sensitivity of a nocturnal mosquito, *Anopheles gambiae*, to dim white, red and infrared light. *Physiol. Entomol.* **20**(3), 224–228 (2010)

13. F. Hawkes, G. Gibson, Seeing is believing: the nocturnal malarial mosquito *Anopheles coluzzii* responds to visual host-cues when odour indicates a host is nearby. *Parasites & Vectors* **9**(1), 1–13 (2016)
14. D.A.A. Santos, J.J.P.C. Rodrigues, V. Furtado, K. Saleem, V. Korotaev, Automated electronic approaches for detecting disease vectors mosquitoes through the wing-beat frequency. *J. Clean. Prod.* **217**, 767–775 (2019)
15. D. Raman, R.R. Gerhardt, J.B. Wilkerson, Detecting insect flight sounds in the field: implications for acoustical counting of mosquitoes. *Trans. ASABE* **50**(4), 1481–1485 (2007)
16. M. Brydegaard, A. Gebru, S. Svanberg, Super resolution laser radar with blinking atmospheric particles—application to interacting flying insects. *Progress Electromagn. Res.* **147**, 141–151 (2014)
17. M. Brydegaard, Towards quantitative optical cross sections in entomological laser radar—potential of temporal and spherical parameterizations for identifying atmospheric fauna. *PLoS One* **10**(8), 1–15 (2015)
18. S.M. Zhu, E. Malmqvist, W.S. Li, S. Jansson, Y.Y. Li, Z. Duan, K. Svanberg, H.Q. Feng, Z.W. Song, G.Y. Zhao, M. Brydegaard, S. Svanberg, Insect abundance over Chinese rice fields in relation to environmental parameters, studied with a polarization-sensitive CW near-IR lidar system. *Appl. Phys. B* **123**(7), 211–221 (2017)
19. E. Malmqvist, S. Jansson, S.M. Zhu, W.S. Li, K. Svanberg, S. Svanberg, J. Rydell, Z.W. Song, J. Bood, M. Brydegaard, S. Akesson, The bat-bird-bug battle: daily flight activity of insects and their predators over a rice field revealed by high-resolution Scheimpflug Lidar. *R. Soc. Open Sci.* **5**(4), 1–12 (2018)
20. S. Jansson, P. Atkinson, R. Ignell, M. Brydegaard, First polarimetric investigation of malaria mosquitoes as lidar targets. *IEEE J. Sel. Top. Quantum Electron.* **25**(1), 1–8 (2019)
21. Z. W. Song, B. X. Zhang, H. Q. Feng, S. M. Zhu, L. N. Hu, M. Brydegaard, Y. Y. Li, S. Jansson, K. Svanberg, G. Y. Zhao, J. Bood, S. Svanberg, and D.S. Li, Application of lidar remote sensing of insects in agricultural entomology on the Chinese scene. *J. Appl. Entomology*. (2019). <https://doi.org/10.1111/jen.12714>
22. I. Potamitis, I. Rigakis, Measuring the fundamental frequency and the harmonic properties of the wingbeat of a large number of mosquitoes in flight using 2D optoacoustic sensors. *Appl. Acoust.* **109**(C), 54–60 (2016)
23. I. Potamitis, I. Rigakis, Large aperture optoelectronic devices to record and time-stamp insects' wingbeats. *IEEE Sens. J.* **16**(15), 6053–6061 (2016)
24. I. Potamitis, I. Rigakis, N.A. Tatlas, Automated surveillance of fruit flies. *Sensors (Basel)* **17**(1), 1–14 (2017)
25. I. Potamitis, I. Rigakis, N. Vidakis, M. Petousis, M. Weber, Affordable bimodal optical sensors to spread the use of automated insect monitoring, *J. Sens.*, (2018)
26. M. Weber, M. Geier, A. Rose, S. Sperling, and I. Potamitis, Automatic identification of the species and sex of captured mosquitoes in an advanced, remotely operated mosquito trapping system: technical background and results from the laboratory and field. In: Presented at the 85th ANCA Conference, Orlando (2019)

Publisher's Note Springer Nature remains neutral with regard to jurisdictional claims in published maps and institutional affiliations.

Article

Foreground Scattering Elimination by Inverse Lock-in-Like Spatial Modulation

Yueyu Lin ^{1,2,3}  and Sune Svanberg ^{1,2,3,*}

¹ National Center for International Research on Green Optoelectronics, South China Normal University, Guangzhou 510006, China; yueyu.lin@coer-scnu.org

² Guangdong Provincial Key Laboratory of Optical Information Materials and Technology & Center for Optical and Electromagnetic Research, South China Academy of Advanced Optoelectronics, South China Normal University, Guangzhou 510006, China

³ Department of Physics, Lund University, P.O. Box 118, SE-221 00 Lund, Sweden

* Correspondence: sune.svanberg@fysik.lth.se

Received: 9 July 2020; Accepted: 10 August 2020; Published: 13 August 2020



Abstract: We describe a simple approach to enhance vision, which is impaired by close range obscuring and/or scattering structures. Such structures may be found on a dirty windscreen of a car, or by tree branches blocking the vision of objects behind. The main idea is to spatially modulate the obscuration, either by periodically moving the detector/eye or by letting the obscuration modulate itself, such as branches swinging in the wind. The approach has similarities to electronic lock-in techniques, where the feature of interest is modulated to enable it to be isolated from the strong perturbing background, but now, we modulate the background instead to isolate the static feature of interest. Thus, the approach can be denoted as “inverse lock-in-like spatial modulation”. We also apply a new digital imaging processing technique based on a combination of the Interframe Difference and Gaussian Mixture models for digital separation between the objects of interest and the background, and make connections to the Gestalt vision psychology field.

Keywords: vision; scattering; modulation; lock-in techniques; background subtraction; Gestalt psychology

1. Introduction

Unimpaired vision is a very fundamental quality of life. Most visual defects can be corrected by glasses. Glare related to slant-angle specular reflections can be reduced by polarization filters. Good vision is also clearly related to adequate illumination. Normal human color vision requires object illumination by white light to activate our three types of color receptors, signaling particular colors after processing the color sensitive absorptions of the different image parts in the brain [1,2]. These receptors in the cones have low sensitivity and are, thus, inactive in low light level environments, where instead, the more sensitive rods are employed in black-and-white colorless vision. Thus, although the reflective “colors” are clearly physically equally present in low-light conditions, night vision devices employing, e.g., electro-optical image intensifiers, give black-and-white images only, actually black and green images, because of the emission characteristics of the most efficient electro-optical phosphor. However, night color vision can be obtained by separating different color bands before amplification, and then add the color coded enhanced images into a normal color image. This can be done by image processing, following, e.g., imaging color splitting by a split mirror Cassegrainian telescope, where three images are intensified simultaneously in a single unit [3]. Alternatively, rotating color-glass sectors are used in front of the image intensifier, which produces a magnified image on a white-phosphor screen, which is then observed through co-rotating color-glass sectors for flicker-less color image formation in the brain once the rotating frequency is high enough [4].

Vision can also be strongly influenced by the properties of the light transmission medium, normally the atmosphere. While there is no major molecular absorption in the spectral region of human vision (400–700 nm), scattering due to fog or smoke can certainly strongly impair vision. A remedy, frequently used in military applications, is to perform the observation at infra-red wavelengths, where Mie and Rayleigh scattering are less prominent due to the strong wavelength dependence of these processes [5,6].

A further origin of vision impairment is the scattering of a close lying, physically structured semi-transparent layer, making the contrast or isolation of remote objects very difficult. The present paper deals with this problem. We describe the phenomenon and provide a remedy based on vision physiology. We also make a connection to well-known digital imaging processing techniques used in background subtraction, and foreground removal by integral imaging.

2. The Problem and Its Solution

A common imaging situation yielding strongly impaired recognition is depicted in Figure 1. The objects of interest are at a distance but are viewed through a strongly scattering window, featuring structure. Light from the close lying object completely dominates over the light derived from the distant objects of interest. An everyday situation along the lines just described is viewing through a dirty or frosty windscreens while driving, making it difficult to see the road and the objects on or adjacent to the road. The common remedy is, of course, to use an efficient screen wiper, frequently combined with spraying the screen from outside with water or an anti-frost solution. Experience shows that this does not always make the situation satisfactory, especially not in situations with counter-illumination from the sun or from the headlights from approaching vehicles. The objects of interest remain hard to discern. We illustrate this situation in Figure 1.



Figure 1. Impaired vision sometimes encountered during nighttime driving. An animal, approaching from the left, is very hard to discern.

A further, somewhat different situation might be when the object is partly hidden by vegetation, i.e., leaves and branches, which may be moving in the wind. How could the object of interest behind be imaged clearly? Further, there may be raindrops or snowflakes falling in the line of sight to the object of interest, which impair vision. Such situations can be handled by well-known digital image processing techniques of background subtraction and integral imaging (see, e.g., [7–13]), but the human brain is also remarkably able to link together image elements, which are not accessible simultaneously, but only in a temporal sequence. We will discuss such situations in the present paper, while not covering cases when the object of interest is totally and permanently blocked from direct view, but where many interesting image processing approaches have recently been presented (see, e.g., [14], and references therein).

It is important to point out that we are also not considering situations where the scattering medium is more or less homogeneous, such as fog or biological tissue. Then the object of interest, frequently having sharp structures, is observed on a strong, homogenous background, making contrast minute or absent. For such situations, new and fascinating methods have recently been developed based on scattering compensation with spatial light modulators, etc. [15–18]. We are also not considering cases when the illumination of the object can be made structured, to ensure a spatial tagging, which enhances the object while reducing the non-structured background, e.g., in SLIPI (structured laser illumination planar imaging) applications [19,20]. A further way to enhance distinct distant objects over a close lying scattering medium (whether homogeneous or structured) is to simply apply far field focusing, resulting in distant objects of interest with sharp edges, which can be enhanced by digital processing [1,21,22].

The motivation to the present approach for improved vision comes from concepts of frequency and phase tagged (lock-in) detection, frequently used for retrieving weak signals residing on a strong background. The idea here is to identify the feature of interest by modulating some parameter related to the feature only, while not affecting the background. Examples of this approach are numerous in the field of spectroscopy, e.g., in wavelength modulation in diode-laser absorption spectroscopy, where the derivative of a weak but sharp absorption structure is observed by modulating the wavelength to an extent corresponding to a fraction of the feature line width (see, e.g., [23]). Another example is found in optical pumping or optical double resonance experiments [23], where the radiofrequency field inducing transitions between atomic sublevels is chopped on and off, and the minute changes in the detected light due to the action of the radio frequency are monitored selectively. The idea is to lift off and isolate the signal due to the feature of interest from the unrelated strong background. An imaging variety of such an approach could be to use modulated illumination for vision enhancement. Such illumination modulation could be taken, e.g., at nighttime driving, where the (LED) headlights of your car might be modulated in intensity (above the flicker frequency). Normal human vision would then be supported by a forward-looking video camera (possibly with a head-up display), which records synchronously and in phase with your own modulation, to enhance objects of interest to you, while direct light, or windscreens scattered light, from meeting car headlights, would be suppressed since it would be of a different modulation frequency and/or phase.

We will here focus on a different and more general approach for vision enhancement, where the enhancement occurs on the detection side only, rather than also taking the illumination side into account. One important application is when no artificial illumination occurs, e.g., in daylight applications, where the illumination obviously cannot be modulated, enabling the object of interest to be isolated from the disturbing background. The bearing principle in this paper is then to modulate instead the disturbing background, of which we can have control. It is achieved by a systematic spatial modulation by a periodic movement of the detector. If a total signal is observed and part of that signal is modulated, it can be lifted off, leaving the (frequently weak) residue isolated and clearly identifiable. Since the technique utilizes modulation, but for the opposite purpose as normally employed, the new approach could be denoted as “inverse lock-in-like spatial modulation” (ILLSPAM). A situation where spatial modulation could be implemented is the one shown in Figure 1.

3. Practical Implementation

The implementation of the proposed technique, using the physiology of vision and image perception, is the most straightforward application. The eye/brain system has an impressive power to “stabilize” an image, even if the detector is moving, and can easily discern the static parts of an image, while large parts of the “image” characterized by a periodic or uniform movement can be disregarded. Regarding vision psychology, there is a clear connection to the well-established *Gestalt* direction of vision apprehension (see, e.g., [24,25] and references therein). Here, the “figure–ground segregation” approach is taken, emphasizing the capability of the brain to figure out contexts, when considering the “whole” as a concept, in contrast to “the sum of the parts”; a holistic situation pertains. We, in the present treatment, more focus on the parallels to electronic signal enhancement, making the connection

to electronic lock-in isolation of the feature of interest. We put our approach in perspective to all the recent technological developments in vision enhancement in environments impaired by scattering.

An illustrative example, which is quite useful for drivers, is illustrated in Figure 2. If surprised with a sudden situation with foreground scattering, due to the headlights of a meeting car, as illustrated in Figure 1, or the impact of strong, counter sunlight, such as in Figure 2, vision is strongly impaired. For the latter case, the resulting image Figure 2c consists of the background scene of interest, as shown in Figure 2a, and the close-by foreground scene shown in Figure 2b added scattering dirt on the windscreen. The suggested method to isolate the two scenes for obtaining a better vision of the scene in Figure 2a is to move the head a few centimeters up and down periodically and concentrate on the nonmoving parts of the scene observed. This is illustrated in the movie, connected to Figure 2c, where the foreground scattering image, Figure 2b, is moved periodically up and down to simulate the car driving situation (Supplementary Materials, Video S1). We can clearly see how the physiological vision approach works very well to increase the apprehension of the road situation, including the pedestrian and the animal.

Likewise, the eye/brain can easily see and “lock” on a building, partly blocked by, e.g., close-distance tree branches, moving in the wind and exposing different parts of the building at different times, as further discussed below.

The simple physiological approach proposed above brings to mind a further, somewhat trivial trick, well known to myopic persons, who at nighttime from the bed would see a completely blurred distant LED-based clock, which becomes crystal clear, if observed through the small opening between the thumb and two fingers brought tightly together at their tips (central-ray imaging)!

Many digital image processing approaches of removing obscuring foreground or removal of uninteresting background have been developed (see, e.g., [7–13]), and we will put the new physiological approach into perspective by showing an illustrative example, where a standard smartphone is utilized. The approach can be readily applied to the case of active spatial modulation of a close range partially obstructing object (say, a dirty windscreen) when the camera or an attached optical arrangement is periodically spatially translated. Cases of passive, close or far range modulation can also be considered when, e.g., vegetation, rain, or snow in motion impairs the visualization of a distant object, e.g., a building.

We will now put the physiological vision approach in relation to digital image processing and will present a method to isolate the objects of interest. Figure 3 illustrates a laboratory set up, where a fixed smartphone camera was subjected to a transparent screen, 0.5 m from the camera, which was cluttered with an irregular pattern of scattering grey spots, and which were in periodic motion. An object of interest (the logos of the participating universities) was placed at a distance of 1 m, as seen in the background of Figure 3. Images were recorded with successive displacements of the disturbing cluttering screen.

Figure 4a shows an individual frame, where parts of the object of interest were blocked, while the right-hand part shows a processed image, which was mostly free of obstruction. A short video sequence is displayed in Video S2 in the Supplementary Materials, with individual frames occurring to the left, while the video sequence, processed as indicated above, is playing to the right in the figure, without obstruction. We note that the “modulation frequency”, i.e., the rate of foreground movement should be substantially higher than that of the scene recorded to achieve an optimal processed image impression for the case that the image parts of interest would be moving. Then our procedure was performed with the reconstructed image calculated as a “sliding average”, and the objects of interest appeared in a somewhat delayed film.

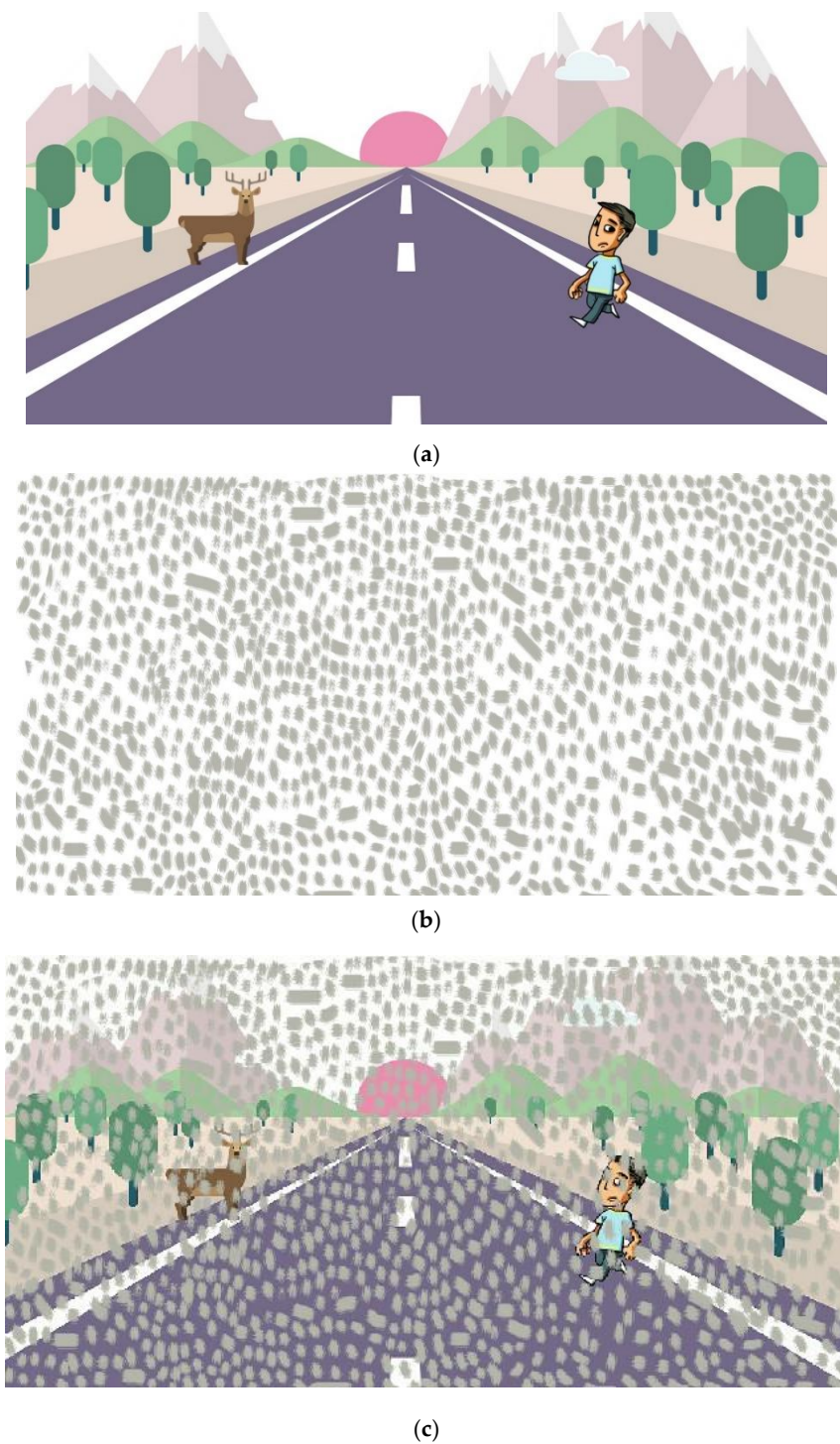


Figure 2. Illustration of how impaired vision sometimes encountered during car driving can be improved by a simple spatial modulation approach, utilizing the unprecedented image processing capability of the human brain. (a) The scene we want to observe without any image blurring; (b) Foreground image blurring, due to, e.g., dirt on the windsscreen; (c) The resulting blurred image obtained as a result of the superposition of Figure 2a,b. Video S1 in the Supplementary Materials shows how Figure 2b is periodically translated up and down in front of Figure 2a, simulating a periodic movement of the observers head.



Figure 3. The laboratory setup with the object, the obscuring foreground screen and the smartphone video camera. (left) schematic setup, and (right) a photograph of the setup.



Figure 4. Individual frame (a) and a digitally processed image (b). Video S2 in the Supplementary Material shows a short sequence, with individual partly obscured frames to the left.

The approach we used in our demonstration, shown in Figure 4, is based on two already known methods. The Interframe Difference Method [11] is commonly used in motion detection, while it is not sensitive to targets, which are moving slowly. However, the Interframe Difference Method is simple and has good stability for light variations. The Gaussian Mixture Model (GMM) [12] builds the background by using M models, which come from the intensity of pixels. It also cannot detect targets with slow speed, because it builds the background by prehistory. GMM collects the intensity of a particular pixel value over a period of time for modeling. If the target moves slowly, it can wrongly be classified as a non-interesting (background) information, because the intensity of the pixel does not change much. At the same time, the Gaussian mixture model cannot deal with the problems arising from light changes because the background quality obtained by GMM often depends on the prehistory. We operated an interframe action based on the result obtained from GMM. It improved the sensitivity of GMM to light changes and improved the quality of background models as a feedback variable. By combining the two methods in our approach, certain advantages were obtained. We proceed as outlined below:

1. To increase the adaptability in updating of the training set, we defined a time T as the interval for the repeated processes of adding a new frame and discarding the oldest one. To prevent excessive computation time or possible motion, T should not be chosen too long. At time $t-1$, we then had the data set χ_{T-1} :

$$\chi_{T-1} = \{x^{(t-1)}, \dots, x^{(t-1-T)}\} \quad (1)$$

Here, $x^{(t-1)}$ is the current pixel value at time $t - 1$. The probability of observing the current pixel value $p(x)$ is:

$$p(x) = \sum_{m=1}^M \omega_m \cdot \eta(x; \mu_m, \sigma_m^2) \quad (2)$$

Here, the ω_m , values, which are positive and estimate the mixing weights, add up to one at time t . μ_m is the mean value of the i -th ($1 \leq i \leq m$) Gaussian in the mixture, and σ_m^2 is the estimate of the variance that describes the Gaussian models at time t . η is a Gaussian probability density function:

$$\eta(x; \mu, \sigma^2) = \frac{1}{(2\pi\sigma^2)^{\frac{1}{2}}} e^{-\frac{(x-\mu)^2}{2\sigma^2}} \quad (3)$$

2. In every time period, T , foreground and background pixels were present at the same time. Considering the background target as always stable and similar, we ranked all the Gaussian models according to the estimated mixing weights ω_m . So we could approximate the background model from the first B largest models (i.e., those having the largest mixing weights). The probability of observing the current background pixel value $p(X|BG)$ should be:

$$p(X|BG) = \sum_{m=1}^B \omega_m \cdot \eta(x; \mu_m, \sigma_m^2) \quad (4)$$

3. When a new frame comes (at time t), we did the following calculation for all the pixels in this frame. We calculated the distance between the pixel value x and the mean value of all Gaussian distributions in the mixed Gaussian model. If one of the distances was less than 2.5 times its standard deviation, we could say the pixel value x was defined as a background pixel belonging to the i -th ($1 \leq i \leq m$) Gaussian model. By doing this, we could figure out the background (static parts) and foreground (moving objects) in the frame. After calculation, the frame pixels could be divided into foreground and background pixels according to the following relation:

$$f_c(x, y) = \begin{cases} B(x, y), & \text{if } |f_c(x, y) - \mu_{m,t}| \leq 2.5\sigma_{m,t} \\ F(x, y), & \text{otherwise} \end{cases}, \quad (5)$$

Here, $f_c(x, y)$, $B(x, y)$ and $F(x, y)$ are the current frame, background frame parts (static parts), and the current foreground frame parts (moving objects).

4. After step 3, we built a temporary background image $BG(x, y)$ based on the background B_{n-1} corresponding to the previous frame. The pixels in B_{n-1} which locate in the area of $B(x, y)$ in function 5 were updated by using the pixel value which was in the same location $f_c(x, y)$. The other pixels in the area of $F(x, y)$ in function 5 remained the same.
5. We converted the current frame $f_c(x, y)$ and temporary background image $BG(x, y)$ at time t to gray images $f_{cg}(x, y)$ and $BG_g(x, y)$. Then we did the subtraction with the two pixel values of the corresponding position. If the distance between the pixel in $f_{cg}(x, y)$ and the corresponding pixel in $BG_g(x, y)$ was smaller than an adaptive threshold H , this meant that the current pixel could be considered as a background pixel. The gray frame could be divided into gray foreground and gray background according to the following relation:

$$f_{cg}(x, y) = \begin{cases} B_g(x, y), & \text{if } |f_{cg}(x, y) - BG_g(x, y)| \leq H \\ F_g(x, y), & \text{otherwise} \end{cases}, \quad (6)$$

6. After step 5, we could reconstruct the new background B_n at time t based on the background B_{n-1} corresponding to the previous frame. The new background B_n could be obtained as follows:

Based on B_{n-1} , update the pixels which locate in the area of $B_g(x, y)$ in function 6 by using the pixel values which are in the same location in the current frame $f_c(x, y)$. The other pixels which locate in the area of $F_g(x, y)$ remain the same.

7. When a new frame arrives, loop steps 1 through 6 to update the background.

Based on the result of the Gaussian mixture model (GMM), we performed a subtraction with the corresponding frame, which means that we combined these two methods. To evaluate the results of our approach, we used the CDnet2014 data [13] to test it. We used the “intermittentObjectMotion” and “thermal video” data files available at the site. We compared our method with the Gaussian Mixture Model (GMM) [12] and the Interframe Difference Method [11]. The data set also has an official test code that specifically tests the effectiveness of different methods. However, the test code only tests the moving parts to evaluate the results of background reconstruction. Now, instead of eliminating the moving parts of the image, as done in Figure 4, we focused on the moving parts. The results regarding the identification of the moving parts (the foreground) are shown in Figure 5.

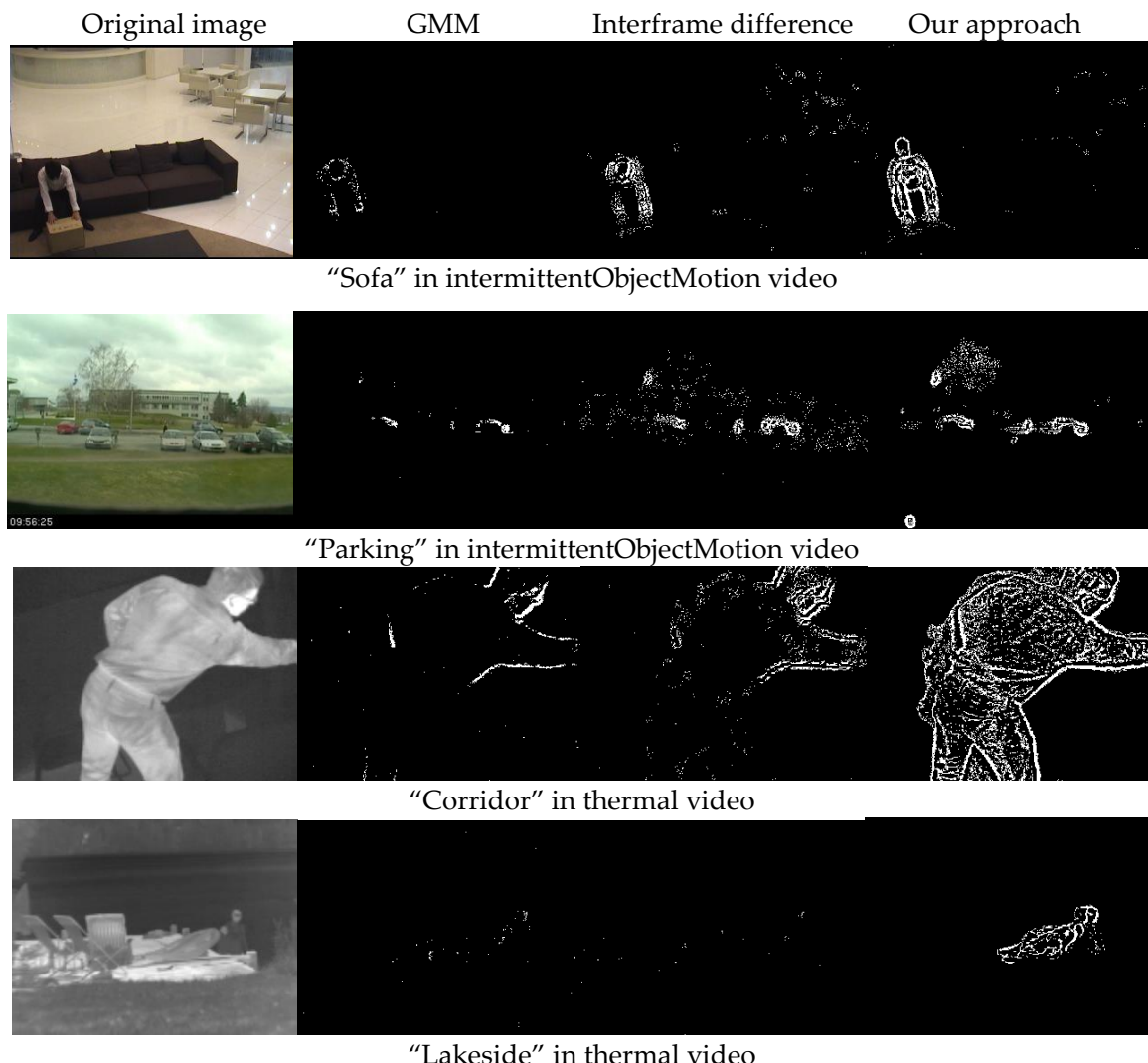


Figure 5. Comparison of benchmark videos between our approach and other approaches. From left to right for each scene, we present the original image, and the results for the foreground (the moving part) obtained with the Gaussian Mixture Model (GMM), the Interframe Difference Model and our new approach.

We note that a better image comprehension was obtained with our new method. However, we also applied more objective general foreground detection evaluation indices to compare the performance of our approach with two other approaches. The indices *Recall*, *Precision*, *PWC*, and *F-measure* were chosen, with the following definitions:

$$\text{Recall} = \frac{TP}{TP + FN} \quad (7)$$

$$\text{Precision} = \frac{TP}{TP + FP} \quad (8)$$

$$\text{PWC} = 100 * \frac{FN + FP}{TP + FN + FP + TN} \quad (9)$$

$$F\text{-measure} = 2 * \frac{\text{Precision} * \text{Recall}}{\text{Precision} + \text{Recall}} \quad (10)$$

Here, *TP*, *TN*, *FP*, and *FN* denote true positive rate, true negative rate, false positive rate, and false negative rate regarding the pixel identification. After running the test code, the indices were generated automatically. Each type of sequence contained different kinds of categories, and the average indices were saved in a text file. The average results are shown in the form of a line chart in Figure 6.

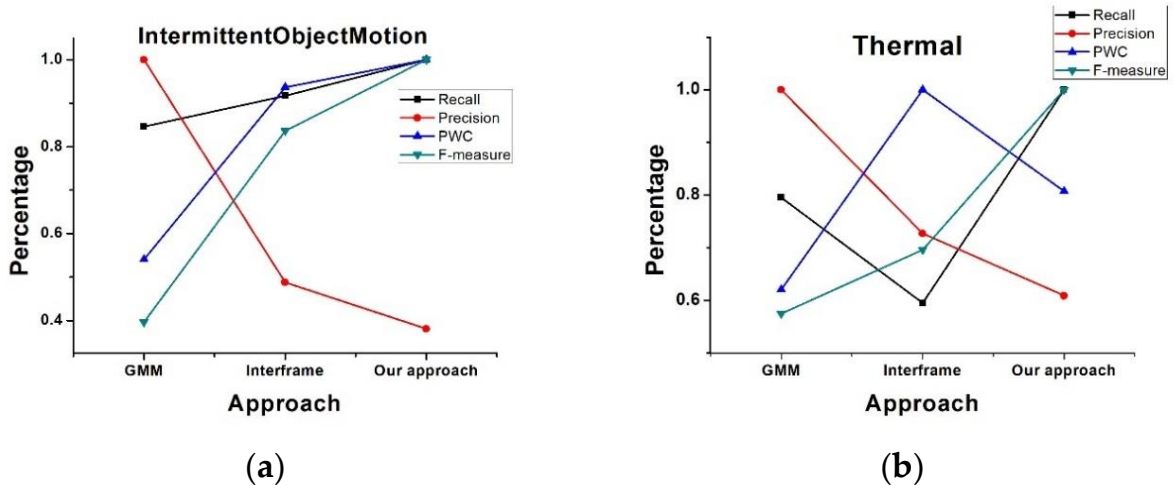


Figure 6. Comparison of evaluation indices of various approaches. (a) Performances of different approaches in intermittentObjectMotion video. (b) Performances of different approaches in thermal video.

From 6a, we can see the *Recall*, *PWC*, and *F-measure* curves were better than for the other two approaches applied to the intermittent ObjectMotion videos. Although *PWC* of our approach was not the best in the thermal videos (right), the *Recall* and *F-measure* values were still good. We can also see that *Precision* of our approach was the worst in both two types of videos, which was due to our sensitivity to light change. In a next step, we will focus on the ability to handle light changes to achieve higher *Precision* values.

4. Discussion

We note that the aspect primarily utilized in the present approach to foreground scattering elimination was that the object of interest does not move, or at least does not move in concord with the imposed modulation. We employed modulation (by, e.g., moving the eyes/head periodically slightly up and down) at a rate allowing the object of interest to be quasi static over a period when the foreground blurring pattern moved periodically. We considered the parallel to normal lock-in (frequency- and phase-tagged) detection. In this case, the modulation must be fast enough to move away from the strongest influence of the 1/f noise in the non-interesting, overwhelming signal contributions that

we wanted to discriminate against. Here, an increased spatial modulation frequency allowed us instead to mark the background clearly so that it could be discerned against the desired, weaker signal. We achieved the improved vision by using the image processing capability of the human brain, as shown in Figure 2, or by computerized image processing, as illustrated in Figure 4.

Instead of moving the detector, the foreground scattering object may instead be moved. Again, the physiological image processing of the brain could be used similarly, as illustrated in Figure 2. Clearly, here, digital image processing of the recordings of a fixed camera could also be used to eliminate the disturbing, partially obstructing close range perturbation, as illustrated in Figure 4. Incidentally, we note that a rotating round window is sometimes installed on the bridge of ships—but now for the purpose of screen wiping without moving the wiper, but rather the window. We note that even if there were no wipers, the present method would allow better vision of distant objects.

We introduced a new method, combining the established Interframe Difference and Gaussian Mixture Models to digitally separate moving and static parts of a video sequence, and demonstrated certain advantages, while there is still room for improvements, by appropriate handling of intensity variations.

We noticed that in the physiological imaging process, the brain over some time “remembers” the parts of the scene, which were non-obscured at a certain time, and is able to add to that later observed parts, which were subsequently uncovered, and finally, to synthesize a full image of the object, at any time partially obscured. This relates to the Gestalt direction of vision psychology [24,25]. This field, with origins back over 100 years [26], continues to attract much attention (see, e.g., [27,28]), and analyzes the fascinating capability of human vision to ensure that “the perceptual whole is more than the sum of the parts”.

Customary imaging techniques used in video conferencing could apply, where only the moving parts of the frame (e.g., the mouth of a speaking person) are updated at video rates, while the “static” features, such as the conference room, remain at a relatively slow updating rate, thus massively saving transmission bandwidth. In the cases that we discuss, we instead eliminated the moving parts and focused on the “semi-static parts”, which constituted our object to be visualized. Again, the analog to the lock-in concept comes to mind; however, now ignoring the modulated part and focusing on the “static background”—making further meaning to the suggested acronym “inverse lock-in-like spatial modulation, ILLSPAM”. We note that the concept of modulating an accessible background instead of the feature of interest, when inaccessible for modulation, may have important applications also outside the field of vision.

Supplementary Materials: The following are available online at <http://www.mdpi.com/2411-5150/4/3/37/s1>, Video S1: Figure 2 animation; Video S2: Figure 4 animation.

Author Contributions: All authors have read and agreed to the published version of the manuscript. Conceptualization, S.S.; Data curation, Y.L.; Funding acquisition, S.S.; Investigation, S.S.; Software, Y.L.; Supervision, S.S.; Visualization, Y.L.; Writing—original draft, S.S.

Funding: This work was partially funded by the SCNU Study Abroad Program for Elite Postgraduate Students, the Science and Technology Program of Guangzhou (No. 2019050001), and the Guangdong Provincial Key Laboratory of Optical Information Materials and Technology (No. 2017B030301007).

Acknowledgments: We gratefully acknowledge the support of Sailing He, Guofu Zhou, and Karl Åström. We are also very grateful to an anonymous reviewer, who brought to our attention the relation of our work to Gestalt psychology.

Conflicts of Interest: The authors declare no conflict of interest.

References

1. Watson, A.B. (Ed.) *Digital Images and Human Vision*; Bradford Books, MIT Press: Cambridge, MA, USA, 1993.
2. Li, Z.P. *Understanding Vision, Theory, Models and Data*; Oxford University Press: Oxford, UK, 2014.
3. Svanberg, S. Color image registration in low-light-level conditions. Swedish Patent SE 468 414, 1993.

4. Svanberg, S.; Johansson, J. Image registering in color at low light intensity. US Patent 5 483 379. European Patent 0584163, 1996.
5. Farmer, W.M. *The Atmospheric Filter*; JCD Publishing: Oviedo, FL, USA, 2001; Volumes 1 and 2.
6. Vollmer, M.; Möllmann, K.-P. *Infrared Thermal Imaging—Fundamentals, Research and Applications*; Wiley-VCH: Weinheim, Germany, 2010.
7. Szeliski, R. *Computer Vision—Algorithms and Applications*; Springer: Berlin/Heidelberg, Germany, 2010; p. 531. [[CrossRef](#)]
8. Toyama, K.; Krumm, J.; Brumitt, B.; Meyers, B. Wallflower: Principles and practice of background maintenance. In Proceedings of the Seventh International Conference on Computer Vision (ICCV'99), Kerkyra, Greece, 20–27 September 1999; pp. 255–261.
9. Hong, S.-H.; Jang, J.-S.; Javidi, B. Three-dimensional volumetric object reconstruction using computational integral imaging. *Opt. Express* **2004**, *12*, 483–491. [[CrossRef](#)] [[PubMed](#)]
10. Xiao, X.; Javidi, B.; Martinez-Corral, M.; Stern, A. Advances in three-dimensional integral imaging: Sensing, display, and applications. *Appl. Opt.* **2013**, *52*, 546–560. [[CrossRef](#)] [[PubMed](#)]
11. Lipton, A.J.; Fujiyoshi, H.; Patil, R.S. Moving target classification and tracking from real-time video. In Proceedings of the Fourth IEEE Workshop on Applications of Computer Vision, Princeton, NJ, USA, 19–21 October 1998; pp. 8–14.
12. Stauffer, C.; Grimson, W.E.L. Adaptive background mixture models for real-time tracking. In Proceedings of the Computer Vision and Pattern Recognition Conference, Fort Collins, CO, USA, 23–25 June 1999; pp. 246–252.
13. Goyette, N.; Jodoin, P.; Porikli, F.; Konrad, J.; Ishwar, P. Chagedetection.net: A new change detection benchmark dataset. In Proceedings of the Computer Vision and Pattern Recognition Conference, Providence, RI, USA, 16–21 June, 2012; pp. 1–8.
14. O'Toole, M.; Lindell, D.B.; Wetstein, G. Confocal non-line-of-sight imaging based on light-cone transformation. *Nature* **2018**, *555*, 338–341. [[CrossRef](#)] [[PubMed](#)]
15. Vellekoop, I.M.; Mosk, A.P. Phase control algorithms for focusing light through turbid media. *Opt. Commun.* **2008**, *281*, 3071–3080. [[CrossRef](#)]
16. Vellekoop, I.M.; Lagendijk, A.; Mosk, A.P. Exploiting disorder for perfect focusing. *Nat. Photonics* **2010**, *4*, 320–322. [[CrossRef](#)]
17. Vellekoop, I.M. Feed-back based wavefront sensing. *Opt. Express* **2015**, *23*, 12189. [[CrossRef](#)] [[PubMed](#)]
18. Yu, H.; Lee, J.P.; Lee, K.; Jang, J.; Lim, J.; Yang, W.; Jeong, Y.; Park, Y. In vivo deep tissue imaging using wavefront shaping optical coherence tomography. *J. Biomed. Opt.* **2016**, *21*, 101406. [[CrossRef](#)] [[PubMed](#)]
19. Kristensson, E.; Berrocal, E.; Wellander, R.; Richter, M.; Aldén, M.; Linne, M. Structured illumination for 3-D Mie imaging and 2-D attenuation measurements in optically dense sprays. *Proc. Comb. Institute* **2011**, *33*, 855–861. [[CrossRef](#)]
20. Kristensson, E.; Bood, J.; Aldén, M.; Nordström, E.; Zhu, J.J.; Huldt, S.; Bengtsson, P.E.; Nilsson, E. Berrocal, H.; Ehn, A. Stray light suppression in spectroscopy using periodic shadowing. *Opt. Express* **2014**, *22*, 7711–7721. [[CrossRef](#)] [[PubMed](#)]
21. Solomon, C.; Breckon, T. *Fundamentals of Digital Image Processing*; Wiley-Blackwell: Hoboken, NJ, USA, 2011.
22. Gonzales, R.C.; Woods, R.E. *Digital Image Processing*, 4th ed.; Pearson: London, UK, 2018.
23. Svanberg, S. *Atomic and Molecular Spectroscopy—Basic Aspects and Practical Applications*, 4th ed.; Springer: Berlin/Heidelberg, Germany, 2004; Chapters 7 and 10.
24. Wagemans, J.; Elder, J.H.; Kubovy, M.; Palmer, S.E.; Peterson, M.A.; Singh, M.; von der Heydt, R. A century of Gestalt psychology in visual perception: I. Perceptual grouping and figure-ground organization. *Psychol. Bull.* **2012**, *138*, 1172–1217. [[CrossRef](#)] [[PubMed](#)]
25. Wagemans, J.; Feldman, J.; Gepshtein, S.; Kimchi, R.; Pomerantz, J.R.; van der Helm, P.A.; van Leeuwen, C. A century of Gestalt psychology in visual perception: II. Conceptual and theoretical foundations. *Psychol. Bull.* **2012**, *138*, 1218–1252. [[CrossRef](#)] [[PubMed](#)]
26. Wertheimer, M. Experimentelle Studien über das Sehen von Bewegung [Experimental studies on the seeing of motion]. *Z. Psychol.* **1912**, *61*, 161–265.

27. Nie, Q.-Y.; Maurer, M.; Müller, H.J.; Conci, M. Inhibition drives configural superiority of illusory Gestalt: Combined behavioral and drift-diffusion model evidence. *Cognition* **2016**, *150*, 150–162. [CrossRef] [PubMed]
28. Costa, T.L.; Orsten-Hooge, K.; Rego, G.G.; Wagemans, J.; Pomerantz, J.R.; Boggio, P.S. Neural signatures of the configural superiority effect and fundamental emergent features in human vision. *Sci. Rep.* **2018**, *8*, 13954. [CrossRef] [PubMed]



© 2020 by the authors. Licensee MDPI, Basel, Switzerland. This article is an open access article distributed under the terms and conditions of the Creative Commons Attribution (CC BY) license (<http://creativecommons.org/licenses/by/4.0/>).

Gas in Scattering Media Absorption Spectroscopy on Small and Large Scales

Towards the Extension of Lung Spectroscopic Monitoring to Adults

Yueyu Lin^{1,2,3}, Patrik Lundin⁴, Emilie Krite Svanberg⁵, Katarina Svanberg^{1,2,6},
Sune Svanberg^{1,2,3*}, and Anna-Lena Sahlberg³⁺

¹National Center for International Research on Green Optoelectronics, South China Normal University, Guangzhou 510006, China

²Guangdong Provincial Key Laboratory of Optical Information Materials and Technology & Center for Optical and Electromagnetic Research, South China Academy of Advanced Optoelectronics, South China Normal University, Guangzhou 510006, China

³Department of Physics, Lund University, SE-221 00 Lund, Sweden

⁴GASPOROX AB, Tellusgatan 13, SE-224 57 Lund, Sweden

⁵Department of Clinical Sciences, Anesthesiology and Intensive Care Medicine, Skåne University Hospital, Lund University, SE-221 00 Lund, Sweden

⁶Department of Clinical Sciences, Oncology and Pathology, Skåne University Hospital, Lund University, SE-221 00 Lund, Sweden

sune.svanberg@fysik.lth.se anna-lena.sahlberg@forbrf.lth.se

Abstract

Numerous natural materials are porous, contain free gas, and are scattering light strongly. Scattering brings about a strong trapping of light and an associated prolonged transit time for photons to reach the detector. Gases can be monitored by using narrow-band laser radiation. We have used the gas in scattering media absorption spectroscopy (GASMAS) method to study free oxygen in thin samples (cm) utilizing a tunable diode laser, while a pulsed dye laser was employed in corresponding measurements on larger samples, up to the meter scale. Time-resolved spectroscopy was in both cases used to assess the temporal distribution of the detected photons, mapping the path-lengths through the media, which ranged between few centimeters up to 100 m. Our work explores the feasibility to extend recent successful monitoring of gases in neonatal infant lungs to the case of larger children or even adults, which could have very important applications,

e.g., in ventilator setting optimization for severely ill patients, suffering, e.g., from SARS-CoV-2. The conclusion of our work is that this could most realistically be performed by applying intra-tracheal illumination employing a tapered amplifier, injected with a distributed feed-back diode-laser oscillator output and combined with wavelength-modulation spectroscopy.

1 Introduction

Monitoring of free gases is of great importance in many different contexts, and laser spectroscopic techniques have proven a great capability for high specificity and sensitivity, as well as for non-intrusive measurement with data available in real-time. Monitoring can be performed locally/*in situ*, or even with remote-sensing techniques. Areas of application include the environmental, industrial and medical fields. Environmental and industrial monitoring can regard constituents, which influence long-term temperature and global change (CO_2 , CH_4 , H_2O ...), the UV protective ozone layer (O_3 , ClO , BrO ...), or pollution emission gases (NO , NO_2 , SO_2 , Hg ...). Physiological gases of medical interest include O_2 , H_2O , CO_2 , CH_4 , and NH_3 . *In situ* monitoring systems frequently take advantage of the practicality and lower costs of semi-conductor tunable lasers, including quantum cascade lasers (see, e.g., [1-5]), while, e.g., combustion research frequently use larger, pulsed systems, which more easily can overcome an inevitable background [6]. Remote-sensing systems, e.g., of the lidar (light detection and ranging) type, could utilize pulsed dye or solid-state lasers or CW semiconductor lasers [7-9].

Gas concentrations are mostly evaluated in absorption spectroscopy, utilizing the Beer-Lambert law, which is readily applicable once the optical path length is known and the absorption cross section is known, or can be eliminated by calibration measurements on known concentrations. This situation frequently pertains in the measurement situations discussed above. However, more recently, it was realized that free gas can also be present and be of substantial interest in cases, when no well-defined absorption path can be defined, but the interrogating light rather propagates diffusely, encounters distributed gas-filled pores or larger cavities, finally to arrive at the detector, located somewhere around the medium. Since the emerging light is weak and non-localized, a large-area detector combined with extremely sensitive detection electronics is needed to pick up the faint gas imprints [10]. This type of spectroscopy, denoted gas in scattering media absorption spectroscopy (GASMAS) has since found a lot of applications in many areas [11,12], regarding, e.g., materials [13-15], pore-size analysis [16-18], food packages [19,20], fruits [21,22], pharmaceuticals [23], and medical diagnostics [5,11].

The medical diagnostics possibilities are of particular importance. GASMAS studies of free gas *in-situ* in organs are clearly different from diagnostics by breath analysis, where the gases are analyzed in a well-defined absorption cell outside the body [24,25]. Human sinus cavities have been extensively studied in relation to rhinosinusitis [26,27], and phantom studies related to middle-ear infection (otitis media) have also been pursued [28]. The activities may have bearing on the handling of the alarming spread of antibiotic resistance [29], in a quest to reduce prescription for infections caused by virus, where the drugs have no effect. A further direction is to use GASMAS for lung monitoring, related to the respiratory distress syndrome (RDS), which is

common in prematurely born infants [30]. Successful feasibility studies have been performed on healthy neonates [31,32]. In a quest to extend the techniques to larger children, or even adults, an approach, where external laser-light chest illumination is replaced by fiber-optical internal light administration, e.g., through an endotracheal tube is proposed to achieve much higher probing light fluxes [33]. The advantages have recently been demonstrated in phantom work [34] and in a study on anesthetized piglets [35].

A long-term goal would be to achieve direct lung monitoring in larger children and also adults to control and optimize the operation of a connected ventilator [33]. In the adult setting, many of the patients treated in Intensive Care Units, suffer from severe respiratory disorders, e.g., pneumonia, chronic obstructive pulmonary disease, lung fibrosis and of course the novel SARS-CoV-2. Direct optical measurements on, e.g., lung volumes and oxygen distribution could lead to prompt detection and treatment of disease progression and complications. The world spread pandemic has brought great challenges to the health care system, with patients displaying symptoms of severe respiratory distress. The natural cause of a severe SARS-CoV-2 infection does not quite resemble well-known states of respiratory failure. In order to properly treat these patients, increased knowledge, e.g., on how lung aeration differs throughout the disease progression is needed.

The present GASMAS work relates to the exploration of the scaling up of dimensions from the cm scale to the meter scale, and evaluate what technological approach would be the most feasible. We have, using two different experimental set-ups, located in Lund, performed monitoring of the gas content in samples of increasing dimensions, as well as studied the temporal distribution of the detected photons following pulsed laser excitation, i.e., mapping the distribution of the total path lengths of the photons diffusing through the sample. For small samples, this was performed using the time-correlated single-photon counting (TCSPC) technique, following ps-pulse laser excitation. The corresponding gas imprint was assessed with a normal GASMAS set-up, operating with a low-power distributed feed-back (DFB) semiconductor laser. The reason for the need of two different set-ups is the fundamental Fourier-transform limitation of spectral resolution in short pulses needed for studies of small samples. Then, two separate arrangements are required, one CW high spectral resolution system for gas assessment, and one pulsed, broadband system for photon propagation studies. In contrast, for large samples, where longer pulses are tolerable, and then providing sufficient spectral resolution, a single system can be used. Then the approach is very similar to differential absorption lidar (DIAL) [8], where exactly that is performed in mapping, e.g., air pollutant concentrations as a function of range. Actually, a remote-sensing study of gas in a strongly scattering material demonstrated exactly that [36], and the application to, e.g., the localization of snow avalanche victims was discussed.

Monitoring of the physiological gas oxygen is clearly of major interest related to lung function assessment. Human tissue, while clearly heavily scattering, has comparatively low absorption around 760 nm, where the molecular oxygen A absorption band is located, exhibiting a number of sharp (half-width < 0.001 nm) rotational-vibrational lines [37]. Unfortunately, the lines are weak. For the strongest line, the R7Q8 component, ~0.44 m of air is needed to produce a 1 percent absorption [37]. A very high sensitivity for minute gas absorption imprints can be

achieved by wavelength-modulation spectroscopy (WMS) using a semiconductor laser, where the lock-in detection is pushed to high-frequencies with associated 1/f noise reduction [38,39]. The use of pulsed lasers strongly reduces the ability to discern small differential absorptions, as is well-known in the lidar community. However, this is then partly compensated by the longer path length through gas in the larger sample, leading to a larger fractional gas imprint, and thus less requirements regarding the signal-to-noise level. Our present study aimed at experimentally elucidating the factors of relevance, to give directions in the construction of an optimum clinically relevant large-scale GASMAS monitoring system. Our measurements were largely performed on oxygen gas in polystyrene foam, where scaling could be adequately studied, and then on organic samples partly simulating a lung, including a 2 kg chicken broiler, with the interior filled with porous sponge, and a small block of polystyrene foam with pork slabs on both sides.

We will describe our experimental arrangements in the next section. Then, in Sect. 3, our measurements and results are presented. In a final section, we discuss our results with special emphasis on possible ways to achieve the final goal of achieving 24-hour continuous lung monitoring in larger children or even adults as an extension of successfully pursued neonatal lung monitoring. The scaling up is not trivial - the higher powers and better signal-to-background advantages in pulsed systems are counter-acted by higher noise levels and resolution limitations due to spectral Fourier-limitation for short pulses, also with associated safety issues. Like-wise, continuous and narrow-band lasers are normally of low power, and penetration depths are limited.

2 Experimental arrangements

In our exploratory work we utilized two different experimental set-ups for the small- and large-scale GASMAS measurements, as motivated in the introduction. The systems are schematically shown in Fig. 1 a)-e).

2.1 Small scale set-up – the GASMAS and TOFS approach

The small-scale instrument, which is manufactured by GASPOROX AB, Sweden, is shown in Fig. 1a), where both the GASMAS and TOFS parts are combined into a single system, named GPX-Porosity, because of its intended use. To the right in the photo the TOFS part with the PMT and the fiber illumination from above is seen. To the left of that the GASMAS part of the instrument is shown (basically a GASPOROX GasSpect) with the laser transmitter unit on the top and the detector below, again illuminating the sample from above and detecting light diffusively transmitted through the sample from below. In the photo, a sample is seen in position for GASMAS measurement, laying on the sample plate, which is moved between a load position (where the sample is put on the sample plate), TOFS measurement and GASMAS measurement by a translation stage. The TOFS and GASMAS measurements are thus performed in succession.

Schematic block diagrams of the GASMAS and TOFS parts of the instrument are seen in Figs 1c) and 1d), respectively. The laser light in both the GASMAS and TOFS parts are made diffuse with a divergence of around 6 degrees (FWHM), by sending the initially collimated beams through diffusers, prior to the sample. The main control unit (MCU) used for both parts is a PC

with a user interface. The detection in the TOFS set-up is based on time correlated single photon counting (TCSPC), using a card installed in the PC. A variable attenuator is used in the TOFS set-up to ensure that photon “pile-up” is avoided.

2.2 Large-scale set-up – the GASMAS/DIAL approach

A schematic of the experimental set-up for the large-scale GASMAS/DIAL approach is shown in Fig. 1e. The second harmonic output of a pulsed Nd:YAG laser (Spectra Physics, PRO 290-10, 10 Hz) was used to pump a narrow-band dye laser (Sirah, PRSC-D-18, operated with the dye LDS765), in order to generate tunable laser radiation around 760 nm and with a pulse duration of 6-8 ns. The pulse energies used in these experiments range from 2-60 mJ, depending on the size of the samples. The main laser beam was directed to the porous sample. The light scattered through the sample was detected with a photomultiplier tube (PMT), while a small part of the laser beam was split off onto a photodiode (PD), and the signals from the PD and PMT were displayed on an oscilloscope (LeCroy, Waverunner 6100). The photodiode signal was used both as a trigger for the oscilloscope, and as a reference point for the shape and timing of the incident laser pulse. To filter away surrounding background light, the PMT was equipped with an interference filter (750 ± 20 nm), which transmitted the 760 nm light but blocked most of the ambient light and the stray light from the Nd:YAG laser.

The sample in these measurements were either blocks of polystyrene foam, of dimension 40×60 cm with different thickness, or a chicken broiler/pork slab as described later in connection with Fig. 6. The polystyrene foam is seen to the left in the photo in Fig. 1b. To avoid interference from light scattering in the room, the block was shielded with black plastic during the measurements. An oscilloscope screen dump is also shown in Fig. 1b, with the trigger ($t=0$) signal (violet), a photon time-of-flight graph (green) and a repetitive wavelength scan through the oxygen line (yellow). Due to the interface between oscilloscope and PMT, the green signal trace is shown as a negative signal, and the absorption lines (yellow) are shown as peaks in the yellow spectrum. The sharp lines between each yellow absorption peak marks the start of each repetitive scan over the R9R9 O₂ line, which was chosen for our study.

3 Measurements and results

Our measurements were all intended to be exploratory in view of extending neonatal lung monitoring towards larger children and adults. Lung tissue is quite porous containing small alveoli as well as channels of different dimensions pertaining to the bronchial tree. Initial measurements we performed with both experimental set-ups in studies of strongly scattering structures, while a final measurement series approached a more realistic phantom situation, with sponges inserted in the interior of a large chicken broiler, or a small block of polystyrene foam surrounded with slabs of pork.

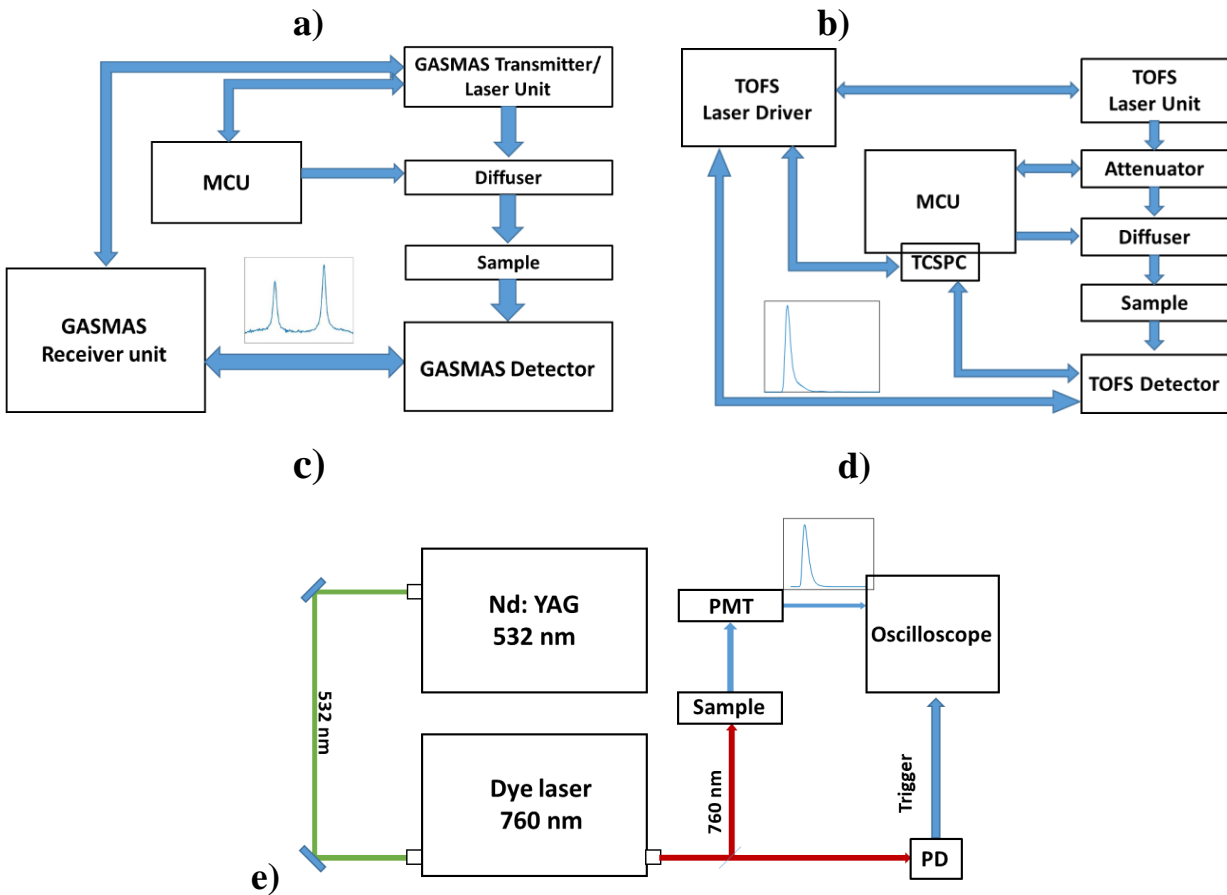
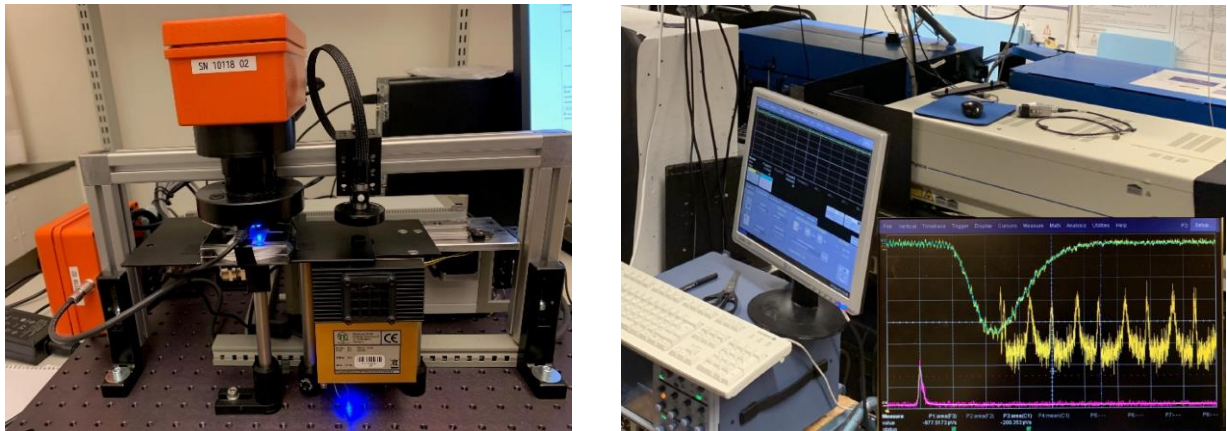


Fig. 1 Experimental set-ups used in the measurements. a) Photo of the small-scale set-up with the Gasmas arrangement to the left and the time-of-flight arrangement to the right b) Photo of the large-scale set-up with the Nd-YAG laser pumping a dye laser and the polystyrene block (to the left). An oscilloscope screen dump is inserted, with the trigger ($t=0$) signal (violet), a time-of-flight graph (green) and a repetitive wavelength scan through the oxygen line (yellow) c) Schematic diagram of the diode laser-based Gasmas set-up (MCU denotes the main control unit, a PC) d) Schematic diagram of the pulsed diode laser time-of-flight set-up (TOFS denotes time-of-flight spectroscopy), and e) Schematic diagram of the pulsed DIAL-Gasmas system (PMT denotes photomultiplier tube, and PD photo diode).

3.1 Small-scale GASMAS and TOFS set-up recordings

The GASMAS technique using a low-power tunable semiconductor laser is very suited for monitoring weak absorptive imprints due to gas in scattering media of small extension. We studied a 10 mm thick slab of polystyrene foam of the same type that we later used for pulsed laser studies. We show in Fig. 2.a) the imprint from two molecular oxygen lines, the R11Q12 and R13R13 components, at 13150.2 and 13151.4 cm^{-1} , respectively. By calibration, we notice that the absorptive imprint corresponds to an effective path length through air of 16 cm. The remaining oxygen imprint due to the 35 mm open air path between the laser and the detector is removed from that value. The residual oxygen curve can be seen superimposed on an undulating background, which we interpret as due to interference fringes between partially reflecting surfaces in the set-up. The removal of such fringes is frequently an important issue in tunable diode laser spectroscopy and has been discussed in several publications; see, e.g., [40-43]. A time-of-flight recording on the same polystyrene slab is shown in Fig. 2.b). We note, that the maximum of the distribution of arrival times is delayed by about 0.7 ns, corresponding to 15-20 cm average passage length divided up between air, and polystyrene. Thus, the data from the frequency and time domain are compatible.

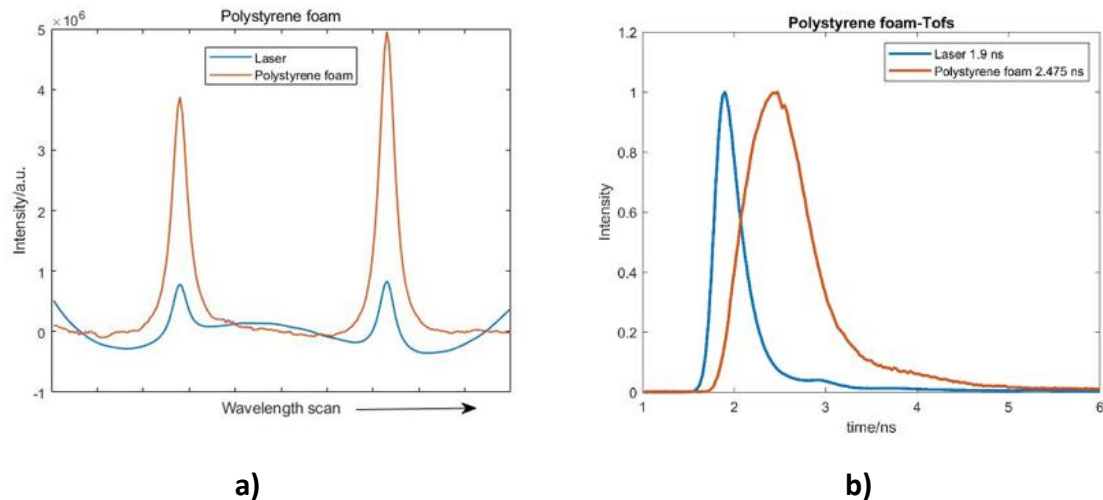


Fig. 2. a) GASMAS recording (direct absorption) through a 1.0 cm thick slab of polystyrene foam (orange curve) and residual oxygen recording with the sample removed (blue curve). b) Time-of-flight recording for the same slab of polystyrene foam (orange curve) and instrument response function (blue curve).

As a further small-scale GASMAS example we show in Fig. 3 the case of an increasing number of cosmetic cotton pads placed in a transparent plastic box, with 17 mm height inside. Five or ten pads all fill up the space, but with increasing compression of the fiber material. Fig. 3a) shows the TOF recordings and Fig. 3b) the resulting oxygen absorption signals. We notice, that the TOF curves display increasing effective photon path lengths due to increased scattering (some photons finally travelled more than 100 cm) at the same time as the oxygen absorption increases. However, gas absorption increases due to a longer path length through gas could be partly counteracted by photons also increasingly travelling inside cotton fibres, which become more and more compressed and thus contacted to each other.

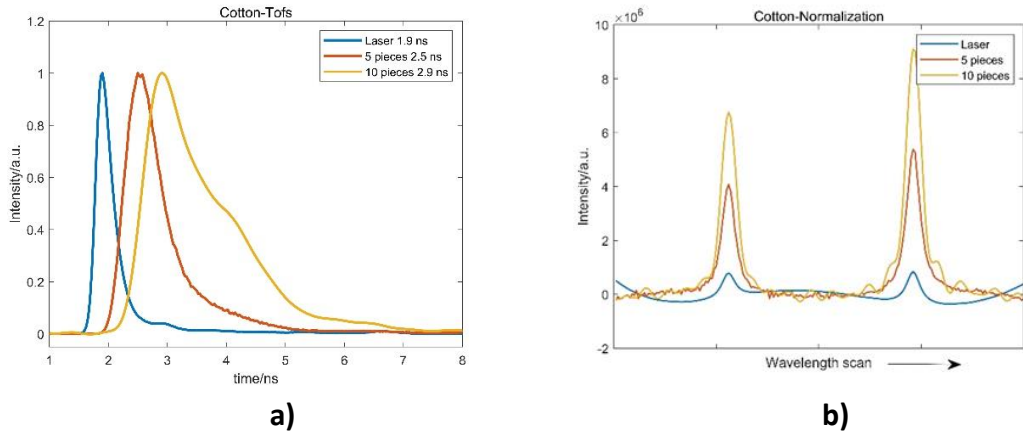


Fig. 3. Time-of-flight recordings a) and corresponding oxygen GASMAS recordings for cotton pads, placed in a transparent plastic box of inner height 17 mm. Recordings for 5 and 10 pads, compressed to increasing degrees are shown. Recordings for an empty box are also included (blue curves).

Similar recordings are shown in Figs 4a) and b) for a more biological case. Here 1 – 4 yellowish quite porous crackers were studied. The interrogation distance was matched to the resulting total thickness. We also here see the residual oxygen signal (blue curve) for the case of no sample also showing an oscillating background due to interference fringes, which are clearly more likely in the case of the absence of a scattering medium.

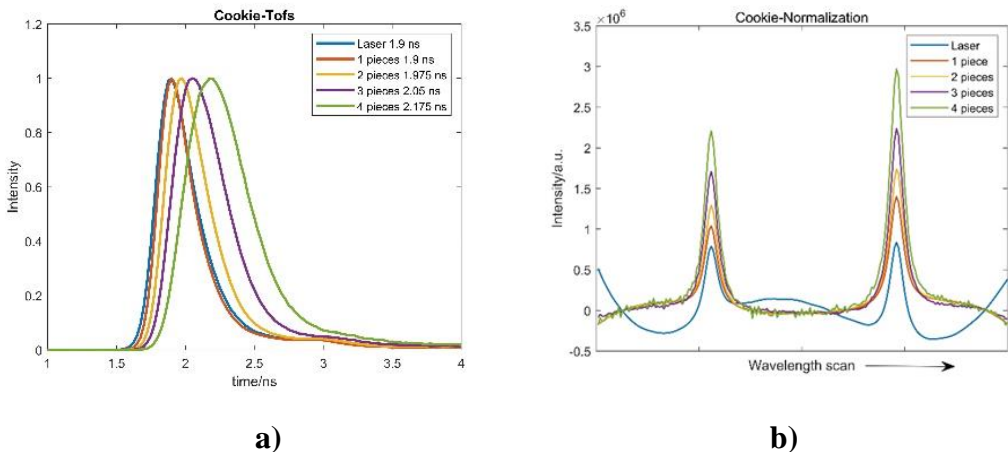


Fig. 4. Time-of-flight recordings a) and corresponding oxygen GASMAS curves b) for 4 mm thick yellowish and very porous crackers. Recordings for 1, 2, 3, and 4 crackers placed on top of each other are shown, as well as the recordings with no cracker in place (blue curves).

3.2 Large-scale GASMAS/DIAL set-up recordings

As earlier discussed, for larger samples time-resolved recordings are compatible with range-resolved gas concentration recordings as applied in normal atmospheric differential absorption lidar (DIAL) air pollution monitoring. We will in this section present results from our pulsed narrow-band dye laser set-up. The approach could then be characterized as small-scale DIAL, or as large-scale GASMAS. We first performed measurements on large blocks of polystyrene foam of the same kind as used in the small-scale GASMAS measurements shown in Fig. 2. Time-resolved recordings with the laser tuned off the oxygen absorption line are shown in Fig. 5a) for 10, 20, 30, 40, and 60 cm of polystyrene. The average path length travelled by the photons in the sample strongly increases, and for the thickest block we notice that some photons travel over 100 meters before reaching the detector. The recordings were made by adding rectangular blocks of size $40 \times 60 \times 10$ cm back-to-back and placing the detector on the backside opposite the light injection point. For the 40 cm thickness, one recording was made by stacking four $40 \times 60 \times 10$ cm blocks together, and another one was made by using a whole $40 \times 60 \times 80$ cm block, aligned so the detector was placed opposite the light injection through 40 cm polystyrene foam. We note, that both arrangements resulted in very similar recordings, indicating that the optical contact between individual, very flat blocks was very good. The 60 cm recording was made with the same whole block but aligned so the detector was opposite the light injection point through 60 cm polystyrene foam.

Time/range-resolved differential absorption recording yielding range-resolved concentration data could be obtained by first positioning the laser wavelength on an oxygen absorption line (the R9R9 line at 13144.5 cm^{-1}) and reference it to a close-by off-resonance wavelength. A repetitive wavelength sweep through the line is shown as the yellow trace on the computer screen in Fig. 1b). Data for a 40 cm thick polystyrene foam block are shown in Fig. 5b), together with the divided, DIAL curve for on and off-resonance recordings. A clear slope for increasing time delays/path-lengths is observed corresponding to the 21 percent oxygen content in

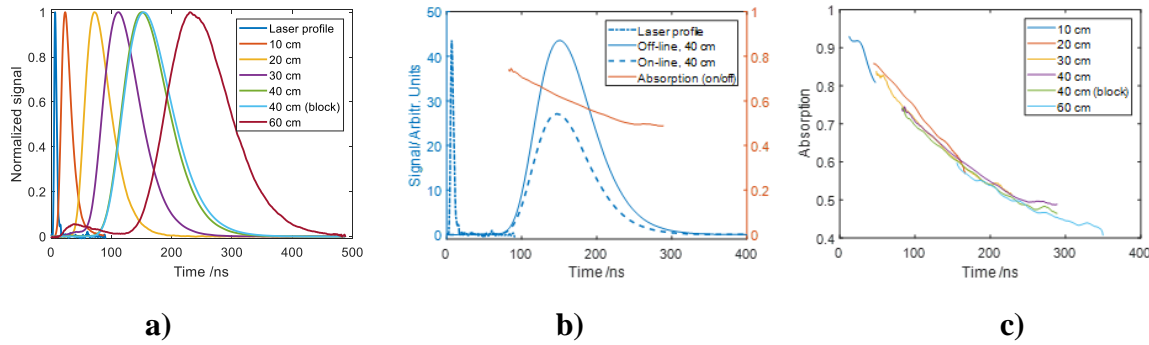


Fig. 5 a) Time-resolved recordings for polystyrene blocks of thickness 10-60 cm. The laser pulse recording, in the absence of a scattering medium is also included (blue curve) b) on- and off-resonance temporal recordings for a 40 cm thick block of polystyrene foam, as well as the ratio DIAL curve. c) ratio curves for polystyrene foam blocks of thickness 10 - 60 cm.

the atmospheric gas inside the material pores. We note, that the oxygen absorption over 30 meters of gas is about 25 percent. Corresponding DIAL curves for all block thicknesses are shown in Fig. 5c). The curves closely overlap in the regions where photons can be detected, and the slope follows an exponential, as expected for a constant oxygen concentration, as a reflection of the simple Beer-Lambert law.

Since the possibilities and limitations in medical diagnostics using CW GASMAS systems operating with semiconductor lasers with few mW output are well known, we here wanted to explore what type of upscaling might be achieved using a high-peak power pulsed laser system on the kind typically used in DIAL measurements. We thus exchanged the polystyrene blocks for easily available animal food-stuff samples and pursued exploratory test recordings. Fig. 6a) shows a 2 kg chicken broiler, where house-hold sponges (total thickness about ~6 cm) were introduced in the interior of the broiler, while Fig. 6b) shows a 3 cm thick piece of polystyrene foam surrounded by ~2 cm thick pork slabs on each side.



a)

b)

Fig. 6 a) Photo of chicken broiler, into which sponges were introduced. b) Photo of sample arrangement with a block of polystyrene foam and pork slabs positioned on each side.

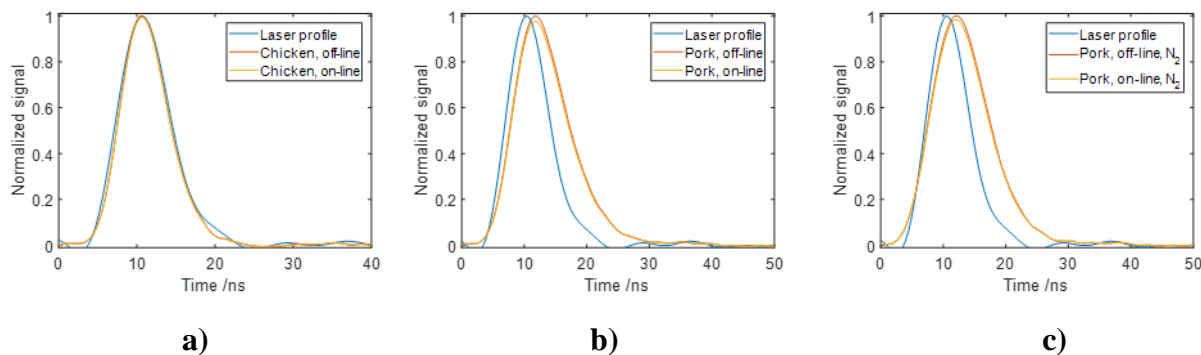


Fig. 7 a) Time-resolved recordings through the chicken broiler (on and off the oxygen line) as well as the laser pulse shape only. b) and c) Time-resolved recordings through the composite polystyrene foam/pork slab sample; on and off the oxygen absorption line. b) corresponds to ambient air recording, while in c) nitrogen flushing was applied.

Examples of time-resolved recordings for these samples are shown in Fig. 7. a) presents data for the chicken broiler with internal air-filled sponges. A delay of <0.1 ns is observed between the peak intensities of the curves with and without the 15 cm thick sample. No clear differential absorption effect is observed for the resulting short pathway through the sponges, and there is no significant broadening of the temporal curve. We note, that the temporal curve is broadened by <0.1 ns. Panels b) and c) show data for the polystyrene foam/pork composite target studied in ambient air, and with the whole sample flooded with nitrogen gas, respectively. In this case, the delay of the peak is observed to be 1.5 ns, and the temporal distribution is increased by 2 ns, larger values than for the broiler, indicating a longer effective path length through the composite sample, most likely due to the foam component. This is consistent with the observation of a small additional reduction in peak intensity for the on-resonance wavelength in the case of ambient air monitoring, apart from a larger reduction due to surrounding ambient air. Divided, range-resolved DIAL curves make little sense in this case when the recorded signal is heavily convoluted with the laser pulse itself. Clearly, a very high sensitivity to small trigger errors will also pertain for these cases, and actually, occasional recordings of erratic data are believed to be due to such problems. While such problems should be reduced when the sample linear size would be increased by a factor of two, pertaining to the larger children/adult lung case, there are clear issues with the high-energy pulsed laser approach.

4 Discussion and conclusions

Before drawing the conclusions on the technical implications of the present work and earlier experience, what regards the development of a system for adult lung monitoring, we present a background regarding the need for such surveillance.

We note that lung oxygen measurements in adults using GASMAS has so far not been possible, due to longer path-lengths/larger geometries, leading to extremely low light intensities reaching the detector, as compared to the successful measurements on neonatal lungs, previously reported by our research group [31,32]. The possibility to promptly identify severe lung complications, e.g., pneumothorax (collapsed lung due to air leakage in the space between the lung and the chest wall) or atelectasis (collapsed lung due to deflated alveoli), using the GASMAS technique in an animal model has also been demonstrated [35]. The need for a non-invasive, harmless, continuous lung surveillance technique for preterm/ill infants is clear, where, due to lung immaturity, careful monitoring of the spatially distributed oxygen content and the amount of air-filled alveoli, as well as detection of complications, such as pneumothorax or atelectasis, can lead to optimal respiratory support and prompt treatment of complications.

There is, of course, a corresponding need for adults, where many of the sick patients suffer from severe respiratory disorders, e.g., pneumonia, chronic obstructive pulmonary disease, idiopathic lung fibrosis, and of course the novel SARS-CoV-2 viral infection [44-46].

The worldwide spread of the SARS-CoV-19-virus has had enormous medical, social and economic impact. In modern time, this is the worst pandemic observed. Manifestations of infection vary much; from no symptoms, to mild upper respiratory symptoms, respiratory symptoms that

require hospitalization without intensive care, and finally severe respiratory failure in need of ventilator therapy, renal and cardiovascular support in the intensive care unit. Recent studies show, that once hospitalized, approximately 25% of the patients require mechanical ventilation, advanced circulatory support, and/or renal replacement therapy [47]. The case fatality rate is extremely age dependent with an increase from <0.6 to 2.2% at age 60 and increasing to 9.3 % at age 80 [48].

The ability to monitor dynamic changes regarding the air and oxygen distribution, as well as prompt detection of anomalies would certainly improve the medical treatment of these patients. The patients, who are in need of ventilator support due to SARS-CoV-2 infection, present symptoms like shortness-of-breath, severe hypoxia, and respiratory fatigue, often together with high fever and reduced general condition. The severe respiratory deterioration often emerges around one week after initial SARS-CoV-2 symptoms occur. The condition presents itself as a pneumonitis, with dysregulation of the pulmonary perfusion, loss of pulmonary vasoconstriction (a normal physiological mechanism, reducing the blood perfusion in less ventilated lung regions, avoiding shunting of deoxygenated blood through the lungs), and micro-embolism (small thrombi in the pulmonary vessel system, leading to increased dead-space ventilation). The lung compliance is still maintained and ventilator-assisted recruitment of collapsed alveoli is possible. With disease progression, a more classical ARDS (Acute Respiratory Distress Syndrome) status arises – consisting of pulmonary edema, inflammation and consolidated lung regions [49]. The lungs are now “stiffer”, and high airway pressures in the ventilator is required to oxygenate the patient and to remove the carbon dioxide. During this phase, pulmonary embolism, a well-known complication to severe SARS-CoV-19 infection, further deteriorates the respiratory function.

The possibility for bed-side continuous monitoring of the dynamic pulmonary processes, with regard to oxygen content, spatial air distribution and also detection of severe complication, such as pneumothorax (collapsed lung) and atelectasis (collapsed alveoli), could lead to quicker detection and treatment of immediate life-threatening conditions. There would be a possibility to “tailor” the respiratory support for the individual patients, with regard to in which phase of the disease progression they are.

In scaling up lung monitoring from newborn to larger children or adults, internal light administration is clearly advantageous over light injection from the surface of the chest [33-35]. Internal fiber-optical light administration would not present any major complication, since the patients mostly in need would anyway be intubated with an endotracheal tube, connected to a ventilator. Clearly, high laser intensity in repetitive pulses would allow signal photons to be better distinguished over background noise as compared to the situation if the same average power would be delivered from a CW laser source. However, as illustrated in our measurements and in the general lidar community, when the absorption imprint is a very small fraction (< 1%) of the detected light, pulse to pulse fluctuations and other error sources make the detection uncertain. Also, short energetic pulses, like the <10 ns dye laser pulses used in the present experiments, are difficult to transmit through an optical fiber, and the tissue exposure safety regulations would be hard to meet. Then the longer pulses (>100 ns) from a tunable alexandrite laser, which operates in the spectral region of interest, would be a possibility for fiber-optical transmission and lower tissue load, as earlier utilized for inducing fluorescence in a clinical endoscopic imaging system [50].

The potential for range-resolved monitoring would then be lost due to the longer pulse length. Further, such a laser system is very bulky and complex, which would reduce the applicability.

High-frequency lock-in detection employing a modulated CW system has a very strong noise suppression capability. While originally an analogous electronic signal processing method, it can very conveniently be adopted in a powerful digital approach [39], which allows very small fractional absorptive imprints in a weak detected signal level to be isolated, as illustrated, e.g., in numerous GASMAS applications. The equipment used so far had only output powers of typically 10 mW or less, and would not allow the scaling up of size, even if intra-tracheal illumination would be applied. However, recently diode-laser-pumped solid-state tapered amplifiers have become available, and would be able to boost the presently used GASMAS laser outputs (including its modulation employed for sensitive WMS detection) hundred-fold or more, while basically retaining the rest of the full system. A diffusing fibre termination or specially adopted endotracheal tube would ensure a well tolerable power level. The experimental work presented in this paper, and the analysis done, convince us that this would be the way to proceed to accomplish 24-hour bedside lung surveillance with active feedback to the ventilator. We now plan to construct such a system and test its performance. Our hope is that a successful development would much benefit severely ill patients, including those affected by SARS-CoV-2 and future pandemics with lung impairment.

Acknowledgements

We are grateful for discussions and support by J. Bood and Z.S. Li of the Physics Department, Lund University, and by M. Lewander Xu and M. Sebesta, GASPOROX AB, as well as by Prof. G.F. Zhou, South China Normal University.

Conflict of interest statement: PL is employed by GASPOROX AB, which manufactured the small-scale equipment, and KS and SS have minor shares in this company. EKS, KS and SS are minor share-holders in the company GPX Medical AB, which pursues lung monitoring of neonatal infants; KS is also a board member of that company.

References

1. P. Werle, F. D'Amato, S. Viciani, Tunable Diode Laser Spectroscopy: Principles, Performance and Perspectives, in *Lasers in Chemistry*, ed. M. Lackner (Wiley-VCH, Weinheim, 2008).
2. J. Hodgkinson, R.P. Tatam, Optical Gas Sensing: A Review, *Meas. Sci. Technol.*, **24**, 012004 (2013).
3. A. Kosterev, G. Wysocki, Y. Bakhirkin, S. So, R. Lewicki, M. Fraser, F. Tittel, R.F. Curl, Application of Quantum Cascade Lasers to Trace Gas Analysis, *Appl. Phys. B* **90**, 165–176 (2008).
4. A. Schwaighofer, M. Brandstetter, B. Lendl, Quantum Cascade Lasers (QCLs) in Biomedical Spectroscopy, *Chem. Soc. Rev.*, **46**, 5903 /2017)

-
5. K. Svanberg, S. Svanberg, Monitoring of Free Gas In-Situ for Medical Diagnostics using Laser Spectroscopic Techniques, in *Frontiers in Biophotonics for Translational Medicine*, eds. U.S. Dimish, M. Olivo, Springer, Singapore, 307–321, 2015.
 6. K. Kohse-Höinghaus, R.S. Barlow, M. Aldén, J. Wolfrum, Combustion at the Focus: Laser Diagnostics and Control, Proc. Comb. Inst. **30**, 89-123 (2005).
 7. W. Demtröder, S. Svanberg, Optical and Spectroscopic Techniques, in *Springer Handbook of Lasers and Optics*, ed. by F. Träger (Springer, Heidelberg, 2007), pp. 987–1052
 8. S. Svanberg, Differential absorption LIDAR (DIAL), in *Air Monitoring by Spectroscopic Techniques*, ed. by M. Sigrist (Wiley, NewYork, 1994), Chap. 3
 9. M. Brydegaard, S. Svanberg, Photonic Monitoring of Atmospheric and Aquatic Fauna, Lasers and Photonics Review, DOI: 10.1002/lpor.201800135 (2018).
 10. M. Sjöholm, G. Somesfalean, J. Alnis, S. Andersson-Engels, S. Svanberg, Analysis of Gas Dispersed in Scattering Solids and Liquids. Opt. Lett. **26**, 16 (2001)
 11. S. Svanberg, Gas in Scattering Media Absorption Spectroscopy – from Basic Studies to Medical Applications, Laser. Photon. Rev. **7**, 779 (2013).
 12. S. Svanberg, Gas in Scattering Media Absorption Spectroscopy, in *Encyclopedia of Analytical Chemistry* (Wiley, 2019) DOI: 10.1002/9780470027318.a9325.pub2201
 13. H. Zhang and S. Svanberg, Laser Spectroscopic Studies of Gas Diffusion in Alumina Ceramics, Optics Express **24**, 1986 (2016)
 14. L. Yang, G. Somesfalean, S. He, Laser Absorption Spectroscopy of Oxygen Confined in Highly Porous Hollow Sphere Xerogel, Opt. Express **22**, 2584 (2014).
 15. Q. Libois, F. Levesque-Desrosiers, S. Lambert-Girard, S. Thibault, F. Domine, Optical Porosimetry of Weakly Absorbing Porous Materials, Opt. Express **27**, 22983 (2019).
 16. T. Svensson, M. Lewander, S. Svanberg, Laser Absorption Spectroscopy of Water Vapor Confined in Nanoporous Alumina: Wall Collision Line Broadening and Gas Diffusion Dynamics, Opt. Express **18**, 146460 (2010).
 17. C.T. Xu, M. Lewander, S. Andersson-Engels, E. Adolfsson, T. Svensson, S. Svanberg, Wall Collision Line Broadening at Reduced Pressures: Towards Nondestructive Characterization of Nanoporous Materials, Phys. Rev. A **84**, 042705 (2011).
 18. A. Al-Saudi, A. Aljalal, W. Al-Basheer, K. Gasmi, S. Qari, Investigation of O₂ line Broadening in Nanoporous Alumina using Gas in Scattering Media Absorption Spectroscopy, Appl. Phys. B **126**, 63 (2020).
 19. M. Lewander, Z.G. Guan, L. Persson, A. Olsson, S. Svanberg, Food Monitoring Based on Diode Laser Gas Spectroscopy, Appl. Phys. B **93**, 619 (2008).
 20. T.Q. Li, H.Y. Lin, H. Zhang, K. Svanberg, S. Svanberg, Application of Tunable Diode Laser Spectroscopy in Assessment of Food Quality, Appl. Spectrosc. **71**, 929 (2017).
 21. L. Persson, H. Gao, M. Sjöholm, S. Svanberg, Diode Laser Absorption Spectroscopy Studies of Gas Exchange in Fruits, Laser Opt. Eng., **44**, 687 (2006).
 22. J. Huang, H. Zhang, H.Y. Lin, T.Q. Li, L. Mei, K. Svanberg, and S. Svanberg, Gas Exchange in Fruits Related to Skin Condition and Fruit Ripening, J. Biomed. Opt. **21** (12), 127007 (2016); doi: 10.1117/1.JBO.21.12.127007
 23. T. Svensson, L. Persson, M. Andersson, S. Svanberg, S. Andersson-Engels, J. Johansson, S. Folestad, Noninvasive Characterization of Pharmaceutical Solids by Diode Laser Oxygen Spectroscopy. Appl. Spectrosc. **61**, 784 (2007)

-
24. M. Lewander, S. Lindberg, T. Svensson, R. Siemund, K. Svanberg, S. Svanberg, Noninvasive Diagnostics of the Maxillary and Frontal Sinuses based on Diode Laser Gas Spectroscopy, *Rhinology* **50**, 28-32 (2012)
25. M.R. McCurdy, Y. Bakhirkin, G. Wysocki, R. Lewicki, F.K. Tittel, Recent Advances of Laser-Spectroscopy-Based Techniques for Applications in Breath Analysis. *J. Breath Res.* **1**, 014001/1-12 (2007).
26. C. Wang, P. Sahay, Breath Analysis using Laser Spectroscopic Techniques: Breath Biomarkers, Spectral Fingerprints, and Detection Limits. *Sensors* **9**, 8230 (2009)
27. J. Huang, H. Zhang, T.Q. Li, H.Y. Lin, K. Svanberg, S. Svanberg, Assessment of Human Sinus Cavity Air Volume using Tunable Diode Laser Spectroscopy, with Application to Sinusitis Diagnostics, *J. Biophotonics* **8**, 985 (2015)
28. L.N. Hu, W.S. Li, H.Y. Lin, Y. Li, H. Zhang, K. Svanberg, S. Svanberg, Towards an Optical Diagnostic System for Otitis Media using a Combination of Otoscopy and Spectroscopy, *J. Biophotonics*, Doi.org/10.1002/jbio.201800305 (2019).
29. H. Goossens, M. Ferech, R. van der Stichele, M. Elseviers, ESAC Project Group. Outpatient Antibiotic use in Europe and Association with Resistance: A Cross-national Database Study, *Lancet* **365**, 579 (2005).
30. L.B. Ware, M.A. Matthay, Medical Progress – The Acute Respiratory Distress Syndrome, *New Engl. J. Med.* **342**, 1334–1349 (2000).
31. P. Lundin, E. Krite Svanberg, L. Cocola, M. Lewander Xu, G. Somesfalean, S. Andersson-Engels, J. Jahr, V. Fellman, K. Svanberg, S. Svanberg, Non-invasive Monitoring of Gas in the Lungs and Intestines of Newborn Infants using Diode Lasers: Feasibility Study, *J. Biomed. Opt.* **18**, 127005 (2013).
32. E. Krite Svanberg, P. Lundin, M. Larsson, J. Åkesson, K. Svanberg, S. Svanberg, S. Andersson-Engels, V. Fellman, Noninvasive Monitoring of Oxygen in the Lungs of Newborn Infants by Diode Laser Spectroscopy, *Pediatr. Res.* **79**, 621 (2016).
33. E. Krite Svanberg, S. Svanberg, Equipment and Method for Internal Laser Illumination for Medical Gas Analysis, Swedish Patent Application No 1500335-3. 2015.
34. J. Larsson, D. Leander, M. Lewander Xu, V. Fellman, J. Bood, E. Krite Svanberg, Comparison of Dermal vs Internal Light Administration in Human Lungs using the TDLAS-GASMAS Techniques – Phantom Studies, *J. Biophotonics* DOI: 10.1002/jbio.201800350 (2019).
35. E. Krite Svanberg, J. Larsson, M. Rasmussen, M. Larsson, D. Leander, S. Bergsten, J. Bood, G. Greisen, V. Fellman, Changes in Pulmonary Oxygen Content are Detectable with Laser Absorption Spectroscopy – Proof of Concept in Newborn Piglets, *Pediatric Research*, Doi 10.1038/s41390-020-0971-x (2020).
36. Z.G. Guan, M. Lewander, R. Grönlund, H. Lundberg, S. Svanberg, Gas Analysis in Remote Scattering Targets using LIDAR Techniques, *Appl. Phys. B* **93**, 657 (2008)
37. I. E. Gordon, L. S. Rothman, *et al.*, The HITRAN2016 Molecular Spectroscopic Database, *J. Quant. Spectr. Rad. Trans.* **203**, 3 (2017).
38. E.I. Moses, C.L. Tang, High-Sensitivity Laser Wavelength-Modulation Spectroscopy, *Opt. Lett.* **1**, 115–117 (1977).

-
39. L. Mei, S. Svanberg, Wavelength Modulation Spectroscopy – Digital Detection of Gas Absorption Harmonics based on Fourier Analysis, *Applied Optics* **54**, 2254 (2015)
40. V.V. Liger, Optical Fringes Reduction in Ultrasensitive Diode Laser Absorption Spectroscopy, *Spectrochimica Acta A* **55**, 2021-2026 (1999).
41. L. Persson, M. Andersson, F. Andersson, S. Svanberg, Approach to Optical Interference Fringe Reduction in Diode-Laser-Based Absorption Spectroscopy, *Appl. Phys. B* **87**, 523 (2007)
42. P. Lundin, M. Karlsson, L. Mei, J. Larsson, G Somesfalean, S. Svanberg. Sensitivity Enhancement and Fringe Reduction in Tunable Diode Laser Spectroscopy using Hemispherical Diffusers, *Rev. Sci. Instr.* **88**, 10.1063/1.4983807 (2017)
43. R. Yang, X.Z. Dong, Y.F. Bi, T.L. Lv, A Method of Reducing Background Fluctuation in Tunable Diode Laser Absorption Spectroscopy, *Opt. Commun.* **410**, 782-786 (2018).
44. J.L. Vincent, Y. Sakr, V.M. Ranieri, Epidemiology and Outcome of Acute Respiratory Failure in Intensive Care Unit Patients, *Critical Care Medicine* **31** (4 Suppl), 296-9 (2003).
45. G. Bellani, J.G. Laffey, T. Pham, et al. Epidemiology, Patterns of Care, and Mortality for Patients with Acute Respiratory Distress Syndrome in Intensive Care Units in 50 Countries. *JAMA* **315** (8):788-800 (2016).
46. P. Jason, W. Li, L. Ling, et al. Intensive Care Management of Coronavirus Disease 2019 (COVID-19): Challenges and Recommendations. *Lancet Respir. Med.* **8**, 506–17 (2020).
47. P.A. McCullough, R.J. Kelly, G. Roucco, et al., Pathophysiological Basis and Rationale for Early Outpatient Treatment of SARS-CoV-2 (Covid-19) Infection, *Am. J. Medicine* **134**, 16 (2020).
48. N. Ferguson, D. Laydon, G. Nedjati Gilani, et al., Report 9: Impact of Non-pharmaceutical Interventions (NPIs) to Reduce COVID19 Mortality and Healthcare Demand, Imperial College London, 16 March 2020. <https://doi.org/10.25561/77482>.
49. A.Y. Denault, S. Delisle, D. Carty, et al., A Proposed Lung Ultrasound and Phenotypic Algorithm for the Care of COVID-19 Patients with Acute Respiratory Failure, *Can. J. Anesth.* **67**, 1393 (2020).
50. K. Svanberg, I. Wang, S. Colleen, I. Idvall, C. Ingvar, R. Rydell, D. Jocham, H. Diddens, S. Bown, G. Gregory, S. Montán, S. Andersson-Engels, and S. Svanberg, Clinical Multi-colour Fluorescence Imaging of Malignant Tumours - Initial Experience. *Acta Radiol.* **38**, 2 (1998).

Article

Gas Monitoring in Human Frontal Sinuses -

Stability Considerations and Gas Exchange Studies

Han Zhang^{1,2*}, Ning Han^{1,2*}, Yueyu Lin^{1,2}, Jiawen Huang^{1,2}, Sune Svanberg^{1,2,3+} and Katarina Svanberg^{1,2,3+}

- ¹ National Center for International Research on Green Optoelectronics, South China Normal University, Guangzhou 510006, China
² Guangdong Provincial Key Laboratory of Optical Information Materials and Technology & Center for Optical and Electromagnetic Research, South China Academy of Advanced Optoelectronics, South China Normal University, Guangzhou 510006, China
³ Lund Laser Centre, Lund University, SE-221 00 Lund, Sweden
* These authors contributed equally to this study
+ Correspondence: sune.svanberg@fysik.lth.se; katarina.svanberg@med.lu.se

Abstract: Acute rhinosinusitis is a common infectious disease, which in more than 90% of the cases is caused by viruses rather than by bacteria. Even so, antibiotics are often unnecessarily prescribed, and in the long run contributing to the alarming antibiotics resistance. The reason is that there are no good guiding tools defining the background reason of the infection. One main aspect for the clearance of the infection is if there is a non-obstructed ventilation through the existing channels. Gas in Scattering Media Absorption Spectroscopy (GASMAS) seems to have the potential of diagnosing this. We have performed a study of frontal sinuses of volunteers with a focus on signal reproducibility over time, accurate oxygen concentration determination, and assessment of gas transport through the channels, naturally and after decongestant spray administration. Different from earlier studies on frontal sinuses, water vapor, serving the purpose of oxygen signal normalization, was measured at 818 nm rather than earlier at 937 nm, now closer to the 760 nm oxygen absorption band and thus resulting in more reliable results. Also the action of decongestants was objectively demonstrated for the first time.

Citation: Zhang, H.; Han, N.; Lin, Y.; Huang, J.; Svanberg, S.; Svanberg, K.; Gas Monitoring in Human Frontal Sinuses—Stability Considerations and Gas Exchange Studies. *Sensors* **2021**, *21*, x. <https://doi.org/10.3390/xxxxx>

Academic Editor: Firstname Lastname

Received: date

Accepted: date

Published: date

Publisher's Note: MDPI stays neutral with regard to jurisdictional claims in published maps and institutional affiliations.



Copyright: © 2021 by the authors. Submitted for possible open access publication under the terms and conditions of the Creative Commons Attribution (CC BY) license (<http://creativecommons.org/licenses/by/4.0/>).

1. Introduction

1.1 Background

Rhinosinusitis is a common upper respiratory tract infectious disease caused by viruses, bacteria, or more seldom by fungus. The main symptoms are nasal congestion, nasal discharges, headache, and fever, which seriously affect the daily life of patients. Sinusitis is a very common infection that occurs all over the world and is a major public health problem. It is the fifth most common infectious diagnosis in open-patient healthcare, affecting about 16% of the United States population each year [1]. Over time, the prevalence of sinusitis has been on the rise due to increased pollution and antibiotic resistance. According to one U. S. official report, chronic sinusitis is the most common chronic disease among people less than 45 years old, and the second most common chronic disease among people between 45 and 65 years, only outnumbered by hypertension [2]. However, this disease is easily neglected in children, and the incidence of sinusitis in children is even higher than that in adults, and may be as high as 32% in young children [3]. Rhinosinusitis imposes a huge clinical and economic burden and affects the quality of life of a large fraction of the population. In 1992, the healthcare sector in the U.S. spent more than \$2 billion

on sinusitis medication [4]. In 1996, the total cost of medical care due to sinusitis was estimated at \$5.8 billion, out of which \$1.8 billion (30.6%) was spent on children 12 years of age or younger. This cost estimate does not include lost time for work, and lost productivity [5-7].

The sinuses, which surround the nasal cavity, are gas-filled cavities located in the facial bones and the skull. The mucosa of the nasal cavity continues into the sinuses. This explains why infection of the nasal cavity can cause infection of the sinuses [8]. There are four pairs of paranasal sinuses: the maxillary, the frontal, the ethmoid, and the sphenoid ones, as shown in Figure 1 [9]. They are air-filled, mucosa-lined cavities within the maxillofacial region and skull, and all are communicating with the nasal cavity [10,11]. Sinuses are divided into two groups according to their anatomical location and the opening locations of the sinus connecting channels (the *ostia*). The anterior sinuses are the frontal and the maxillary cavities, all with openings to the middle nasal passage [10,11]. The posterior group of sinuses consists of the sphenoid and the ethmoid sinuses. The former ones open in the sphenoid recess and the latter ones open in the upper nasal passage. The maxillary sinuses are the largest ones [10]. The average volume of the adult maxillary sinus is 10 - 15 ml. The ethmoid sinus is a honeycomb-like structure, within the ethmoid bone, and consists of 3 - 18 cells. The frontal sinuses are located within the frontal bone. The frontal sinus opening is located at the bottom of the cavity and is funnel-shaped, connecting with the middle nasal passage [12]. Within the sphenoid sinus, there is a septum separating the left and right cavities. All paranasal sinuses are lined with epithelial cells and the connecting channels to the nasal cavity serve for ventilation and transport of mucus. Healthy sinuses are characterized by unimpeded ventilation and normal function of cilia in mucus transport. In the case of viral or bacterial infection, the mucosal tissue becomes swollen, mucus secretion increases, the cilia function becomes impaired, and the nasal passage is partially or completely blocked, which might result in rhinosinusitis [13]. Judged by clinical symptoms, it is difficult to distinguish between viral sinusitis and bacterial sinusitis. Many junior doctors tend to think that sinusitis is an acute bacterial infection, and in 85% to 98% of the cases antibiotics are prescribed [1]. However, in 84% to 91% of the cases the infection is of viral origin [14-16]. Even if it is caused by bacteria, the condition disappears in most patients following anticongestion medication and without antibiotic treatment. The overuse of antibiotics, which has attracted widespread attention, has led to an alarming increase in bacterial antibiotic resistance and medical costs [17-19]. It has been estimated that half of the antibiotics use in human medicine is unnecessary, as the infections are caused by virus [20,21], and the use of antibiotics then only results in resistance development, which is growing rapidly worldwide, especially in Asia, including China, where 25-50% of people carry multidrug-resistant or methicillin-resistant bacteria [22-25].

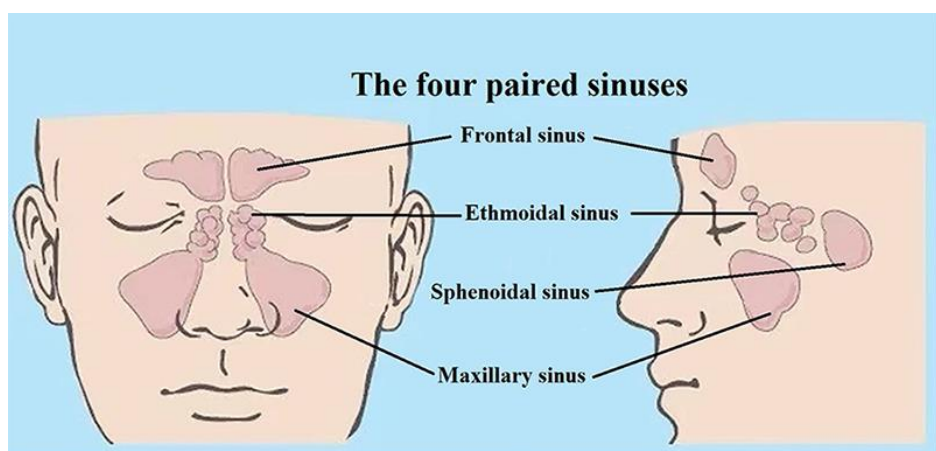


Figure 1. The anatomic locations of the human sinuses. A frontal and a coronal view are shown with the four paired sinuses. Anatomy figure adapted from Ref. [9].

The treatment of sinusitis is a huge challenge, where information technology can help in the diagnosis and support decisions on treatment. Accurate anatomical 3-dimensional models can be established based on X-ray computed tomography (CT) or magnetic resonance imaging (MRI) data, which can accurately differentiate the inflammatory soft tissue from obstructing secretions [24]. But CT and MRI diagnostic procedures are expensive, and often require a special imaging center, which involves travel, delays, and high costs. Thus, simplified diagnostic modalities would be very welcome [26,27]. The recently developed GASMAS (gas in scattering media absorption spectroscopy) technique shows considerable promise in assessing gas content of the sinuses. Our study focuses on the further development of this approach in the management of sinusitis.

1.2 Gas in scattering media absorption spectroscopy

Gas in Scattering Media Absorption Spectroscopy (GASMAS) is a technique used to investigate free gas inside pores or cavities surrounded by a highly light scattering medium [28]. The GASMAS technique is based on Tunable Diode Laser Absorption Spectroscopy (TDLAS), which uses the interaction between light and gas molecules to determine the concentration of a certain gas. The main concept behind the GASMAS technique is based on the difference between the absorption of light by free molecules in gases and by molecules in liquids and solids. The free gas molecules surrounded by the scattering medium have distinctive sharp absorption signatures, which are approximately 10,000 times narrower than those of the surrounding medium, making it possible to detect very unique signals associated with the gas [29].

When determining the concentration of a gas by using optical spectroscopy, the first step is to calculate the optical path length. In a non-scattering medium, the optical path length is well-defined and measurable. In a scattering medium, the photons pass through an unknown path through gas because of multiple light scattering. Based on the Beer-Lambert law, applied to the case of a scattering medium, the term equivalent average path length can be introduced. It can be determined by measuring the distance the photons must pass through a reference gas (usually the surrounding air), receiving a fractional absorption equivalent to that experienced when light passes through the sample under study [29].

As mentioned above, the GASMAS technique is based on the strong difference in the spectral characteristics between free gases and solid substances. In the analysis of gases surrounded by living tissues, the sharp absorption fingerprints of gases (in our case O₂ and H₂O) are easily distinguished from the slow changes in absorption of the main tissue constituents in blood, fat, muscle etc. While the physiological gas oxygen is of main interest in human GASMAS studies, water vapor can be used as a convenient reference gas [29,30]. Its concentration, e.g., in the sinuses, depends on the temperature and the relative humidity according to the Arden-Buck equation [31].

While our earlier GASMAS studies have been performed with home-built equipment, the instruments used in the present project were manufactured by the company Gasporox AB (Lund, Sweden). The instruments are constructed for monitoring of gas in food packages, and were modified by us for *in vivo* sinus monitoring. One of the systems was equipped with a laser operating close to 760 nm for oxygen monitoring, while the other one had a laser operating close to 818 nm, and suitable for water vapor monitoring. The oxygen monitoring system was, for the first time, used to study the gas exchange in the sinus cavities monitoring the oxygen signal when flushing nitrogen through the nose nostrils in conjunction with administration of anticongestion medication.

1.3 Previous work on frontal sinus cavities

After a proposal and first demonstration of the possibility to use GASMAS for sinus monitoring [32], a useful laboratory set-up with oxygen as well as water vapor measure-

ment capability was integrated. It was used in a study on healthy volunteers, where different geometrical arrangements of light injection and detector positions with regard to the frontal and maxillary sinuses were investigated, and the normalization of the oxygen signal on water vapor was first attempted [33]. While molecular oxygen is always measured using suitable rotational-vibrational transitions in its A-band close to 760 nm, water vapor was in that exploratory study probed using prominent lines close to 937 nm. However, at this wavelength liquid water, a main component of tissue, is also strongly absorbing, which is not the case at 760 nm. While the oxygen signal normalization to water vapor cannot be expected to work out perfectly in such a case (see below), the results were very encouraging, and a larger clinical study was planned. In preparation for this, a system capable of performing simultaneous monitoring of the two gases was constructed [34], and digital wavelength-modulation spectroscopy was introduced [35]. A subsequent clinical trial involved 40 patients, which were referred to CT imaging of the skull for diagnostics of sinus disorders [36]. It was shown, that GASMAS could characterize the sinuses equally well as the standard CT technique, which employs non-desirable ionizing radiation. While this result was very encouraging, still information on the stability and reproducibility of the signals over time was lacking. A first study of that kind was performed and reported in [37]. However, on this occasion, only equipment capable of water vapor monitoring was available, thus no oxygen gas assessment or study of sinus ventilation could be performed. The aim of the present study was to overcome earlier limitations and show directions on how to proceed to realistic clinical application. Thus, for the first time commercial equipment was adapted for clinical use, and the water vapor monitoring was moved to 818 nm, where a 10 times fainter absorption band is present, which in itself poses a challenge. Very stable signals for the individual gases, and in particular for the signal ratio, which is proportional to the oxygen concentration, could be established. While a sinus ventilation feasibility study by flushing the nostrils with nitrogen was included in [33], only healthy volunteers could be studied. In contrast, we could in the present work for the first time clearly and non-intrusively demonstrate, how decongestant spray could open up initially blocked connecting channels. Recently, an exploratory study, now on human maxillary sinuses in volunteers rather than on frontal sinuses, was performed as a MSc project at Lund university, Sweden [38].

2. Study design

The present study was designed to first establish suitable geometric arrangements for the laser light transmitting fiber and the detector with regard to the frontal sinuses. Measurements on volunteers were performed to study the stability of the oxygen and water vapor signals from the frontal sinuses. Ascertaining a reliable evaluation of the oxygen concentration is a further goal. To study the influence of administration of decongestant spray in unaffected and rhinitis volunteers was also a key aspect. The stability measurements were performed at different intervals; at the same time every day during seven consecutive days for long-term assessment, and every two hours throughout the day (12 hours), starting at 9.30 am and ending at 9.30 pm, for shorter-time investigation. The sinus ventilation study was performed by observing the influence of nitrogen flushing of the nasal cavity on the measured oxygen signal, in the presence and absence of decongestant spray. During 3 minutes of flushing through the nostril, the volunteer was asked to breath normally through the mouth.

In order to find optimum sinus signals, we put the detector in different positions to observe the strength of the signal (Figure 2). The light emitting fiber was positioned at the base of the nose and emitted the laser vertically upwards as seen in Figure 2. Based on exploratory measurements, we decided to choose 3 different measurement geometries: the detector 10 mm above the light source (Position I), 20 mm above the light source (Position II), and 10 mm above the center of the eyebrow (Position III), as shown in Figure 2. We set the signal sampling time to 2 seconds and recorded 30 sets of data at each marked position.

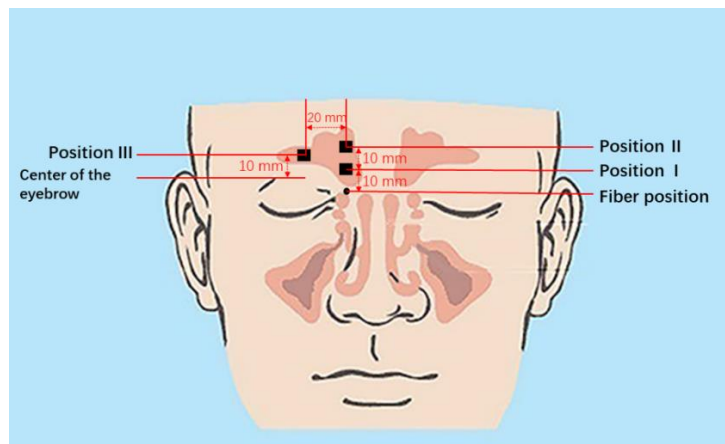


Figure 2. Location sites of the light emitting fiber and the detector. The size of the detector is $10 \times 10 \text{ mm}^2$ and positions relate to the center of the detector. Anatomy figure adapted from Ref. [9].

This study presents the first *in vivo* recordings of frontal sinuses using a laser emitting light at 760 nm matching one oxygen line combined with recording of water vapor using a laser at 818 nm. The aim of this study was to monitor the stability and reproducibility of the GASMAS signals in the monitoring of frontal sinus cavities. The study also presents for the first time the opening up of the sinus passages of a rhinitis affected volunteer, by administration of decongestant medication. Our study provides a foundation for a planned future trial in a clinical setting.

2.1 Volunteers

Four volunteers were included in the study. The volunteers agreed by signing a written consent to take part in the study, which uses a fully non-invasive technique.

Volunteers 1, 2 and 3 had no sign of a common cold or any sinus function aberrations.

Volunteer 4 had allergic rhinitis for a long time, which was accompanied by symptoms such as blocked nasal passages.

2.2 Gas monitoring systems

In contrast to earlier work, which employed laboratory designed systems working with wavelength-modulation spectroscopy techniques [35], we have in the present study used two modified commercial GASMAS systems supplied by Gasporox AB (Lund, Sweden). These systems were not designed for medical use, but rather for non-intrusive monitoring of gas in food packages. Accordingly, we have modified the interface to fit the present purpose of frontal sinus exploratory studies; see Figures 2 and 3. The systems were used for molecular oxygen and water vapor monitoring. The semiconductor lasers employed in the systems had output powers of about 5 mW. The systems utilize direct detection of the gas absorptive imprints. Figure 3 (a) shows the experimental arrangement, and Figure 3 (b) is a photograph of the detector. Finally, Figure 3 (c) is a photograph of the systems applied in measurement on a volunteer. An optical fiber transmitting probe carrying the laser light to the frontal sinuses was placed distally to the roof of the orbita pointing up towards the frontal bone with the sinus cavity. The detecting photodiode was placed on to the frontal bone above the light injection point at positions indicated in Figure 2. The arrangement can be considered to correspond to a modified back-scattering geometry. Figure 4 (a) shows a raw recording of the detected light when transmitting fiber and the detector were placed on opposite sides of a 2 cm thick test sample of strongly scattering polystyrene foam. The intensity rise of the ramp is due to the wavelength tuning, accomplished by increasing the driving current. Two faint absorption lines are indicated by arrows. As we can see, signals are very weak even for a sample with a long diffuse path-length through oxygen.

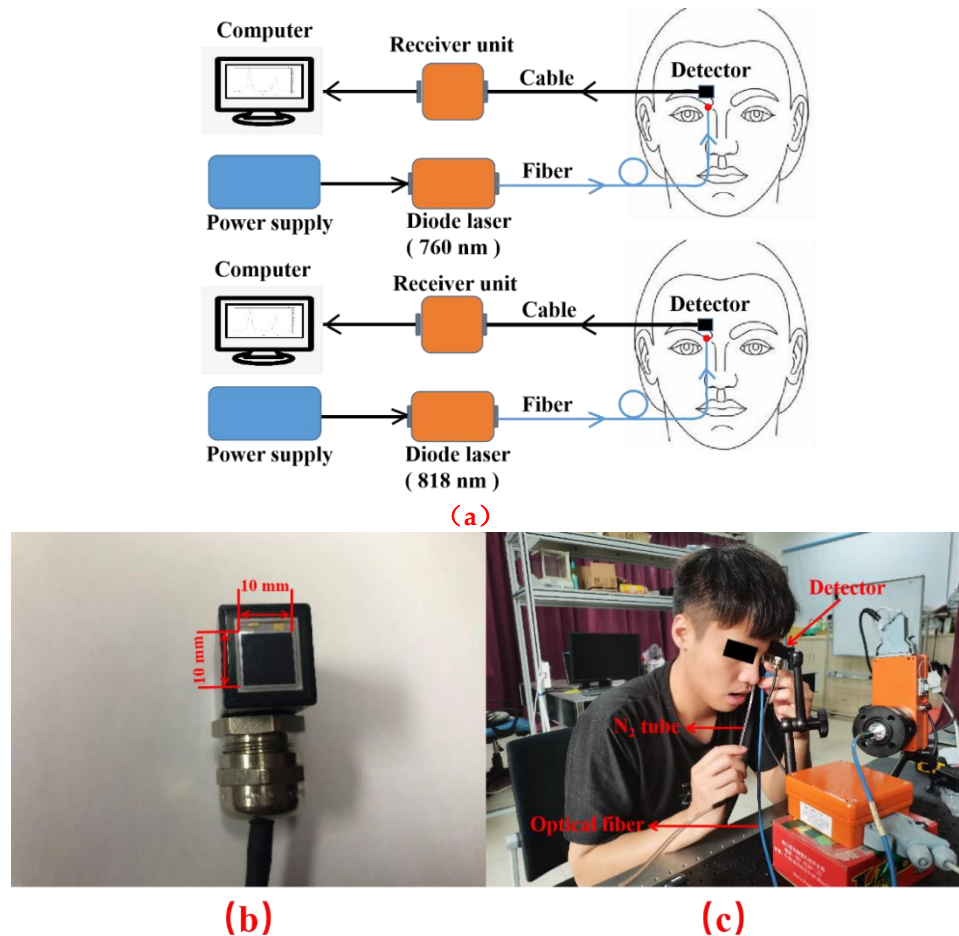


Figure 3. (a) Diagram of the arrangement of the two Gasmas systems with lasers, emitting light at 760 nm and 818 nm, respectively. (b) Photograph of the detector. (c) Photograph of the systems during measurement.

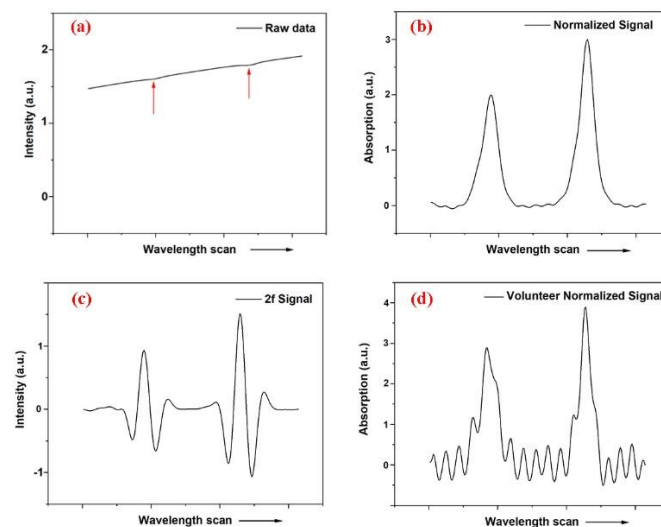


Figure 4. (a) Detector output when the laser frequency is ramped through two oxygen line positions. The sample is a 2 cm thick piece of polystyrene foam. (b) Isolated oxygen absorption signals derived from the data in Figure 4 (a). (c) The second derivative of the data shown in Figure 4 (b). (d) Typical recording of oxygen signals recorded through a human frontal sinus. The fitted fractional gas absorption $\Delta I/I$ is in our instrument expressed in the unit percent meter ($\% \cdot m$), since only the product of concentration and interrogated gas distance is determined.

225
226227
228
229
230231
232
233
234
235
236

Figure 4 (b) shows the two absorption lines isolated after subtracting a fitted background. It is well-known, that 1/f noise can effectively be suppressed by operating at a high frequency f. In wavelength modulation spectroscopy [35], employed in our earlier studies [33,34,36,37]. The frequency was modulated appropriately to generate a derivative-shaped signal due to the absorptive imprint. Frequently, the second derivative is used in the signal evaluation. In contrast, direct absorption monitoring was employed in the present work, still with good performance. Figure 4 (c) displays the second derivative of the data shown in Figure 4 (b), to provide a connection to the earlier work. Finally, Figure 4 (d) shows a typical recording of oxygen from a sinus cavity.

The retrieved absorption data we obtain from the system is the concentration C of a gas in the cavity times the effective scattering path length L in gas through the sinuses:

$$\text{Signal}(\% * m) = C(\%) * L(m) \quad (1)$$

When monitoring the signal with the 760 nm system we get the oxygen signal ($\text{Signal}_{(O_2)}$), and similarly when we use the 818 nm system we attain the water vapor signal ($\text{Signal}_{(H_2O)}$). As the water vapor concentration $C_{(H_2O)}$ is known, provided the temperature and relative humidity are known [31], the water vapor concentration can be used for normalization, and the oxygen concentration $C_{(O_2)}$ can be derived by dividing the expressions (1) for oxygen and water vapor:

$$\frac{\text{Signal}_{(O_2)}}{\text{Signal}_{(H_2O)}} = \frac{C_{(O_2)} * L_{(O_2)}}{C_{(H_2O)} * L_{(H_2O)}} \quad (2)$$

If the wavelengths used for the two gases would be very close to each other, the scattering and absorption through the sample would be the same, and the pathlength L through gas would be the same ($L_{(O_2)} = L_{(H_2O)}$), and the pathlength would be eliminated from the equation. We then have:

$$C_{(O_2)} = \frac{\text{Signal}_{(O_2)}}{\text{Signal}_{(H_2O)}} C_{(H_2O)} \quad (3)$$

Since 818 nm is quite close to 760 nm, an assumption of equal pathlength is still quite reasonable. Then the two measured signals and the water vapor concentration (known from the Arden-Buck relation and the known temperature) can be used to evaluate the oxygen concentration according to Eq. (3).

3. Measurements and results

3.1 Instrument calibration

Our instruments display the measured gas signal in units of %*m, reflecting the fact that only the product of concentration and pathlength is determined in measurements based on the Beer-Lambert law. The oxygen instrument is factory calibrated against the 21% ambient oxygen concentration for its standard use in food-package monitoring, and the %*m reading based on the signal fit to the recorded oxygen absorption lines apply directly to the GASMAS case. However, the situation is different for water vapor, which is not a normal application for this type of instruments. Air temperature, as well as relative humidity affects the calibration, which we now performed by sensing a 1 m distance of 25 °C room temperature and a measured relative humidity of 50%. Using the Arden-Buck relation [31], we found that the relative %*m value given as the signal output of the water vapor instrument should be multiplied by a factor 1.48 to yield absolute %*m values. The primary data for water vapor recorded in our subsequent studies and displayed in figures are the relative values, subject to the connection factor when true oxygen concentrations are evaluated in the normalization to water vapor data, as described by Eqs (2) and (3).

3.2 Signal stability

Two healthy volunteers were involved in our study of GASMAS signal stability and reproducibility.

3.2.1 Monitoring during one week

The one week signal stability monitoring study was performed with two clinically judged healthy volunteers without any sign of upper respiratory infection. The surrounding environment, such as the indoor temperature and humidity, was kept as constant as possible in order to reduce influence from surrounding factors. The measurements were scheduled at the same time during 7 consecutive days. Every measurement started with monitoring of the left side, followed by recordings of the same corresponding locations of the right side. The whole measurement procedure on both sides lasted for approximately 15 minutes. Arrangements were made to ensure full eye safety for volunteers and investigators.

Volunteer 1

Data in Figure 5 show measurement results for a first volunteer as recorded at the 6 chosen locations during one week. The first three histograms represent positions I, II and III of the left frontal sinus, and the latter three histograms represent positions I, II and III of the right frontal sinus, respectively. The recorded %*m values from the instruments are plotted with one standard deviation of the 30 consecutive recordings, each lasting 2 seconds.

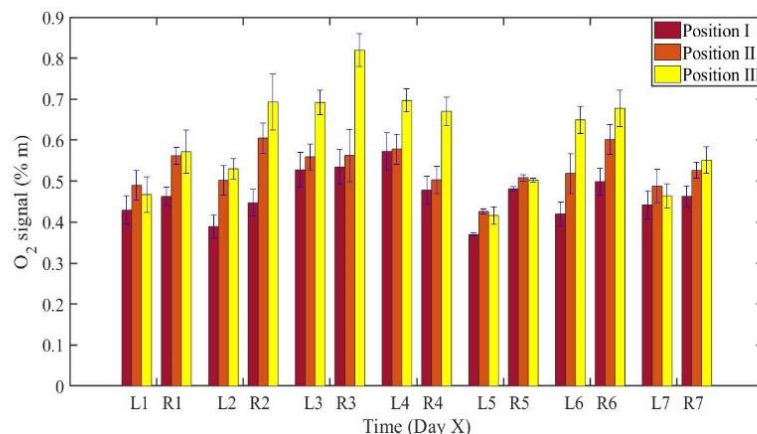


Figure 5. Sinus cavity oxygen signals recorded at six locations during 7 consecutive days (X) recorded for volunteer 1. Three values pertain to the left sinus (LX) and three values to the right sinus (RX). Values are given with one standard deviation.

Corresponding data for water vapor are shown in Figure 6, while the ratio of the oxygen and water vapor results (from Figures 5 and 6, respectively) is plotted in Figure 7. We note that day-to-day variations in gas signals are small, and that recorded differences between different locations are persistent over time. Also, the ratio data, which according to Eq. (2) are proportional to the oxygen concentration, are closely similar for all locations and over time. The same data are plotted in Figures 8–10, but now instead focusing on signal variations over time for individual measurement locations. Again, very consistent behaviour is observed.

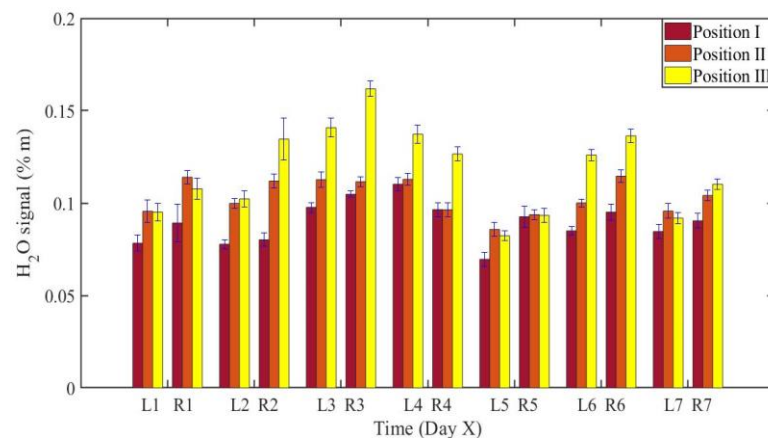


Figure 6. Sinus cavity water vapor signals recorded at six locations during 7 consecutive days recorded for volunteer 1. Three values pertain to the left sinus and three values to the right sinus. Values are given with one standard deviation.

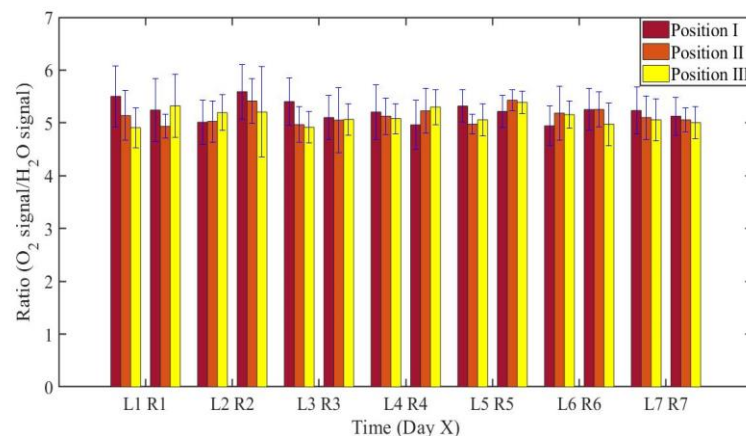


Figure 7. The ratio of oxygen signal to water vapor signal at the six locations for which data are given in Figures 5 and 6.

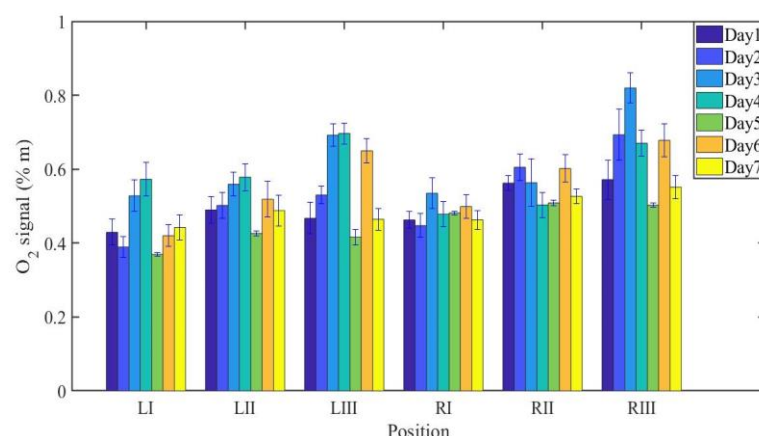


Figure 8. The changes of measured oxygen signal at different locations for volunteer 1 during one week, together with the standard deviation.

315
316
317
318319
320
321322
323
324

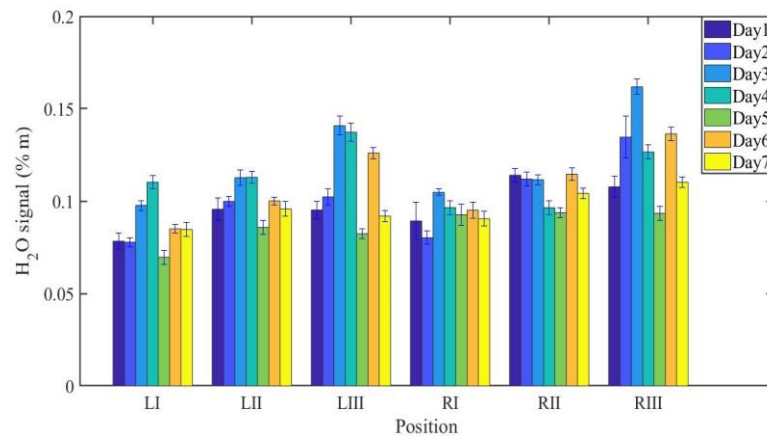


Figure 9. The changes of measured water vapor signal at different locations for volunteer 1 during one week, together with the standard deviation.

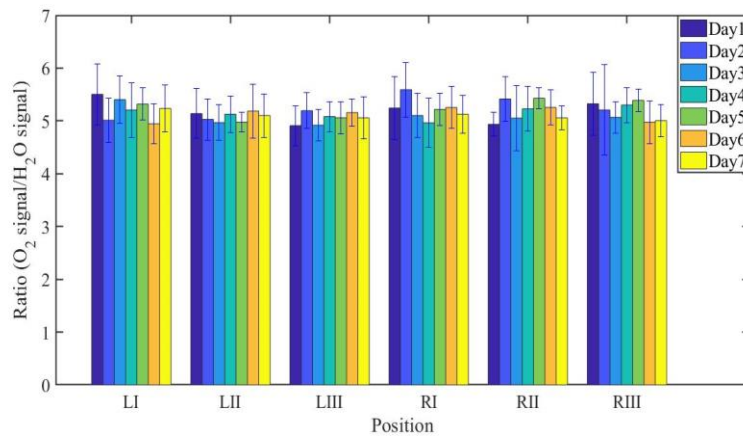


Figure 10. The ratio of measured oxygen and water vapor signals at different locations for volunteer 1 during one week, together with the standard deviation.

Volunteer 2

The same type of data as shown in Figures 5–10 for volunteer 1 were recorded for volunteer 2, and the results are shown in Figures 11–16.

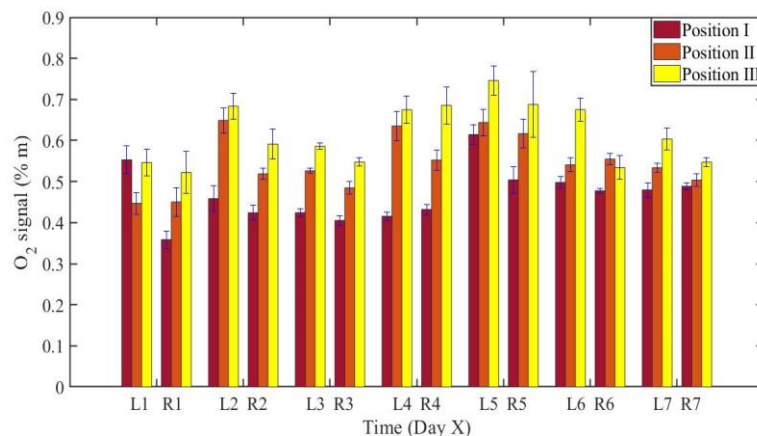


Figure 11. Sinus cavity oxygen signals recorded at six locations during 7 consecutive days (X) recorded for volunteer 2. Three values pertain to the left sinus (LX) and three values to the right sinus (RX). Values are given with one standard deviation.

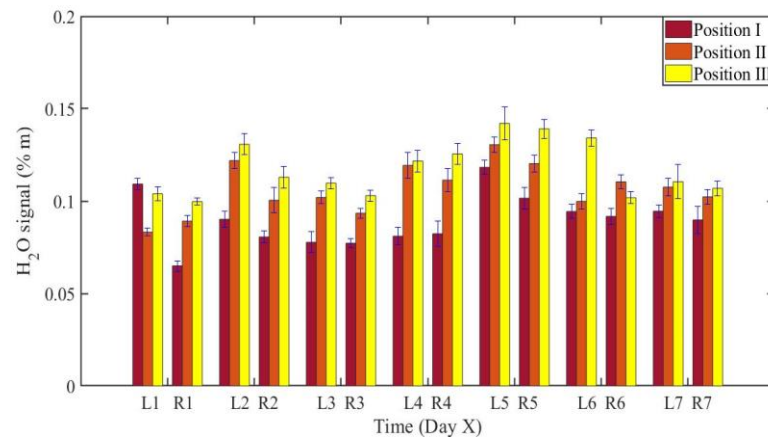


Figure 12. Sinus cavity water vapor signals recorded at six locations during 7 consecutive days recorded for volunteer 2. Three values pertain to the left sinus and three values to the right sinus. Values are given with one standard deviation.

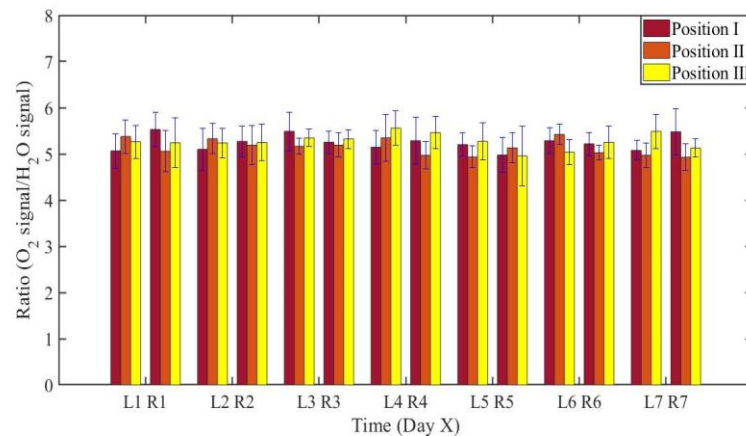


Figure 13. The ratio of oxygen signal to water vapor signal at the six locations for which data are given in Figures 12 and 13.

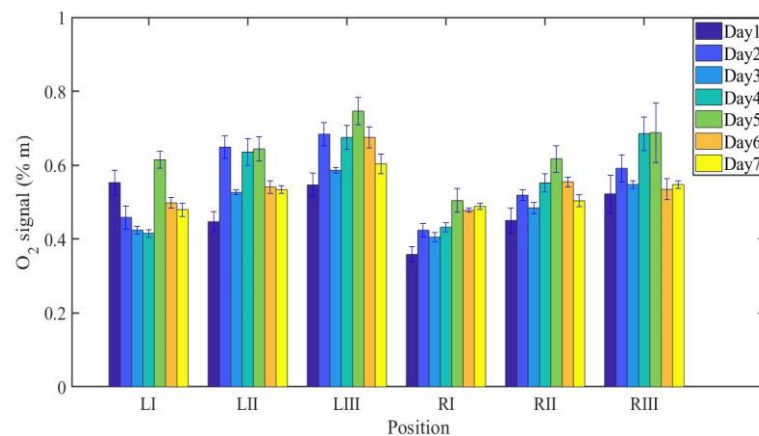


Figure 14. The changes of measured oxygen signal at different locations for volunteer 2 during one week, together with the standard deviation.

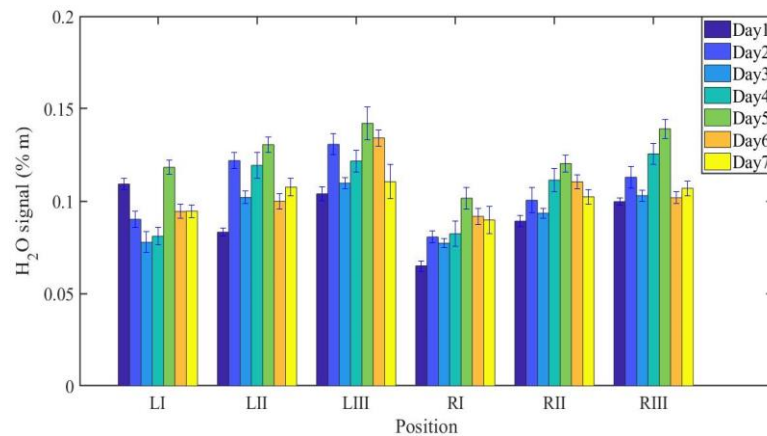


Figure 15. The changes of measured water vapor signal at different locations for volunteer 2 during one week, together with the standard deviation.

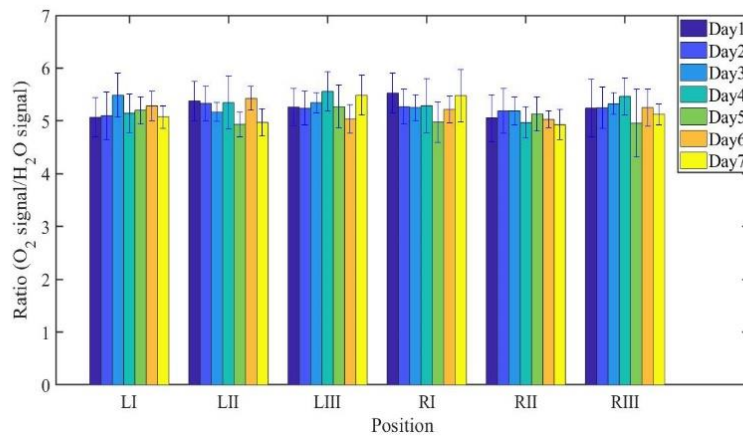


Figure 16. The ratio of measured oxygen and water vapor signals at different locations for volunteer 2 during one week, together with the standard deviation.

Like for volunteer 1, the data from volunteer 2 show similar consistency in value trends between locations and as a function of time.

3.2.2 Monitoring during one day

GASMAS data might be somewhat changing from day to day, e.g., because of different filling with mucus and possible slow changes in health status. Such trends are observed in the data given in Figures 5–16. In order to further assess the instrumental and methodological stability and reproducibility of the GASMAS technique applied in sinus monitoring, it was also considered valuable to follow the signals during a single day. For this study on volunteer 1, we chose to study only one position, at the left and right sides of the face. Gas signals from the sinuses of this volunteer were measured every two hours throughout the day, starting at 9:30 a.m. and ending at 9:30 p.m. Data for oxygen, water vapor and evaluated ratio are given with one standard deviation in Figures 17–19.

We can see from Figures 17–19 that the gas signals obtained from the volunteer are extremely stable and that small left-right asymmetry largely pertain through the day. The ratio data in Figures 7 (10), 13 (16), and 19 all give a value close to 5.2, with a very small error bar.

348
349
350

351
352
353

354
355
356
357
358
359
360
361
362
363
364
365
366
367
368
369

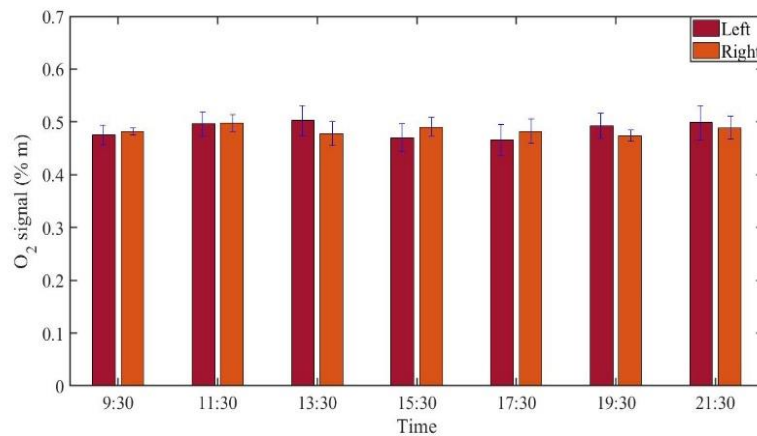


Figure 17. The changes of measured oxygen signal from a frontal sinus of the healthy volunteer 1 during one day. 371
372

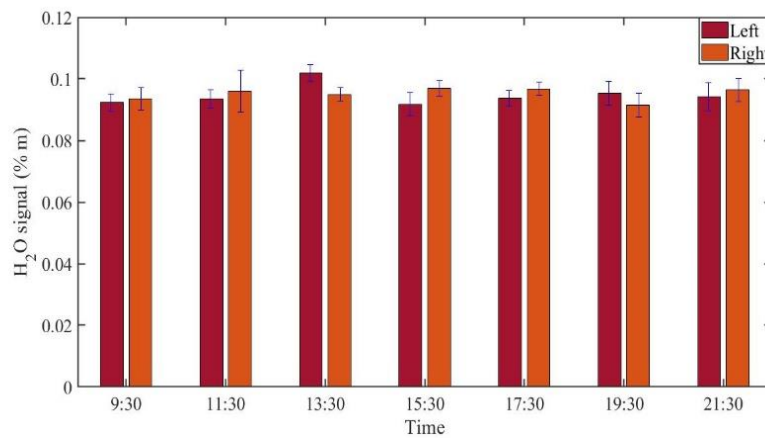


Figure 18. The changes of measured water vapor signal from a frontal sinus of the healthy volunteer 1 during one day. 374
375

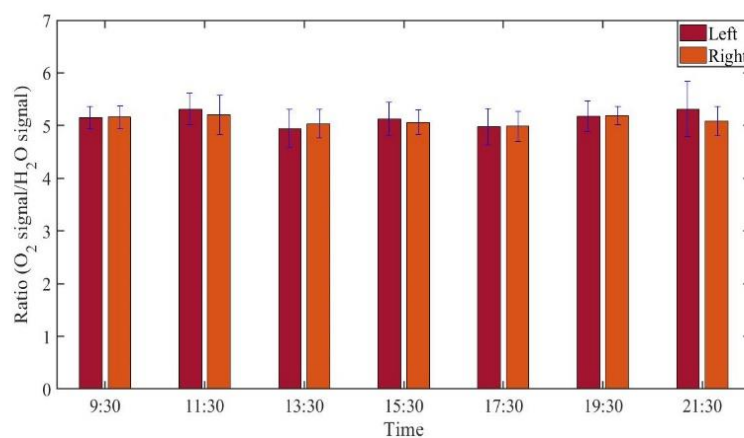


Figure 19. The ratio of measured oxygen signal to water vapor signal on volunteer 1 during one day. 377
378

3.3 Oxygen concentration retrieval

The sinuses are not highly ventilated, so the temperature is expected to be close to 37 °C, and the sinuses contain liquid water, leading to 100% relative humidity. According to the Arden-Buck relation [31], the concentration of water vapor in the sinuses is then

370

371
372

373

374
375

376

377
378

379

380
381
378
372

about 6.2 %. We then, according to Eq. (3), multiply the signal ratio by the concentration of water vapor in the sinuses, to attain the concentration of oxygen in the sinuses. According to Figures 7 (10), 13 (16), and 19, the ratio in the sinuses of all healthy volunteers is close to 5.2, a value which should be adjusted with the calibration factor 1.48, obtained in Sect. 3.1. We then obtain a true signal ratio of 3.5 and the resulting oxygen concentration $3.5 * 6.2\% \approx 22\%$, which is close to what is expected for well-ventilated sinuses.

3.4 Gas transport through ostia

Our gas transport study was performed using pure nitrogen, flushed through the nostril of two volunteers, one without any symptoms, and one with a clear rhinitis condition. During the flow, the volunteers breathed through the mouth only. We monitored oxygen gas at 760 nm with a geometry corresponding to position II. The study for each volunteer was divided into two parts. Every gas exchange monitoring sequence lasted for 10 minutes. As shown in Figure 20, first 60 recordings of the oxygen signal of the left frontal sinus of the healthy volunteer were taken during 2 min, to establish a background signal level. Then 90 recordings (3 min) were taken while a flow of pure nitrogen into the nostril was running. Finally, 150 recordings (5 min) were taken after we stopped the flow of nitrogen.

After the end of the first part of the study, we asked the healthy volunteer to rest for 20 minutes. At the 15th minute, we sprayed decongestant into the left nostril of the volunteer. After 5 minutes of action, we conducted the second part of the study, which again lasted for 10 minutes. For 60 recordings (2 min), we recorded the background oxygen level for the same frontal sinus of the volunteer after spraying decongestant. Then 90 recordings (3 min) were taken during nitrogen flow. Finally, 150 recordings (5 min) of the oxygen signal were taken after the nitrogen flow had stopped. Figure 20 shows the results of the recordings on the healthy volunteer.

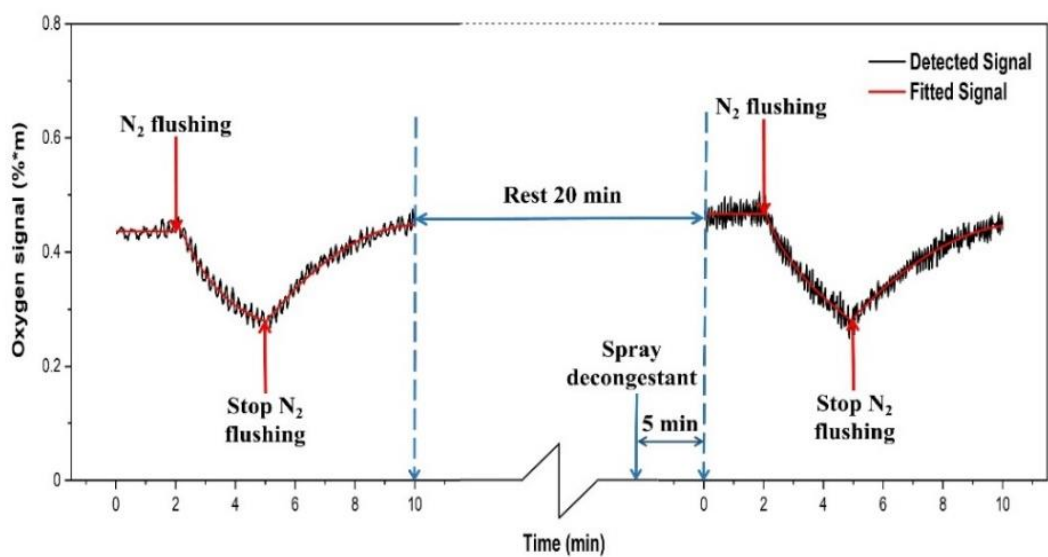


Figure 20. The measured O_2 signal from the left frontal sinus of the healthy volunteer. The dynamics of gas exchange, in the absence and presence of decongestant, is shown.

We note that in the first part of the study, when flowing nitrogen through the healthy volunteer's nostril, the oxygen signal decreases, indicating that the sinus channel was open, and nitrogen could partly replace oxygen in the sinus. After stopping the nitrogen flow, the oxygen signal returns to its original value signal recording, oxygen was again displacing nitrogen. Spraying the decongestant into the nostril of the healthy volunteer, we note, that the baseline oxygen value is basically the same, and also the dynamic be-

haviour on nitrogen flushing is the same. We note, that in both cases the fall-off and increase curves, when fitted with exponentials, remain indifferent with and without decongestant. The decay and increase curves have time constants of the order of the 5 minutes.

The corresponding data for the rhinitis volunteer, recorded in an identical measurement sequence are shown in Figure 21.

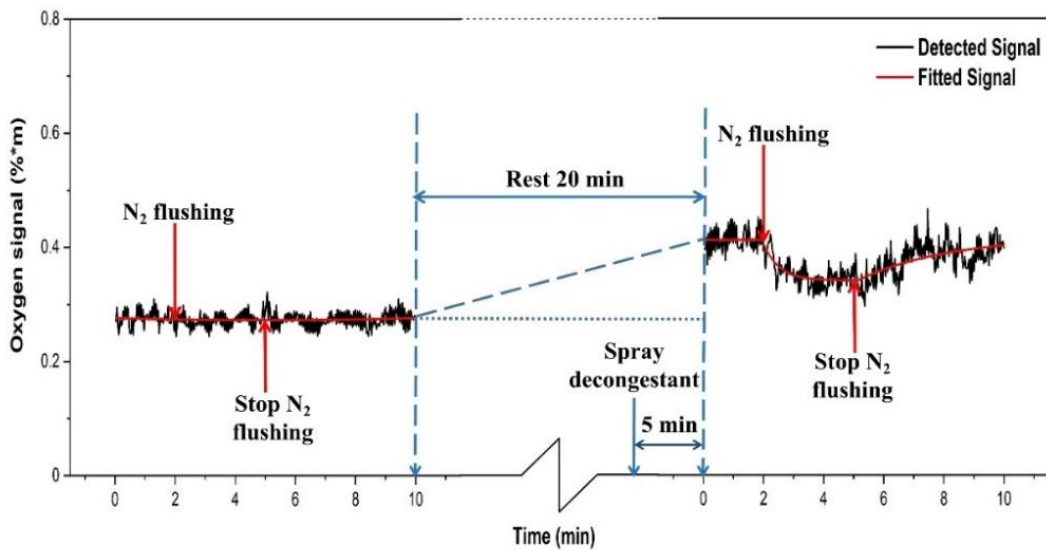


Figure 21. The measured O_2 signal from the left frontal sinus of the rhinitis volunteer. The influence of spraying a decongestant is shown.

We can see that when the rhinitis volunteer was not sprayed with decongestant, the oxygen signal basically did not change when nitrogen was let in, indicating that the nasal passage was blocked. The baseline value is about 0.27, which is significantly lower than for the healthy volunteers, with an average value for position II of volunteer 1 of 0.53 (Figure 8) and 0.54 for volunteer 2 (Figure 14). When we sprayed decongestant on the volunteer with rhinitis, and after 5 minutes measured the oxygen signal, we found that it had increased by 51% to 0.41, indicating that the initially low oxygen content in the closed sinus now increased by fresh air influx through the opened channel. When we filled the nasal cavity with nitrogen, the signal of oxygen decreased, verifying that the decongestant did open up the sinus nasal passage. However, now the maximum reduction was only 17% in contrast to 44% for the healthy volunteer.

4. Discussion and conclusions

The water vapor signal is related to the size of the sinus, since the water vapor concentration is constant and well-defined. Clearly, it also strongly depends on the measurement geometry, which in our study was kept constant for each measurement site. The oxygen signal depends on the size as well as the oxygen concentration in the sinus. By dividing the oxygen and water vapor signals, the size of the volume as well as the influence of the geometry is eliminated, and the oxygen concentration can be determined.

Measurements on healthy volunteers, frequently during one day, and also everyday during one week, demonstrated human frontal sinus gas signal stability both regarding water vapor and oxygen using noninvasive diode laser spectroscopy. Relative signal intensities for different monitoring sites largely persist as well as left-right asymmetries, showing that the technique provides highly stable reflections of sinus size/geometry. Small observed changes over time might reflect small difference in mucus volume. We used a laser at 760 nm for oxygen monitoring, and a laser at 818 nm (instead of at 937 nm) for water vapor monitoring for the first time for the study of the frontal sinus gas signals.

By moving the water vapor laser wavelength closer, the differences in attenuation and scattering in the light propagation are strongly reduced, thus improving the accuracy in oxygen concentration retrieval using Eqs (2) and (3).

Actually, we found the ratio of the oxygen and water vapor signal to be particularly stable, reflecting a constant oxygen concentration in well-ventilated sinus cavities. For volunteer 1, the ratio (standard deviation) as evaluated from all the data in Figures 7 (10) is 5.12 (0.03) for the left sinus, while we obtain 5.18 (0.11) for the right sinus. Corresponding values for volunteer 2 (Figures 13 (16)) are 5.23 (0.07) for the left sinus and 5.18 (0.08) for the right sinus. Likewise the ratio was found to be 5.11 (0.10) for the one-day monitoring of a single sinus of volunteer 1. We note that all these values closely coalesce. Using the global average 5.16 and applying the calibration factor 1.48 (Sect. 3.1), we, with an expected water vapor concentration of 6.2% ($T=37^{\circ}\text{C}$, RH=100%) arrive, at a sinus average concentration of 21.6%. The value is close to the average concentration of inhaled and exhaled air, 21 and 17%, respectively. The deviation is easily explained by small inaccuracies in calibration and sinus temperature values (exponential dependence) and relative humidity (linear dependence). As an example, a temperature reduction of the sinus air with 1°C would lead to an oxygen concentration reduction from 21.6% to 20.4%.

Furthermore, our study showed that it is possible to objectively assess sinus ventilation through channels. We studied the effect on the oxygen content of spraying decongestant of the frontal sinus of volunteers with and without rhinitis. Nitrogen flushing before and after spraying decongestant was performed. The opening up of the channel with decongestant was established for the first time by observing the action of nitrogen flow into the sinus. Since the nasal passages of healthy volunteers are always open, we, as expected, do not see any significant influence of the decongestant spray. Together with clinical partners we now plan to conduct a study on patients to establish the clinical value of the method. In particular, we plan to relate the type of bacteria found in patients suffering from sinus disorders to the GASMAS signal, in search for possible correlations which may prove useful in sinusitis diagnostics.

Author Contributions: Conceptualization, KS, SS; methodology, HZ, NH, KS and SS; data curation, HZ, NH, YL and JH; writing—original draft preparation, HZ and NH; writing—review and editing, KS and SS; supervision, KS and SS; All authors have read and agreed to the published version of the manuscript.

Funding: The project was supported by the Science and Technology Program of Guangzhou (2019050001), and the Guangdong Provincial Key Laboratory of Optical Information Materials and Technology (2017B030301007).

Institutional Review Board Statement: Since the study was a small pilot on healthy fellow students with a completely non-invasive technique, formal approval was deemed not necessary in China.

Informed Consent Statement: Informed written consent was obtained from all volunteers involved in the study.

Acknowledgements: The authors gratefully acknowledge the continuing support from Prof. Guofu Zhou, Dean of South China Academy for Advanced Optoelectronics, and fruitful discussions with Dr. Min Zhou and Prof. Yan Ruan of the Guangzhou University of Traditional Chinese Medicine. We thank Lingna Hu for contributions at the early stage of the project, and Dr. Patrik Lundin of Gasporox AB for technical support.

Conflicts of Interest: SS and KS have minor shares in Gasporox AB the company, which delivered the GASMAS equipment employed.

References

1. Snow, V.; Mottur-Pilson, C.; Hickner J. M. Principles of appropriate antibiotic use for acute sinusitis in adults. *Ann. Intern. Med.* **2001**, *134*, 495–497. 504
505
506
2. Anzai, Y.; Yueh, B. Imaging evaluation of sinusitis: diagnostic performance and impact on health outcome. *Neuroimag. Clin. N. Am.* **2003**, *13*, 251–263. 507
508
3. Leo, G.; Mori, F.; Incorvaia, C.; Barni, S.; Novembre, E. Diagnosis and management of acute rhinosinusitis in children. *Curr. Allergy. Asthma. Rep.* **2009**, *9*, 232–237. 509
510
4. Smith, K. A.; Orlandi, Richard R.; Rudmik, L. Cost of adult chronic rhinosinusitis: a systematic review. *Laryngoscope* **2015**, *125*, 511
1547–1556. 512
5. Rudmik, L.; Economics of chronic rhinosinusitis. *Curr. Allergy. Asthma. Rep.* **2017**, *17*, 20. 513
6. Brook, I. Current issues in the management of acute bacterial sinusitis in children. *Int. J. Pediatr. Otorhinolaryngol.* **2007**, *71*, 1653–514
1661. 515
7. Anand, V. K. Epidemiology and economic impact of rhinosinusitis. *Ann. Otol. Rhinol. Laryngol.* **2004**, *113*, 3–5. 516
8. Jankowski, R.; Nguyen, D. T.; Poussel, M.; Chenuel, B.; Gallet, P.; Rumeau, C. Sinusology. *Eur. Ann. Otorhinolaryngol.* **2016**, *133*, 517
263–268. 518
9. <https://mts.jk51.com/tushuo/2702655.html>. 519
10. Whyte, A.; Boeddinghaus, R. The maxillary sinus: physiology, development and imaging anatomy. *Dentomaxillofac. Radio.* **2019**, 520
48, 20190205. 521
11. Takahashi, R. Y. O. The formation of the human paranasal sinuses. *Acta. Otolaryngol.* **1984**, *97*, 1–28. 522
12. Kuhn, F. A. An integrated approach to frontal sinus surgery. *Otolaryngol. Clin. North. Am.* **2006**, *39*, 437–461. 523
13. Ebelt, M. H.; McKay, B.; Dale, A.; Guilbault, R.; Ermias, Y. Accuracy of signs and symptoms for the diagnosis of acute rhinosinusitis and acute bacterial rhinosinusitis. *Ann. Fam. Med.* **2019**, *17*, 164–172. 524
525
14. Rosenfeld, Richard, M.; Acute sinusitis in adults. *N. Engl. J. Med.* **2016**, *375*, 962–970. 526
15. Smith, S. S.; Ference, E. H.; Evans, C. T.; Tan, B. K.; Kern, R. C.; Chandra, R. K. The prevalence of bacterial infection in acute 527
rhinosinusitis: a systematic review and meta-analysis. *Laryngoscope* **2015**, *125*, 57–69. 528
16. Autio, T. J.; Koskenkorva, T.; Leino, T. K.; Koivunen, P.; Alho, O. P. Longitudinal analysis of inflammatory biomarkers during 529
acute rhinosinusitis. *Laryngoscope* **2017**, *127*, E55–E61. 530
17. Patel, H.; Zhang, W.; Kuo, Y.; Sharma, G. Impact of choosing wisely on antibiotic prescription and CT scan use for uncomplicated 531
acute rhinosinusitis (ARS). *J. Allergy. Clin. Immunol.* **2018**, *141*, AB166. 532
18. Melanie, D.; Desrosiers, M. Guidelines for management of acute bacterial rhinosinusitis: impact on Quebec physicians' prescriptions 533
for antibiotics. *Otolaryngol. Head. Neck. Surg.* **2007**, *136*, 258–260. 534
19. Benninger, M. S.; Holzer, S. E. S.; Lau, J. Diagnosis and treatment of uncomplicated acute bacterial rhinosinusitis: summary of 535
the Agency for Health Care Policy and Research evidence-based report. *Otolaryngol. Head. Neck. Surg.* **2000**, *122*, 1–7. 536
20. Lux, C.; Johnston, J.; Zoing, M.; Biswas, K.; Taylor, M.; Douglas, R. Antibiotic treatment for chronic rhinosinusitis: Prescription 537
patterns and associations with patient outcome and the sinus microbiota. *Frontiers in Microbiology* **2020**, *11*, 595555. 538
21. Lemiere, M. B.; Driel, M. L.; Merenstein, D.; Liira, H.; Mäkelä, M.; De Sutter, A. I. Antibiotics for acute rhinosinusitis in adults. 539
Cochrane. Database. Syst. Rev. **2018**, *9*, CD006089. 540
22. Stefani, S.; Chung, D. R.; Lindsay, J. A.; Friedrich, A. W.; Kearns, A. M.; Westh, H.; MacKenzie, F. M. Meticillin-resistant Staphylococcus aureus (MRSA): global epidemiology and harmonisation of typing methods. *Int. J. Antimicrob. Agents.* **2012**, *39*, 273–541
282. 542
23. Lee, A. S.; de Lencastre, H.; Garau, J.; Kluytmans, J.; Malhotra-Kumar, S.; Peschel, A.; Harbarth, S. Methicillin-resistant Staphylococcus aureus. *Nat. Rev. Dis. Primers.* **2018**, *4*, 1. 544
545
24. Raut, A.; Jankharia, B.; Paranasal Sinuses in Health and Disease. In: Stucker, F.; Kenyon, G.; Lian, T.; Draf, W.; Schick, B. (eds) 546
Rhinology and Facial Plastic Surgery. Springer, Berlin, Heidelberg **2009**, 35–62. 547
25. Head, K.; Chong, L. Y.; Piromchai, P.; Hopkins, C.; Philpott, C.; Schilder, A. G.; Burton, M. J. Systemic and topical antibiotics for 548
chronic rhinosinusitis. *Cochrane. Database. Syst. Rev.* **2016**, *4*, CD011994. 549
26. Ebelt, M. H.; Hansen, J. G. Proposed clinical decision rules to diagnose acute rhinosinusitis among adults in primary care. *Ann. 550
Fam. Med.* **2017**, *15*, 347–354. 551
27. Ebelt, M. H.; McKay, B.; Guilbault, R.; Ermias, Y. Diagnosis of acute rhinosinusitis in primary care: a systematic review of test 552
accuracy. *Br. J. Gen. Pract.* **2016**, *66*, e612–e632. 553
28. Sjöholm, M.; Somesfalean, G.; Alnis, J.; Andersson-Engels, S.; Svanberg, S. Analysis of gas dispersed in scattering solids and 554
liquids. *Opt. Let.* **2001**, *26*, 16–18. 555
29. Svanberg, S. Gas in scattering media absorption spectroscopy – from basic studies to biomedical applications. *Lasers Photonics 556
Rev.* **2013**, *7*, 779–796. 557
30. Svanberg, K.; Svanberg, S. Monitoring free gas in situ for medical diagnostics using laser spectroscopic techniques. *Frontiers in 558
Biophotonics for Translational Medicine*, Eds. M. Olivo and U.S. Dinish (Springer Science and Business Media Singapore 2016). 559
31. Buck, A. L. New equations for computing vapor pressure and enhancement factor. *J. Appl. Meteorol. Climatol.* **1981**, *20*, 1527–1532. 560
32. Persson, L.; Svanberg, K.; Svanberg, S. On the potential of human sinus cavity diagnostics using diode laser gas spectroscopy. 561
Appl. Phys. B **2006**, *82*, 313–317. 562

33. Persson, L.; Andersson, M.; Cassel-Engquist, M.; Svanberg, K.; Svanberg, S. Gas monitoring in human sinuses using tunable diode laser spectroscopy. *J. Biomed. Opt.* **2007**, *12*, 054001. 563
564
34. Lewander, M.; Guan, Z. G.; Svanberg, K.; Svanberg, S.; Svensson, T. Clinical system for non-invasive in situ monitoring of gases in the human paranasal sinuses. *Opt. Express* **2009**, *13*, 10849–63. 565
566
35. Mei, L.; Svanberg, S. Wavelength modulation spectroscopy-digital detection of gas absorption harmonics based on Fourier analysis. *Appl. Optics* **2015**, *54*, 2234–43. 567
568
36. Lewander, M.; Lindberg, S.; Svensson, T.; Siemund, R.; Svanberg, K.; Svanberg, S. Noninvasive diagnostics of the maxillary and frontal sinuses based on diode laser gas spectroscopy. *Rhinology* **2012**, *50*, 26–32. 569
570
37. Huang, J.; Zhang, H.; Li, T.; Lin, H.; Svanberg, K.; Svanberg, S. Assessment of human sinus cavity air volume using tunable diode laser spectroscopy, with application to sinusitis diagnostics. *J. Biophotonics* **2015**, *8*, 985–992. 571
572
38. Mekamy, S. In-vivo study on the stability of the use of gas absorption spectroscopy as a technology for accessing sinus cavity size and oxygen gas concentration. MSc thesis, Department at Biomedical Engineering, Lund University, **2020**. 573
574

Identification of flying insects in the spatial, spectral and time domains with focus on mosquito imaging

Yuting Sun^{1,2,*}, Yueyu Lin^{1,2,*}, Guangyu Zhao¹, and Sune Svanberg^{1,2,3+}

- ¹ Guangdong Provincial Key Laboratory of Optical Information Materials and Technology & Center for Optical and Electromagnetic Research, South China Academy of Advanced Optoelectronics, South China Normal University, Guangzhou 510006, China
² National Center for International Research on Green Optoelectronics, South China Normal University, Guangzhou 510006, P. R. China
³ Department of Physics, Lund University, P.O. Box 118, SE-221 00 Lund, Sweden
* These authors contributed equally to this work
+ Correspondence: sune.svanberg@fysik.lth.se

Citation: Sun, Y.T.; Lin, Y.Y.; Zhao, G.Y.; Svanberg, S. Identification of flying insects in the spatial, spectral and time domains with focus on mosquito imaging. *Sensors* **2021**, *21*, x. <https://doi.org/10.3390/xxxxx>

Academic Editor: Firstname Lastname

Received: date

Accepted: date

Published: date

Publisher's Note: MDPI stays neutral with regard to jurisdictional claims in published maps and institutional affiliations.



Copyright: © 2021 by the authors. Submitted for possible open access publication under the terms and conditions of the Creative Commons Attribution (CC BY) license (<http://creativecommons.org/licenses/by/4.0/>).

Abstract: Insects constitute a very important part of the global ecosystem and include pollinators, disease vectors and agricultural pests, all with pivotal influence on society. Monitoring and control of such insects has high priority, and automatic systems are highly desirable. While capture and analysis by biologists constitutes the golden standard in insect identification, optical and laser techniques have the potential of high-speed detection and automatic identification based on shape, spectroscopic properties such as reflectance and fluorescence, as well as wing-beat frequency analysis. The present paper discusses these approaches, and in particular presents a novel method for automatic identification of mosquitos based on image analysis, as the insects enter a trap based on a combination of chemical and suction attraction. Details of the analysis procedure are presented, and selectivity is discussed. As a powerful and cost-effective method we finally propose the combination of imaging and wing-beat frequency analysis in an integrated instrument.

Keywords: insects; mosquito; spectroscopy; wing-beat frequency; image.

1. Introduction

Insects exhibit the largest variety of species in the animal kingdom with an estimated number of 5.5 million varieties [1], and represented by 1 gigatons of carbon they account for the largest fraction of the total animal biomass [2]. Clearly, they play a very important part of the global ecosystem, and are like the rest of the biosphere also influenced by global change [3]. Among the numerous types of insects, pollinators, disease vectors and agricultural pests all have a pivotal influence on society. Pollinators are indispensable in food production, and in the absence of insects the diet would be very limited and meager [3]. Disease vectors include malaria-carrying mosquitos, such as *Anopheles*, which transfer *Plasmodium* parasites, responsible for about 400,000 deaths annually, mostly children in Africa [4]. Additional vectors, including for dengue fever, West Nile and Zika virus, Japanese encephalitis, and yellow fever, account for further 300,000 deaths annually [5]. Agricultural pests, such as classical locusts, army worms, plant hoppers, etc. are responsible for strong crop losses in many parts of the world. Monitoring and control of such insects have a high priority, and automatic systems are highly desirable. Many of the insects of interest have wings and can move over considerable distances. While capture and analysis by biologists constitutes the golden standard in insect identification, optical and laser techniques have the potential of high-speed detection and automatic identification when

insects are in flight. Analysis can be based on shape, spectroscopic properties such as reflectance, depolarization, and fluorescence, as well as wing-beat frequency monitoring. Many approaches can be implemented in remote-sensing systems such as time-of-flight-(TOF), or CW bi-static light detection and ranging (lidar) installations, while additionally, imaging followed by processing could be available in *in-situ* insect traps.

The present paper discusses these approaches, and in particular presents a novel method for automatic identification of mosquitos based on image analysis. Details of the procedure are presented, and selectivity is discussed. Before going into our method for insect identification by image processing, we will briefly describe techniques based on spectroscopy and wing-beat frequency analysis. We will especially relate to our own experience, and in a concluding section discuss pros and cons for different approaches. Finally, we propose a cost-effective system based on basic image processing and wing-beat frequency analysis implemented in an insect trap.

Reflectance, depolarization and fluorescence spectroscopy

Spectroscopic approaches (see, e.g., [6,7]) interrogate the molecular constituents of objects, naturally then also including insects. Photonic interactions related to atmospheric as well as aquatic fauna were recently reviewed in [8]. The reflectance spectrum recorded following illumination with a broad spectral distribution of radiation corresponds to the perceived color, but of course also extends outside the region accessible to the human eye, i.e., to the ultraviolet (UV) and infrared (IR) domains. Surface reflections (specular reflection) do not carry information on the interior of the material, which the diffuse light does. Then scattering inside the substance has occurred and specific absorption, governed by the Beer-Lambert law, is revealed as color in a generalized sense. Specifically, polarization analysis can be performed, and the depolarization of primary impinging linearly polarized light can carry information on the structure of an insect in terms of hairiness, microstructures, etc. In particular, insects can be distinguished from raindrops [9], which according to Mie scattering theory exhibit no depolarization. We note that colors also can result from ordered nanostructures in, e.g., insect wings and bodies. Such structural colors, which are among the most spectacular in the animal kingdom, are due to interference effects [10].

Reflection spectra from flying insects were first reported in [11], where a simple amateur astronomical telescope, connected to a compact digital spectrometer was directed horizontally towards a background termination, arranged to be as dark as possible and placed at a distance of about 100 meter. When white sunlight, reflecting off insects flying into the telescope field-of-view, abrupt spikes rising up from the low background were spectrally recorded. Species of damselflies were identified. Similar dark-field work employing sunlight, but also an artificial lamp at night time, was reported in [12] for the case of Chinese agricultural pests. Laboratory controlled studies on released insects gave detailed information on the reflectance spectra of certain pests, and corresponding fluorescence spectra were also recorded [13]. Later, also full multi-spectral reflection imaging of insects using an imaging spectrometer has been accomplished; see, e.g., [14].

Fluorescence, induced by a UV laser or other radiation source, and appearing Stokes-shifted towards longer wavelengths, can carry complementary information on the molecular constituents, although spectral structures are, like for reflectance, broad with overlapping contributions from major constituents such as melanin, carotinoids, etc., pertinent to insects. Sharper Raman structures due to characteristic molecular vibrations may also be observed for major constituents. Fluorescence spectra from insects were reported in [15,16] using pulsed-laser TOF lidar techniques, which have a wide applicability in remote-sensing environmental monitoring and the study of cultural heritage (see, e.g., [17–19]). By first dusting caught and identified insects with fluorescent dyes, unique spectral signatures are obtained, and the dispersion of insects in their natural habitat can be studied [16]. Fluorescence lidar monitoring of Chinese agricultural pests were also performed [20] using TOF lidar techniques, and could also be extended to flying birds [21].

Wing-beat frequency analysis

Flying insects flap their wings with frequencies, which are related to the species, and also to the sex within the same species. This gives rise to well-known sounds with typical pitch, which are readily recognized by humans as being different for mosquitos, flies and bees. Clearly, analyzing the sounds captured by a microphone adds specificity to the approach. Thus, acoustic systems employing pressure waves for insect identification have been developed (see, e.g., [22,23]). Wing-beats can also be detected as oscillation in the light, which scatters off a flying insect. This can be observed in passive, dark-field, systems using ambient light [12], but more conveniently using high-repetition-rate or CW lidar systems. First results related to lidar monitoring of bees, as reported in [24,25], and with the application to the detection of hidden land-mines and explosives when using honey bees, which were specially trained to be attracted to TNT fumes. Insect detection and associated wing-beat frequency analysis at considerable range were made highly realistic with the introduction of CW, bi-static lidar systems based on the Scheimpflug principle [26]. Such systems, which are also very powerful for aerosol and air pollutant monitoring, are described, e.g., in [27-29]. Scheimpflug lidars observe a transmitted CW laser beam at an angle with a low-price amateur astronomy telescope, placed less than a meter from the transmitting optics and on a co-rotated platform. The imaging detector is arranged at a specific angle, for which the laser beam is imaged sharply on the detector array, at close as well as at far range. In contrast to TOF lidar systems, where the signal intensity falls off with an $1/r^2$ dependence (r being the range), a Scheimpflug lidar basically shows a constant signal level out to large ranges, but now with a strongly falling-off range resolution. Since the array detector can be read out at high speed, a high temporal resolution is obtained, allowing also wing-beat frequencies up to hundreds of Hz to be recorded, and with a capability of a hundred of thousands observed events for single-night recordings.

Such systems have been employed in many field experiments on different continents, where monitoring of wing-beat frequencies was also performed (see, e.g., [30-34]). Analysis of light depolarization [9], insect flight speed [33], and differential back-scattering using two laser wavelengths (see, e.g., [35-37]) has also been accomplished. Normally, Scheimpflug lidar systems operate with elastic back-scattering from the targets. However, by using a double Scheimpflug arrangement, with a 2-D detector, the fluorescence spectrum induced by a blue CW laser can be recorded for each range interval. This was demonstrated for under-water lidar monitoring at ranges up to 5 meters [38,39], and also for terrestrial vegetation monitoring from a light-weight drone-based system [40].

It should be noted that several non-lidar laser-based system have been constructed for in-situ or close-range characterization of insects [41-44]. These include systems with different laser or LED wavelengths, allowing crude reflectance characterization, as well as studies of depolarization. Below, we will concentrate on in-situ sampling systems, which combined with optical detection have the potential for be particularly realistic and cost-effective.

2. Mosquito sampling method

2.1. Common sampling methods

We will here first describe current mosquito sampling methods and then present the system used in our imaging study. The main conventional methods for monitoring adult mosquitoes are the human-landing catch, human-baited double net trap, and light traps techniques. The human-landing catch approach uses a hollow tube for mosquitoes trying to penetrate the human skin [45]. This method puts collectors at risk of being bitten by infectious mosquitoes and contracting malaria, which is of course very problematic. The human-baited double net trap is divided into an inner net and an outer net [46]. The attractant sits in the enclosed area of an inner net, exposing free skin areas; the collector then

uses an electric mosquito sucker between the inner net and the outer net to collect mosquitoes, which settled on the mosquito net. Since the distance between the attractor and the mosquitoes is larger, the mosquito trapping effect may be reduced accordingly. The light trap method utilizes the phototaxis of mosquitoes. The mosquito light trap is often placed near mosquito breeding grounds [47]. It has limitations such as easy damage to the equipment, and attraction of also other types of insects subject to phototaxis.

2.2. Present system description

The instrument designed for the present experiments avoids certain problems of the types mentioned above. The structure of the arrangement is shown in Figures 1 and 2. We use a Biogents BG-Sentinel commercial trap [48], on top of which we installed the imaging unit. The two parts are marked with ① and ② in Figure 1. An illuminator ④ is placed on the top of the instrument. On the one hand, it realizes the function of light trapping, and on the other hand, it provides illumination for the photos taken by the camera ③. On the opposite side of the camera, the instrument uses black cloth ⑥ as the scene background, which increases the contrast in the photos of the insects taken by the camera.

The lower BG-Sentinel trap part of the instrument is a foldable white fabric cylindrical container, 40 cm high and 36 cm in diameter. At the bottom of the container is an attractant ⑨ that simulates human odor. The middle part of the instrument is connected to a black mosquito catching net bag ⑦. A fan ⑧ is placed under the mosquito net bag, and causes an air flow to suck mosquitoes into the mosquito net bag. The air flow effectively prevents the trapped mosquitoes from flying again and the bag ensures that the mosquitoes will not be damaged by the fan.

The light and the odor attractant bring mosquitoes to the instrument, where they enter a small opening ⑤ on the top, as caught by the air flow produced by the fan. The camera will take pictures of the mosquitoes sucked into the instrument. The photos are transferred to a personal computer, where insects are counted and classified as described in Sect. 3.2. Our image recognition algorithm effectively distinguishes mosquitoes from some other phototaxis insects captured by the instrument, ensuring a high accuracy of the

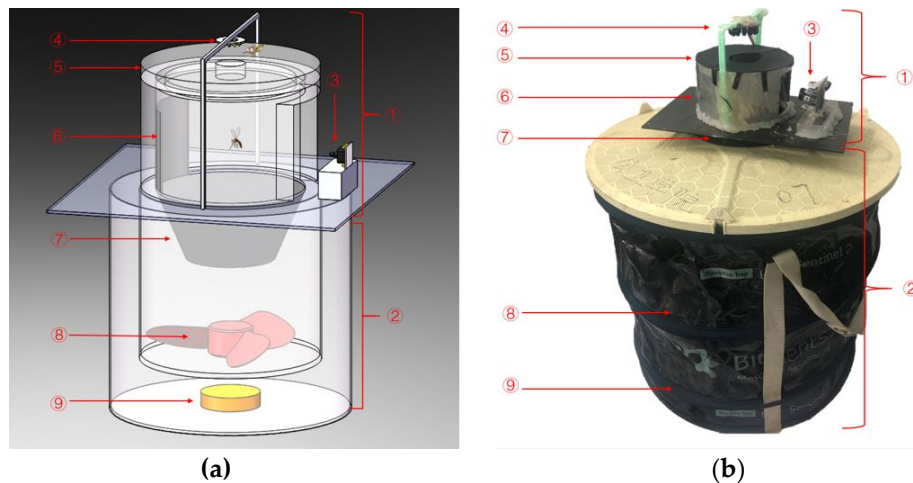


Figure 1. Overall structure of the instrument, consisting of an image recording section ① placed on top of a BG-Sentinel commercial mosquito trap ②. ③ indicates a camera for taking pictures and ④ is an illuminator placed on the top of the instrument. The cover has a small opening ⑤ on top. Black cloth ⑥ is used as the scene background. Mosquitoes are caught in a black net bag ⑦. A fan ⑧ is placed under the mosquito net bag, and at the bottom of the container there is an attractant ⑨. Fig. 1 (a) shows the design structure of the system, while 1 (b) is a physical photo of the system.

data. The cost of our instruments is very low, and it is quite sturdy and can be deployed for large-scale, long-term monitoring of mosquitoes. It can save a lot of manpower and material resources.

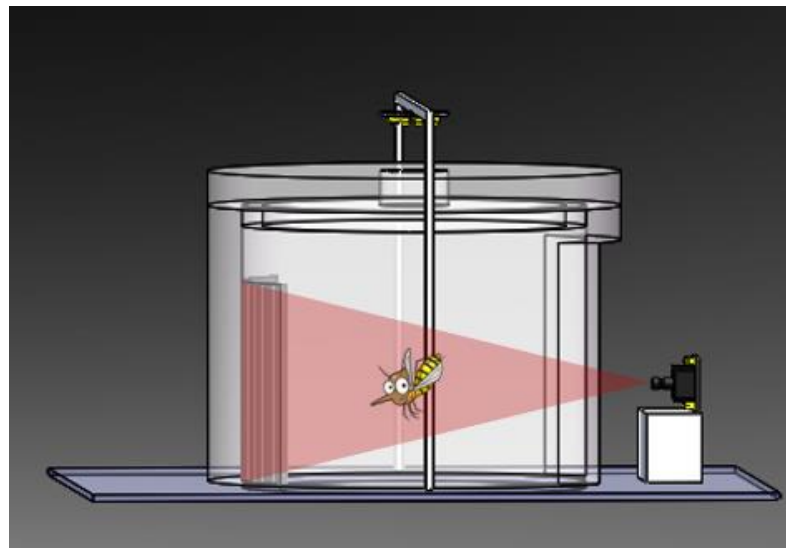


Figure 2. Upper part of the instrument with camera observing insects, which are illuminated from above, against a black cloth background.

3. Insect imaging

Many advanced methods have been proposed to detect and classify insects. A solution was presented in [49], to detect *Aedes Aegypti* mosquito species using images taken from a camera with a 500x optical zoom and employing a support vector machine algorithm. Fixed threshold and sliding threshold methods were introduced in [50] to detect insects by using smart phones. By improving the existing technique based on a fixed threshold method, an accuracy of 95% was obtained in online identifying and counting of insects. A system for combating infectious diseases by using image classification techniques and collaboration with normal citizens was introduced in [51]. Citizens were asked to use their smart phones for image capturing and reporting mosquitoes, which they encountered. A system, which integrates image processing, feature selection, unsupervised clustering, and a support vector machine (SVM) learning algorithm for classification was introduced in [52]. This system can with high accuracy classify nine different disease-carrying species, which were captured from a real outdoor trap. A more advanced algorithm based on a Convolutional Neural Network (CNN) was also used to detect and classify insects. A vision-based counting and recognition system is built by using so called You Only Look Once (YOLO) and SVM algorithms [53]. By combining the detection function of YOLO and the classification function of SVM, the system can achieve a detection rate of 93% and a classification rate of 90%. However, some of these methods need plenty of calculations and data to train the algorithms, which make them both time-consuming and expensive. On the other hand, the introduced methods with simple algorithms have low accuracy and performance.

We here present a new simple and effective method with low cost and high accuracy. The main idea of our method is template matching [54]. Template matching involves defining a measure or a “cost” to find the “similarity” between the (known) reference patterns and the (unknown) test patterns by performing a matching operation. Since template matching was originally proposed, many improved algorithms such as Fast Template Matching [55] and Very Fast Template Matching [56] were introduced with higher speed and better performance. Using a single template, the detection capacity is clearly very limited. Multi-target recognition is the most common case in object detection. Multi-target

template matching algorithms were developed based on single template matching. Classification is also another common task in object detection. Without employing large data sets and performing excessive calculations, a simple way with high accuracy is introduced in the present paper.

3.1. Detection and classification

We in this section represent our method to detect and classify mosquitoes from other insects captured by the camera. We chose bees as an example of a specie, to be discriminated against. There is a sequence of steps in our method, including image graying, padding, template matching, covering and classification, as detailed below.

- **Step one:** Convert the image (pixels: 1280 * 960) into grayscale.
- **Step two:** Cut out the template (pixels: 200 * 144) from one image sample, as shown in Figure 3(a), and perform the padding operation to another image sample. Padding operation means to increase length and width of the original photo with the length and width of the template to make the new image (pixels: 1480 * 1104), as shown in Figure 3(b). Without applying a padding operation, targets, which are near the boundary would be missed by the algorithm.

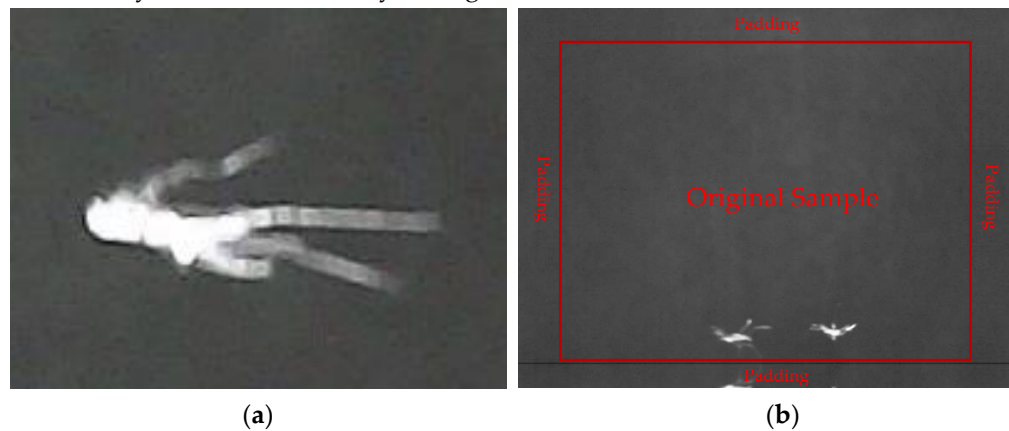


Figure 3. (a) Template image; (b) Image sample after padding.

First, align the template in the upper left corner of the new image. Calculate the similarity between the template and the area covered by the template (the Region of Interest, ROI). The correlation coefficient r_{ccoeff} is calculated as follows:

$$r_{ccoeff}(x, y) = \sum_{x', y'} I'_T(x', y') * I'_{ROI}(x + x', y + y') \quad (1)$$

Here, x and y are the pixel location information in the image; $0 \leq x < 1280$ and $0 \leq y < 960$. x' and y' are the pixel location information in template; $0 \leq x' < 200$ and $0 \leq y' < 144$. We further calculate I'_T :

$$I'_T(x', y') = \frac{I_T(x', y') - \frac{\sum_{x'', y''} I_T(x'', y'')}{W * H}}{\sqrt{\sum_{x'', y''} I_T^2(x'', y'')}} \quad (2)$$

$I_T(x', y')$ is the intensity of the pixel, which is located in (x', y') of the template. x'' and y'' are also the pixel location information in the template, $0 \leq x'' < 200$ and $0 \leq y'' < 144$. W and H are the width and height of the template, which are 200 and 144, respectively. Eqs (2) can be considered as a normalization process. By subtracting the mean and dividing by the variance, it is guaranteed that the particular light intensity will not affect the calculation results.

Further, I'_{ROI} is calculated as:

$$I'_{ROI}(x', y') = \frac{I_{ROI}(x', y') - \frac{\sum_{x'', y''} I_{ROI}(x'', y'')}{W * H}}{\sqrt{\sum_{x'', y''} I_{ROI}^2(x'', y'')}} \quad (3) \quad 258$$

Here $I_{ROI}(x', y')$ is the intensity of the pixel, which locates in (x', y') of the ROI region. x'' and y'' are also the pixel location information in the ROI; $0 \leq x'' < 200$ and $0 \leq y'' < 144$. Again, W and H are the width and height of the template, which are 200 and 144, respectively.

- **Step three:** Move the template one pixel to the right and repeat the calculation in Step 2 until the template arrives to the far right.
- **Step four:** When the template arrives the far right, move it one pixel down and repeat the calculation in Step two and Step three from the far left.
- **Step five:** After Step three and Step four, we can get a new matrix R_{ccoeff} of dimension $(1480 - 200+1) * (1104 - 144+1)$, composed of the calculated correlation coefficient r_{ccoeff} values. They are limited between -1 and 1, and the higher the result is, the greater the matching degree is (see Figure 4). Then we select the maximum value, the minimum value and maximum position information from the matrix. A threshold value of 0.4 is chosen. When the calculated correlation coefficient is higher than the threshold value, we define that it belongs to the location area of the object.

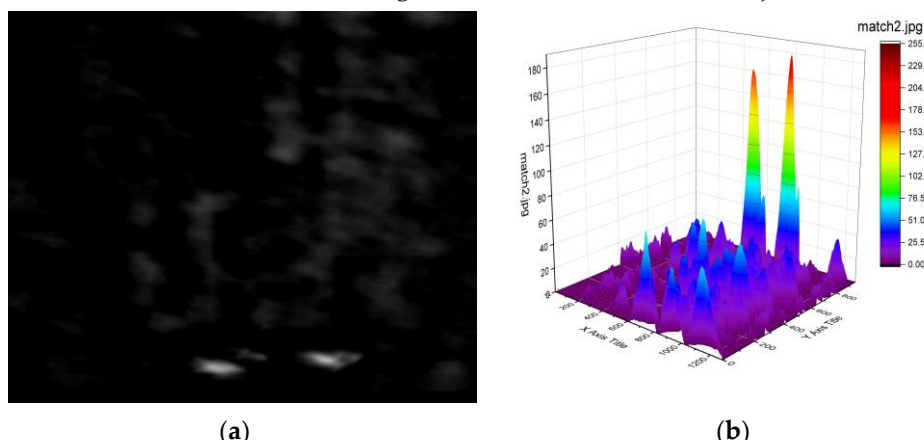


Figure 4. (a) New array R_{ccoeff} ; (b) 3D display of R_{ccoeff} .

- **Step six:** Centering on the coordinates of the maximum, an area of the same size (pixels: $200 * 144$) as the template in the original image (pixels: $1280 * 960$) is placed. Normalization, binarization and morphological processing are carried out for the region within the original area to obtain the contour of the object. Then we calculate the area and perimeter of this contour and divide the perimeter by the area to get the ratio.
- **Step seven:** In the matrix R_{ccoeff} , covering procedure is performed, which is replacing the area in Step six with the minimum value from Step five. Then repeat the process in Step five and Step six until the maximum value is smaller than the threshold.

3.2. Result evaluation

3.2.1. Detection algorithm evaluation

Single template matching is the main ideas of our proposed method. On the basis of signal template matching, a Multi-target template matching algorithm was developed by adding a covering procedure. In order to further improve the detection efficiency, a padding operation was introduced to Multi-target template matching, which constitutes the detection algorithm we proposed. To evaluate the performance of these three types of detection algorithms and the degree of possible improvement, we recorded 122 insect images (71 images of mosquitoes and 51 images of bees) and examples of results from the

three different algorithms are shown in Figures 5 and 6. Figure 5 shows the different results between single template matching and multi-target template matching. After adding the covering procedure, more than one target can be detected. The target (mosquito) near the boundary cannot be found by our algorithm in Figure 6(a). By padding the boundary, there are more pixels near the target that can be used when calculating (see Figure 6(b)). Table 1 shows the different detection rates for these three algorithms, which includes Single template matching, Multi-target template matching and our proposed detection algorithm. After our improvements, the detection rate reaches 92% from initially 64%.



Figure 5. (a) Single template matching; (b) Multi-target template matching.



Figure 6. (a) Without padding; (b) With padding.

Table 1. Performance of different algorithms.

| Algorithm type | Template matching | Covering | Padding | Detection rate |
|--|-------------------|----------|---------|----------------|
| Single template matching algorithm | ✓ | ✗ | ✗ | 64% |
| Multi-target template matching algorithm | ✓ | ✓ | ✗ | 84% |
| Our proposed algorithm | ✓ | ✓ | ✓ | 92% |

3.2.2. Classification method evaluation

To evaluate the performance of the classification methods, several pictures of bees were also recorded by the camera. After Step five in Section 2.1, a set of processes were performed with the ROI to classify mosquitoes and bees. The processes are displayed in Figures 7 and 8. We can see from Figures 7(d) and 8(d), that the body area of a bee is much larger than that of a mosquito. At the end of the processing step, only those targets classified as mosquitoes by the algorithm will be colored, otherwise there will be no operation. Different results are shown as Figures 7(e) and 8(e). For crude classification we calculate the area and perimeter of the target in the ROI. Perimeter means the number of pixels contained in the edge of the contour, while area means the number of all the pixels contained in the contour. Using these parameters we calculate two contrast functions, Perimeter/Area and $(\text{Perimeter})^2/\text{Area}$. The two function values for each mosquito and each bee are plotted in Figures 9(a) and 9(b). We note that while the second function (plotted in (b)) is dimensionless [58], i.e., only depends on shape/structure, the first function (plotted in (a)) also depends on size. We note, that shape/structure (the main information from imaging) alone can discriminate between the insects, but when also incorporating size (a), the discrimination becomes better.

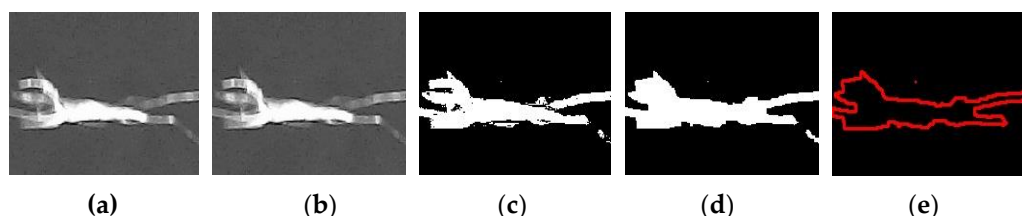


Figure 7. Processed sample of mosquito: (a) Original ROI; (b) Normalization; (c) Binarization; (d) Morphological processing; (e) Classification results.

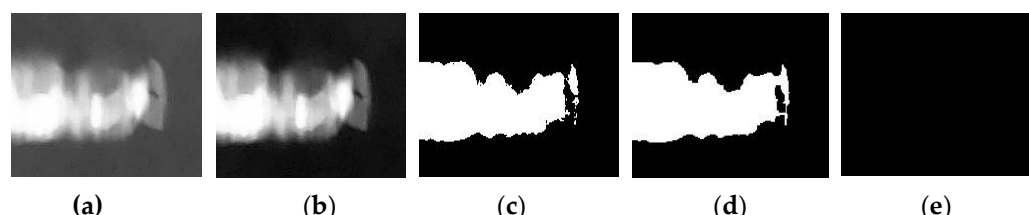


Figure 8. Processed sample of bee. (a) Original ROI; (b) Normalization; (c) Binarization; (d) Morphological processing; (e) Classification results.

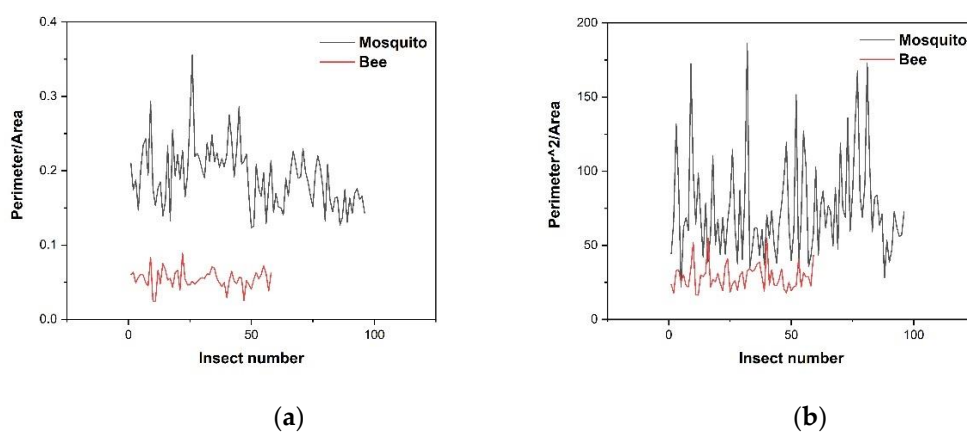


Figure 9. (a) The Perimeter/Area values for mosquitoes and bees. (b) The $(\text{Perimeter})^2/\text{Area}$ values for mosquitoes and bees.

Several evaluation criteria were introduced as shown in Eqs (4–6), TP, FN, FP are defined as follows. TP: True positive, which means that objects were detected as mosquitoes and they are mosquitoes. FN: False negative, which means that objects are not detected as mosquitoes but they are mosquitoes. FP: True negative, which means that objects were detected as mosquitoes but are not mosquitoes (which could be absence of insects, or a bee). Then Recall, Precision and F-measure values can be calculated as follows:

$$\text{Recall} = \frac{TP}{TP + FN} \quad (4) \quad 347$$

$$\text{Precision} = \frac{TP}{TP + FP} \quad (5) \quad 348$$

$$F - \text{measure} = 2 * \frac{\text{Precision} * \text{Recall}}{\text{Precision} + \text{Recall}} \quad (6) \quad 349$$

Sometimes there are contradictions between Recall and Precision. In this case, we need to carry out a synthesis. F-measure is defined as a harmonic mean of Recall and Precision [59], and the higher the F-measure, the better the effect will be. The performance results are presented in Table 2. No Classification means that we only used the detection method, while Classification means that we used the detection method and the Classification method at the same time. Compared with the No Classification method, all the values of the Classification method including Recall, Precision and F-measure, are increased. We note that there is a quite limited number samples in this evaluation. More advanced and accurate detection methods and processing methods require a large number of samples to support, which may be implemented in the near future.

Table 2. Performance of different methods.

| Methods | TP | FN | FP | Recall | Precision | F-measure |
|-------------------|----|----|----|--------|-----------|-----------|
| No Classification | 86 | 14 | 13 | 86.0% | 86.8% | 86.4% |
| Classification | 93 | 6 | 7 | 93.9% | 93.0% | 93.5% |

4. Conclusion and future work

In this paper, we have reviewed optical methods for insect characterization based on spectroscopic features such as reflectance, depolarization and the use of wing-beat frequency analysis. Such techniques can be implemented in remote sensing systems based on TOF or compact CW bi-static lidar systems, but also in in-situ insect traps employing, e.g., chemical attraction. CW systems, based on the Scheimpflug principle, are found to be particular powerful in the continuous logging and characterization of huge amounts of insects, which are intersecting the laser beam at different distances. Traps have been extensively used for later detailed manual analysis of species, but clearly are very labor intensive. We have here presented a method for image analysis of insects entering a trap, which operates with combined light, suction and chemical attraction. Images are recorded by a low-cost camera when illuminated insects are passing the field-of-view at a defined distance in the suction channel. In this way we ensure that the target size apparent size as captured by the camera does not change greatly, which facilitates the analysis of the images stored in the computer. Template matching and simple shape features (perimeter and area) were used for the classification. After data processing, an accuracy of 93% was obtained in automatic discrimination between mosquitoes and bees. Compared with spectroscopy techniques, such image capture and analysis can be implemented very cost-effectively using compact systems.

Clearly, there is much room for improvement in the approach taken. Sharper images can be captured with a higher-quality camera, and matched to an extensive bank of template images. Machine learning or deep learning approaches could be implemented. In such a way, more detailed speciation would become feasible, which would be particularly valuable for differentiating different species of mosquitos, and even sexes. Needless to say, the processing then becomes correspondingly more demanding.

Very simple equipment could still be powerful, by combining straight-forward image analysis along the lines presented, by wing-beat frequency determination. Then a photodiode would be used for the dual purpose of triggering the camera exposure, and for capturing the fundamental wing-beat frequency and the contents of over-tones, as evaluated by Fourier transformation. The frequency spectrum is related to the orientation of the insect [44], which could be inferred also from imperfect images. Basically, a quite powerful but still very cost-effective system could be achieved, by combining the wing-beat frequency analysis described in our earlier insect trap work [57], with the simple imaging approach presented in this paper. We believe, that such low-cost systems could be distributed and connected to a central processing unit for achieving very valuable information related to disease vectors, pollinators as well as agricultural pests in an extended area.

Author Contributions: Conceptualization, GYZ and SS; methodology, YYL, GYZ and SS; software, YYL, YTS and GYZ; validation, YYL, YTS and SS; formal analysis, YYL; resources, SS; writing – original draft preparation, YTS, YYL and SS; writing—review and editing, SS; supervision, SS; project administration, SS; funding acquisition, SS. All authors have read and agreed to the published version of the manuscript.

Funding: Financial support was obtained from the Science and Technology Program of Guangzhou (2019050001), and the Guangdong Provincial Key Laboratory of Optical Information Materials and Technology (2017B030301007).

Acknowledgments: The authors gratefully acknowledge the support Prof. Guofu Zhou.

Conflicts of Interest: The authors declare no conflicts of interest.

References

1. Stork, N. How many species of insects and other terrestrial arthropods are there on earth? *Annu. Rev. Entomol.* **2018**, *63*, 31–45. 410
2. Yinon, M.B.O.; Rob, P.; Ron, M. The biomass distribution on earth. *Proc. Nati. Acad. Sci.* **2018**, *115*, 6506–6511. 411
3. Schowalter, T.D.; Noriega, J.A.; Tscharntke, T. Insect effects on ecosystem services - introduction. *Basic Appl. Ecol.* **2018**, *26*, pp. 1–7. 412
4. World health organization. World malaria report 2020, **2020**. 413
5. Rosenberg, R.; Lindsey, N.P.; Fischer, M.; Gregory, C.J.; Hinckley, A.F.; Mead, P.S.; Paz-Bailey, G.; Waterman, S.H.; Drexler, N.A.; Kersh, G.J.; Hooks, H.; Partidge, S.K.; Visser, S.N.; Beard, C.B.; Petersen, L.R. Vital signs: Trends in reported vector-borne disease cases — United States and territories, 2004–2016. *MMWR Morb. Mortal Wkly Rep.* **2018**, *67*, 496–501. 414
6. Svanberg, S. *Atomic and molecular spectroscopy – Basic aspects and practical applications*, 4th ed.; Springer, Heidelberg, Berlin, New York, United States of America, 2004; 5th ed. in preparation. 415
7. Tkachenko, N.V. *Optical spectroscopy – Methods and instrumentation*, Elsevier, **2006**. 416
8. Brydegaard, M.; Svanberg, S. Photonic monitoring of atmospheric and aquatic fauna. *Laser Photonics Rev.* **2018**, *12*, 1800135. 417
9. Zhu, S.M.; Malmqvist, E.; Li, W.S.; Jansson, S.; Li, Y.Y.; Duan, Z.; Svanberg, K.; Feng, H.Q.; Song, Z.W.; Zhao, G.Y.; Brydegaard, M.; Svanberg, S. Insect abundance over Chinese rice fields in relation to environmental parameters, studied with a polarization-sensitive CW near-IR lidar system. *Appl. Phys. B* **2017**, *123*, 211. 418
10. Berthier, S. *Structural color reference iridescences: The physical colors of insects.*; Springer International, Dordrecht, **2007**. 419
11. Runemark, A.; Wellenreuther, M.; Jayaweera, H. H. E.; Svanberg, S.; Brydegaard, M. Rare events in remote dark-field spectroscopy: An ecological case study of insects. *IEEE Sel. Top. Quant. Electr.* **2012**, *5*, 1573–1582. 420
12. Zhu, S.M.; Li, Y.Y.; Gao, L.N.; Li, T.Q.; Zhao, G.Y.; Svanberg, S.; Lu, C.H.; Hu, J.D.; Huang, J.R.; Feng, H.Q. Optical remote detection of flying Chinese agricultural pest insects using dark-field reflectance measurements. *Acta Sinica Entomologica* **2016**, *59*, 1376–1385. 421
13. Li, Y.Y.; Zhang, H.; Duan, Z.; Lian, M.; Zhao, G.Y.; Sun, X.H.; Hu, J.D.; Gao, L.N.; Feng, H.Q.; Svanberg, S. Optical characterization of agricultural pest insects: A methodological study in the spectral and time domains. *Appl. Phys. B* **2016**, *122*, 213. 422
14. Li, M.; Jansson, S.; Runemark, A.; Peterson, J.; Kirkeby, C.T.; Jönsson, A.M.; Brydegaard, M. Bark beetles as lidar targets and prospects of photonics surveillance. *J. Biophot.* **2020**, e202000420. 423

15. Brydegaard, M.; Guan, Z.; Wellenreuther, M.; Svanberg, S. Insect monitoring with fluorescence lidar techniques: Feasibility study. *Appl. Opt.* **2009**, *48*, 5668–5677. 435
436
16. Guan, Z.; Brydegaard, M.; Lundin, P.; Wellenreuther, M.; Runemark, A.; Svensson, E. I.; Svanberg, S. Insect monitoring with fluorescence lidar techniques: Field experiments. *Appl. Opt.* **2010**, *49*, 5133–5142. 437
438
17. Weitkamp, C. *LIDAR: Range-resolved optical remote sensing of the atmosphere*; Weitkamp, C., Ed.; Springer-Verlag, New York, **2005**. 439
18. Svanberg, S. Fluorescence spectroscopy and imaging of lidar targets. In *Laser Remote Sensing*; Fujii, T., Fukuchi, T., Eds.; CRC Press, Boca Raton 2005; pp 433–467. 440
441
19. Raimondi, V.; Cecchi, G.; Lognoli, D.; Palombi, L.; Grönlund, R.; Johansson, A.; Svanberg, S.; Barup, K.; Hällström, J. The fluorescence lidar technique for the remote sensing of photoautotrophic biodeteriogens on outdoor cultural heritage: A decade of in situ experiments. *Int. Biodeter. Biodegr.* **2010**, *63*, 823. 442
443
20. Mei, L.; Guan, Z.G.; Zhou, H.J.; Lv, J.; Zhu, Z.R.; Cheng, J.A.; Chen, F.J.; Löfstedt, C.; Svanberg, S.; Somesfalean, G. Agricultural pest monitoring using fluorescence lidar techniques. *Appl. Phys. B* **2012**, *106*, 733–740. 445
446
21. Brydegaard, M.; Lundin, P.; Guan, Z.; Runemark, A.; Åkesson, S.; Svanberg, S. Feasibility study: Fluorescence lidar for remote bird classification. *Appl. Opt.* **2010**, *49*, 4531–4544. 447
448
22. Potamitis, I.; Ganchev, T.; Kontodimas, D. On automatic bioacoustic detection of pests: The cases of *Rhynchophorus Ferrugineus* and *Sitophilus Oryzae*. *J. Econ. Entom.* **2009**, *102*, 1681–1690. 449
450
23. Potamitis, I.; Rigakis, I. Measuring the fundamental frequency and the harmonic properties of the wingbeat of a large number of mosquitoes in flight using 2D optoacoustic sensors. *Appl. Acoust.* **2016**, *109*, 54–60. 451
452
24. Repasky, K.S.; Shaw, J.A.; Scheppelle, R.; Melton, C.; Carlsten, J.L.; Spangler, L.H. Optical detection of honeybees by use of wing-beat modulation of scattered laser light for locating explosives and land mines. *Appl. Opt.* **2006**, *45*, 1839–1843. 453
454
25. Hoffman, D.S.; Nehrir, A.R.; Repasky, K.S.; Shaw, J.A.; Carlsten, J.L. Range-resolved optical detection of honeybees by use of wing-beat modulation of scattered light for locating land mines. *Appl. Opt.* **2007**, *46*, 3007. 455
456
26. Brydegaard, M.; Gebru, A.; Svanberg, S. Super resolution laser radar with blinking atmospheric particles – application to interacting flying insects. *Prog. Electromagn. Res.* **2014**, *147*, 141. 457
458
27. Malmqvist, E.; Jansson, S.; Török, S.; Brydegaard, M. Effective parameterization of laser radar observations of atmospheric fauna. *IEEE J. Sel. Top. Quantum Electron.* **2015**, *22*, 327. 459
460
28. Mei, L.; Brydegaard, M. Continuous-wave differential absorption lidar. *Lasers Phot. Rev.* **2015**, *9*, 629. 461
29. Brydegaard, M.; Jansson, S. Advances in entomological laser radar. *The Journal of Engineering* **2019**, *2019*, 7542–7545. 462
30. Gebru, A.K.; Rohwer, E.G.; Neethling, P.; Brydegaard, M.S. Investigation of atmospheric insect wing-beat frequencies and iridescence features using a multispectral kHz remote detection system. *J. Appl. Rem. Sens.* **2014**, *8*, 083503. 463
464
31. Malmqvist, E.; Jansson, S.; Zhu, S.M.; Li, W.S.; Svanberg, K.; Svanberg, S.; Rydell, J.; Song, Z.W.; Bood, J.; Brydegaard, M.; Åkesson, S. The bat-bird-bug battle: Daily flight activity of insects and their predators over a rice field revealed by high resolution Scheimpflug lidar. *Roy. Soc. Open Sci.* **2018**, *5*, 172303. 465
466
32. Song, Z.W.; Zhang, B.X.; Feng, H.Q.; Zhu, S.M.; Hu, L.N.; Brydegaard, M.; Li, Y.Y.; Jansson, S.; Malmqvist, E.; Svanberg, K.; Zhao, G.Y.; Bood, J.; Svanberg, S.; Li, D.S. Application of lidar remote sensing of insects in agricultural entomology on the Chinese scene. *J. Appl. Entomol.* **2020**, *144*, 161. 467
468
33. Li, Y.Y.; Wang, K.; Quintero-Torres, R.; Brick, R.; Sokolov, A.V.; Scully, M.O. Insect flight velocity measurement with a CW near-IR Scheimpflug lidar system. *Opt. Express* **2020**, *28*, 21891. 469
470
34. Brydegaard, M.; Jansson, S.; Malmqvist, E.; Mlacha, Y.P.; Gebru, A.; Okumu, F.; Killeen, G.F.; Kirkeby, C. Lidar reveals activity anomaly of malaria vectors during pan-African eclipse. *Sci. Adv.* **2020**, *6*, eaay5487. 471
472
35. Gebru, A.; Jansson, S.; Ignell, R.; Kirkeby, C.; Prangsma, J.C.; Brydegaard, M. Multiband modulation spectroscopy for the determination of sex and species of mosquitoes in flight. *J. Biophotonics* **2018**, *11*, e201800014. 473
474
36. Lu, J.C.; Li, Y.; Yuan, Y.; Zhu, S.M.; Duan, Z.; Zhao, G.Y.; Svanberg, S. Monitoring of flying insects using a dual-wavelength CW lidar system. 2019 Asia Communications and Photonics Conference, Optical Society, Chengdu, China; Optical Society of America: **2019**; p. M4A.4. 475
476
37. Kirkeby, C.; Rydhmer, K.; Cook, S.M.; Strand, A.; Torrance, M.T.; Swain, J.L.; Prangsma, J.; Johnen, A.; Jensen, M.; Brydegaard, M.; Græsbøll, K. Advances in automatic identification of flying insects using optical sensors and machine learning. *Sci. Reports* **2021**, *11*, 1555. 477
478
38. Zhao, G.Y.; Ljungholm, M.; Malmqvist, E.; Bianco, G.; Hansson, L.A.; Svanberg, S.; Brydegaard, M. Inelastic hyperspectral lidar for profiling aquatic ecosystems. *Laser Photonics Rev.* **2016**, *10*, 807–813. 479
480
39. Duan, Z.; Yuan, Y.; Lu, J.C.; Wang, J.L.; Li, Y.; Svanberg, S.; Zhao, G.Y. Under-water spatially, spectrally, and temporally resolved optical monitoring of aquatic fauna. *Opt. Express* **2020**, *28*, 2600–2610. 481
482
40. Wang, X.; Duan, Z.; Brydegaard, M.; Svanberg, S.; Zhao, G.Y. Drone-based area scanning of vegetation fluorescence height profiles using a miniaturized hyperspectral lidar system. *Appl. Phys. B* **2018**, *124*, 207. 483
484
41. Potamitis, I.; Rigakis, I. Large aperture optoelectronic devices to record and time-stamp insects' wingbeats. *IEEE Sens. J.* **2016**, *16*, 6053. 485
486
42. Genoud, A.P.; Basistyy, R.; Williams, G.M.; Thomas, B.P. Optical remote sensing for monitoring flying mosquitoes, gender identification and discussion on species identification. *Appl. Phys. B* **2018**, *124*, 46. 487
488
43. Rigakis, I.; Potamitis, I.; Tatlas, N.-A.; Livadaras, I.; Ntalampiras, S. A multispectral backscattered light recorder of insects' wingbeats. *Electronics* **2019**, *8*, 277. 489
490

44. Brydegaard, M. Towards quantitative optical cross sections in entomological laser radar – potential of temporal and spherical parameterizations for identifying atmospheric fauna. *PLoS ONE* **2015**, *10*, e0135231. 495
496
45. Kenea, O.; Balkew, M.; Tekie, H.; Gebre-Michael, T.; Deressa, W.; Loha, E.; Lindtjorn, B.; Overgaard, H. Comparison of two adult mosquito sampling methods with human landing catches in south-central Ethiopia. *Malaria J.* **2017**, *16*, 30. 497
498
46. Degefa, T.; Yewhalaw, D.; Zhou, G.; Atieli, H.; Githeko, A.K.; Yan, G. Evaluation of human-baited double net trap and human-odour-baited CDC light trap for outdoor host-seeking malaria vector surveillance in Kenya and Ethiopia. *Malar. J.* **2020**, *19*, 174. 499
500
47. Moore, C.G.; McLean, R.G.; Mitchell, C.J.; Nasci, R.S.; Tsai, T.F.; Calisher, C.H.; Marfin, A.A.; Moore, P.S.; Gubler, D.J. Guidelines for arbovirus surveillance programs in the United States.; **1993**. 501
502
48. Maciel-de-Freitas, R.; Eiras, A.E.; Lourenço-de-Oliveira, R. Field evaluation of effectiveness of the BG-Sentinel, a new trap for capturing adult Aedes Aegypti (Diptera: Culicidae). *Mem. Inst. Oswaldo Cruz* **2006**, *101*, 321-5. 503
504
49. De Los Reyes, A.M.M.; Reyes, A.C.A.; Torres, J.L.; Padilla, D.A.; Villaverde, J. Detection of Aedes Aegypti mosquito by digital image processing techniques and support vector machine. 2016 IEEE Region 10 Conference (TENCON), Singapore, **2016**; 2342-2345. 505
506
50. Zhu, C.; Wang, J.; Liu, H.; Mi, H. Insect identification and counting in stored grain: Image processing approach and application embedded in smartphones. *Mob. Inf. Syst.* **2018**, *2018*, 5491706. 507
508
51. Munoz, J.P.; Boger, R.; Dexter, S.; Low, R.; Li, J. Image recognition of disease-carrying insects: A system for combating infectious diseases using image classification techniques and citizen science. Hawaii International Conference on System Sciences (HICSS), Hilton Waikoloa Village, Hawaii, Jan. 3rd **2018**. 509
510
52. Minakshi, M.; Bharti, P.; Chellappan, S. Leveraging smart-phone cameras and image processing techniques to classify mosquito species. In Proceedings of the 15th EAI International Conference on Mobile and Ubiquitous Systems: Computing, Networking and Services, Association for Computing Machinery, New York, NY, USA, **2018**, 77-86. 511
512
53. Zhong, Y.; Gao, J.; Lei, Q.; Zhou, Y. A vision-based counting and recognition system for flying insects in intelligent agriculture. *Sensors* **2018**, *18*, 1489. 513
514
54. Koutroumbas, K.; Theodoridis, S. Template matching. In *Pattern recognition*, 4th ed.; Koutroumbas, K., Theodoridis, S., Eds.; Academic Press: USA, **2009**; pp. 481-519. 515
516
55. Lewis, J.P. Fast template matching. *Vis. Interface* **1994**, *95*, 120-123. 517
518
56. Schweitzer, H.; Bell, J.W.; Wu, F. Very fast template matching. Heyden, A., Sparr, G., Nielsen, M., Johansen, P., Eds.; Computer Vision — European Conference on Computer Vision (ECCV), **2002**, 2353, 358-372. 519
520
57. Wang, J.L.; Zhu, S.M.; Lin, Y.Y.; Svanberg, S.; Zhao, G.Y. Mosquito counting system based on optical sensing. *Appl. Phys. B* **2020**, *126*, 28. 521
522
58. Svanberg, S.; Laser spectroscopy in medical diagnostics. In *Lasers for medical applications*; Jelinkova, H., Ed.; Woodhead Publ., **2013**, 307. 523
524
59. Sasaki, Y.; The truth of the F-measure. Teach Tutor Mater **2007**. 525
526
- 527
528
529